Deployable Vortex Generators based on Shape Memory Alloy Actuation

Aerodynamic design and performance analysis

Jorge Miret Marco

Deployable Vortex Generators based on Shape Memory Alloy Actuation

Aerodynamic design and performance analysis

by

Jorge Miret Marco

to obtain the degree of Master of Science
at the Delft University of Technology,
to be defended publicly on Thursday June 13th, 2024 at 09:30 AM.

Student number:	5628598
Supervisors:	Dr. M. Li Dr. W. J. Baars
Project duration:	September 2023 – June 2024
Institution:	Delft University of Technology
Faculty:	Faculty of Aerospace Engineering, Delft

Acknowledgements

This Master's thesis marks the end of my studies and reflects the culmination of my work over the past ten months. It has been a period filled with intense learning, both academically and personally. This journey has been a blend of rigorous research, countless hours of study, and practical application of the knowledge I have acquired throughout this program. Completing this thesis has been a significant milestone in my academic career, representing not only the effort and commitment of the past months but also the culmination of years of study and dedication. Nevertheless, I know that I could never have reached this point without the support and help of many individuals. Therefore, I would like to devote this page to acknowledging those who assisted me during my thesis and those who have always been there for me.

First and foremost, I would like to express my deepest gratitude to my supervisors, Dr. Morgan Li and Dr. Woutijn J. Baars. Your invaluable help during the experimental campaign of this research was a guiding light. Your unwavering support and insightful guidance have been crucial to the completion of this thesis. I also want to extend my heartfelt thanks to the other professors who generously shared their wisdom and offered their assistance whenever I needed it. Your expertise and willingness to help have been deeply appreciated.

To my friends in Delft, the Foulkeslaan family, you have been my main pillar of strength throughout this journey. Your constant support, laughter, and encouragement made this challenging path a joyous one. You turned every hurdle into a stepping stone and made me a very happy man. You have made me a better engineer, but above all, a better person. I admire you and I look forward to the bright future that awaits all of you.

To my childhood friends, thank you for making me the person that I am today. Thank you for making every trip back home feel like a warm embrace. Your love and companionship never wavered, and every reunion feels as if no time has passed. You make every homecoming special and fill it with love.

Finalment, als meus pares i la resta de la meua família, sou la meua base i la meua inspiració. Sou la raó per la qual estic ací hui. Vull que sapigueu que mai he donat per fet els vostres sacrificis. Cada dia d'aquesta aventura, he donat el 200%, impulsat pel desig de fer-vos sentir orgullosos. La vostra convicció inquebrantable en mi ha estat la meua major força, i espere que aquest assoliment reflectisca la profunditat de la meua gratitud i amor.

To you all, thank you. Dankjewel. Gracias. Gràcies.

Jorge Miret Marco
Delft, June 2024

Abstract

Flow control is a critical challenge in enhancing the performance of aerodynamic devices across various sectors, including aeronautics, automotive, and energy production. The primary objective of this research is to delay flow separation by enhancing mixing within the boundary layer and restoring momentum near the wall, thus minimizing or preventing separation within an Adverse Pressure Gradient (APG). In order to achieve this goal, this research focuses on the use of deployable vortex generators (VGs) actuated by shape memory alloys, combining the benefits of both passive and active VGs to improve aerodynamic efficiency.

A comprehensive review of existing literature highlighted a significant gap in understanding the aerodynamic and structural dynamics of shape-adaptive vortex generators. To address this, the project investigates the optimal aerodynamic configurations for VGs that can retract and extend, aiming to overcome the limitations of traditional static designs.

The conclusions drawn from the Computational Fluid Dynamics (CFD) analysis and experimental studies provide critical insights into VG performance. The skew angle sensitivity analysis revealed the robustness of various VG designs against axial loads, notably with the vane design showing reduced sensitivity to inflow angles. However, challenges related to normal and side loads, especially for configurations like the hollow ramp, underscore the need for durable actuation mechanisms.

Experimental tests of uncontrolled flow dynamics along a curved backward-facing ramp indicated a three-dimensional flow regime with intermittent separation bubbles, influenced by the ramp's geometry. Controlled flow studies identified counter-rotating vanes as the most effective VG configuration, producing consistent flow control results despite side load challenges. Co-rotating vanes and backward ramp designs exhibited varied effectiveness, necessitating further optimization.

In response to these findings, a novel design approach is proposed, leveraging rigid vane actuators constructed from durable materials and strategically utilizing shape memory alloys for precise skew angle adjustments. This proposed solution offers a pragmatic alternative to traditional VG configurations, mitigating side load issues while maintaining adaptability and control over flow dynamics.

In summary, this research advances the understanding of shape-adaptive vortex generators in flow control applications. The findings emphasize the potential of counter-rotating vane arrays while highlighting the need for robust actuation mechanisms and further design optimizations to address the identified challenges.

Contents

List of Figures

List of Tables

Nomenclature

Abbreviations

Abbreviation	Definition
2D2C	2-Dimensional, 2-Component
2D3C	2-Dimensional, 3-Component
3D3C	3-Dimensional, 3-Component
AFC	Active Flow Control
APG	Adverse Pressure Gradient
BL	Boundary Layer
CD	Common Downwash
CFD	Computational Fluid Dynamics
CoR	Co-Rotating
CR	Complete Reattachment
CtR	Counter-Rotating
CU	Common Upwash
D	Detachment
DNS	Direct Numerical Simulation
ER	Expansion Ratio
FRP	Fiber-Reinforced Composites
GISB	Geometry-Induced Separation Bubble
HWA	Hot Wire Anemometry
IBL	Integral Boundary Layer
ID	Incipient Detachment
ITD	Intermittent Transitory Detachment
ITR	Intermittent Transitory Reattachment
KPI(s)	Key Performance Indicator(s)
PFC	Passive Flow Control
PISB	Pressure-Induced Separation Bubble
PIV	Particle Image Velocimetry
PUVG	Pop-Up Vortex Generators
RANS	Reynolds-Averaged Navier Stokes
SA	Spalart-Allmaras
SARC	Spalart-Allmaras with Rotation/Curvature Correction
SBVG(s)	Sub Boundary layer Vortex Generator(s)
SPIV	Stereoscopic Particle Image Velocimetry
SST	Shear Stress Transport
SSTRC	Shear Stress Transport with Rotation/Curvature Correction

Abbreviation	Definition
TBL	Turbulent Boundary Layer
TD	Transitory Detachment
TKE	Turbulent Kinetic Energy
TR	Transitory Reattachment
TSB	Turbulent Separation Bubble
VG(s)	Vortex Generator(s)
VLSM	Very Large-Scale Motions
ZPG	Zero Pressure Gradient

Symbols

Symbol	Definition	Unit
A	Axial force	[kg m s^{-2}]
A_R	Reference area	[m^2]
C	Crosswind force	[kg m s^{-2}]
C_A	Axial force coefficient	[–]
C_D	Drag coefficient	[–]
$C_\mathcal{D}$	Dissipation coefficient	[–]
C_f	Skin friction coefficient	[–]
C_L	Lift coefficient	[–]
C_N	Normal force coefficient	[–]
C_S	Side force coefficient	[–]
d_p	Particle diameter	[m]
d_τ	Particle image diameter	[px]
D	Drag force	[kg m s^{-2}]
D	Lens aperture	[m]
f	Lens focal length	[m]
$f_\#$	F-stop	[–]
H	Shape factor	[–]
H^*	Kinetic energy shape factor	[–]
H^{**}	Density flux shape factor	[–]
I	Electric current	[A]
k	Turbulent kinetic energy	[m^2 s^{-2}]
l	Pitch of the helical vortex lines	[m]
L	Lift force	[kg m s^{-2}]
M	Magnification factor	[–]
M_e	Boundary layer’s edge Mach number	[–]
N	Normal force	[kg m s^{-2}]
p	Pressure	[kg m^{-1} s^{-2}]
r	Radial coordinate	[m]
Re	Reynolds number	[–]
Re_θ	Momentum thickness Reynolds number	[–]
Re_τ	Friction Reynolds number	[–]
S	Side force	[kg m s^{-2}]
T	Temperature	[K]
u	Instantaneous velocity: x component	[m s^{-1}]
u'	Velocity fluctuation: x component	[m s^{-1}]
u^+	Non-dimensional velocity	[–]
$\overline{u}$	Mean velocity: x component	[m s^{-1}]
u_e	Boundary layer’s edge velocity	[m s^{-1}]
u_τ	Wall-friction velocity	[m s^{-1}]
U_∞	Freestream velocity	[m s^{-1}]
v	Instantaneous velocity: y component	[m s^{-1}]
v'	Velocity fluctuation: y component	[m s^{-1}]
$\overline{v}$	Mean velocity: y component	[m s^{-1}]

Symbol	Definition	Unit
v^*	Wall-friction velocity	[m s^{-1}]
w	Instantaneous velocity: z component	[m s^{-1}]
w'	Velocity fluctuation: z component	[m s^{-1}]
$\overline{w}$	Mean velocity: z component	[m s^{-1}]
x, y, z	Longitudinal, vertical and transverse coordinates	[m]
x^*	Non-dimensional streamwise distance	[–]
y^+	Non-dimensional wall distance	[–]
β	Clauser pressure-gradient parameter	[–]
β	Vortex generator vane skew angle	[deg]
γ_{pu}	Forward flow coefficient	[–]
Γ	Circulation of a vector field around a closed curve	[m^2 s^{-1}]
Γ^*	Non-dimensional circulation of a vector field around a closed curve	[–]
δ	Boundary layer thickness	[m]
δ^*	Displacement thickness	[m]
δ_{99}	Boundary layer thickness where $u = 0.99U_\infty$	[m]
ε	Effective size of the vortex core	[m]
θ	Momentum thickness	[m]
κ	Von Karman constant	[–]
λ	Light wavelength	[m]
μ	Dynamic viscosity	[kg m^{-1} s^{-1}]
ν	Kinematic viscosity	[m^2 s^{-1}]
ξ	Pressure-gradient parameter	[–]
ρ	Density	[kg m^{-3}]
τ_w	Wall shear stress	[kg m^{-1} s^{-2}]
χ	Backflow coefficient	[–]
χ	Vortex strength coefficient	[–]
ω	Specific turbulence dissipation rate	[s^{-1}]

1

Introduction

1.1. Motivation

In the field of fluid dynamics, the phenomenon of flow separation is crucial, with profound implications for the aerodynamic performance of various systems. As a boundary layer decelerates under an adverse pressure gradient (APG), the risk of separation emerges, leading to potential performance detriments. Instances such as wing stall, limitations in diffusers, and the threat of structural fatigue highlight the critical importance of understanding and controlling flow separation in engineering applications.

Conventional methods to address flow separation primarily involve altering the flowfield through mechanisms like vortex generators or steady-blowing jets. While these approaches, in particular the use of vortex generators, have found practical use, their static design introduces limitations. For example, static vortex generators increase drag during the cruise phase of aircraft flight, reducing overall aerodynamic efficiency in aircraft. Additionally, the complexity of setting up and controlling mechanical systems restricts the implementation of adaptive solutions that could optimize performance across diverse flight conditions.

The motivation for this research project arises from the recognition of limitations within existing methodologies and the quest for more effective strategies to control flow separation. This project aims to transcend the constraints of conventional static designs by exploring deployable vortex generators based on active hybrid composites. The focus of this project revolves around developing an optimal aerodynamic design for vortex generator devices that dynamically respond to varying flight conditions without the need for elaborate mechanical systems. This approach not only seeks to delay or suppress flow separation but also aims to optimize aerodynamic performance throughout the entire flight envelope.

In the pursuit of this objective, inspiration is drawn from the potential offered by active hybrid structures, particularly those incorporating shape memory alloys (SMA) and fiber-reinforced composites (FRP) as active elements. This innovative approach allows for simplification of mechanical systems, reduction in weight, and scalability, providing a promising avenue for overcoming the limitations of traditional static vortex generators. In addition to enhanced aerodynamic efficiency, potential benefits also encompass improved safety and reduced noise during take-off and landing.

Thus, the preliminary research question for the project arises:

> Preliminary research question
>
> To what extent can the aerodynamic efficiency of vortex generators be enhanced by incorporating shape-adaptive materials, and what design features are critical for optimal performance?

In summary, this research aims to push the boundaries of flow separation control by exploring novel methods based on adaptive vortex generators and active hybrid composites. Through a comprehensive understanding of the limitations of current methodologies and the pursuit of innovative solutions, we aim to contribute to the advancement of aerodynamic technology, offering more efficient and adaptable means of managing flow separation in aeronautical applications.

1.2. Research methodology

This research explores the technical feasibility surrounding the aerodynamic characterization of vortex generators manufactured using shape-adaptive materials. The project aims to leverage advanced computational tools, specifically Computational Fluid Dynamics (CFD), as well as flow measurement techniques such as Particle Image Velocimetry (PIV), to solve the intricate interplay between aerodynamics and material dynamics in shape-adaptive vortex generators. The ultimate goal is to contribute valuable insights that could enhance the aerodynamic performance of aeronautical systems.

Therefore, this project aims to fill this knowledge gap by exploring the aerodynamic complexities of shape-adaptive vortex generators, particularly those utilizing shape memory alloys for retraction and extension. The goal is to identify and achieve the optimal aerodynamic configuration, pushing the boundaries of conventional flow control methods and paving the way for new innovations.

To address the gap in academic knowledge and simultaneously contribute to resolving this aviation industry challenge, the subsequent thesis work establishes the following research objective:

> Research Objective
>
> Investigate the aerodynamic features of deployable vortex generators employing shape memory alloy actuation, aiming to identify the optimal aerodynamic configuration and advance the understanding of flow separation control.

In order to guide the research process, make sure the necessary tasks are completed, and eventually verify that the goal of the research objective has been accomplished, the following research questions and subquestions have been established:

Q.1 How does an array of vortex generators influence the prevention of flow separation over a backward-facing ramp?

- **Q1.1** What quantitative metrics can be employed to assess the effectiveness of vortex generators?

Q1.2 How do variations in the shape and size of individual vortex generators influence the overall aerodynamic efficiency of the array?

Q1.3 How does the spacing between individual vortex generators impact their collective aerodynamic performance?

Q1.4 How does the spacing between the vortex generator array and the separation point impact their flow control capabilities?

Q.2 **What is the optimal aerodynamic configuration for a deployable vortex generator based on shape memory alloy actuation for enhancing performance?**

Q.2.1 What are the distinct effects of deployable vortex generators compared to static vortex generators in preventing flow separation?

1.3. Report outline

Beginning with the introduction, the present chapter sets the stage by outlining the context and significance of the study. The remainder of this report is structured into four interrelated parts to provide a comprehensive overview of the research conducted:

Part I Background

- Chapter 2 delves into the fundamentals of turbulent boundary layers and the phenomena of separation, covering aspects such as boundary layer scaling and turbulent separation bubbles, including flow detachment and reattachment.
- Chapter 3 explores separation control techniques with a focus on vortex generators, discussing passive and active methods along with vortex dynamics.
- Chapter 4 investigates various design concepts for vortex generators, including conventional, sub-boundary layer, and deployable configurations.
- Chapter 5 concludes with a summary of key findings.

Part II Methodology

- Chapter 6 details the computational fluid dynamics (CFD) methodology employed in the study, including the modeling approach, key performance indicators, computational setup, mesh independence study, and verification procedures.
- Chapter 7 describes the experimental methodology, covering the test section, separation ramp, actuators, and particle image velocimetry (PIV) techniques used for flow characterization.

Part III Results and Discussion

- Chapter 8 examines numerically the sensitivity of multiple VG designs to skew angle using CFD.
- Chapter 9 focuses on the experimental characterization of uncontrolled flow.
- Chapter 10 discusses the characterization of controlled flow through various streamwise and crossflow planes, comparing computational and experimental data.
- Chapter 11 proposes a design concept for deployable VGs based on the study's findings.

Part IV Conclusions and Recommendations

- Chapter 12 summarizes the key conclusions drawn from the study's findings.
- Chapter 13 provides recommendations for future research directions based on the insights gained from the investigation.

Part I

Background

2

Turbulent boundary layers and separation

This chapter delves into the phenomena of turbulent boundary layers and separation, foundational aspects critical to understanding advanced flow control techniques. Section 2.1 begins with an overview of boundary layer fundamentals, providing essential insights into the development and characteristics of boundary layers. Section 2.2 addresses turbulent boundary layer scaling, which is crucial for accurately predicting and modeling turbulent flows. Following this, in Section 2.3, the discussion moves to turbulent separation bubbles, examining their formation, dynamics, and impact on flow behavior. This includes a concise description of the flow detachment and reattachment processes. Together, these topics offer a comprehensive understanding of turbulent boundary layers and separation, setting the stage for subsequent chapters on flow control methodologies.

2.1. Boundary layer fundamentals

As an object moves through a fluid, or as a fluid moves past an object, the fluid molecules near the object are disturbed and move around it. In particular, the molecules in the immediate vicinity of a surface adhere to this surface, inducing a no-slip boundary condition (zero velocity at the wall). The molecules just above the surface are slowed down by collisions with the molecules sticking to the surface. These molecules, in turn, slow down the flow just above them. The farther one moves away from the surface, the fewer the collisions affected by the object surface. This creates a thin layer of fluid near the surface in which the velocity increases from zero at the surface until it reaches the the freestream value away from the surface. The thin layer, consisting of fluid whose velocity has not yet returned to the freestream velocity, is called the *velocity boundary layer*.

The Reynolds number (Re) expresses the ratio of inertial to viscous forces. Boundary layers are prevalent in flows characterized by relatively high Reynolds numbers and low fluid viscosities, which are common in many technical applications. While the $Re \to \infty$ limiting solution is often a useful approximation, it fails to satisfy the no-slip condition, requiring the consideration of viscosity effects that enforce null velocity directly at the wall. By dividing the flow field into the inviscid outer flow and the boundary layer, the theoretical treatment of high Reynolds number flows is simplified. This division is based on the fact that viscosity effects become increasingly confined to narrow regions near the solid wall as the Reynolds number increases, resulting in a thinner boundary layer.

The boundary layer thickness (δ) represents the distance normal to the wall to the point where the flow velocity has essentially reached the freestream velocity, U_∞ (sometimes denoted as u_e, where the subscript e denotes flow conditions at the edge of the boundary layer). Figure 2.1 presents a schematic representation of the velocity distribution across a thin flat plate (with an exaggerated width in the wall-normal direction). At the leading edge, the velocity is constant and parallel to the plate. As the distance from the leading edge increases, the layer of particles slowed down by friction grows larger, as more fluid particles are affected by the retardation. Consequently, the boundary layer thickness increases as a function of the development length, i.e. $\delta(x)$.

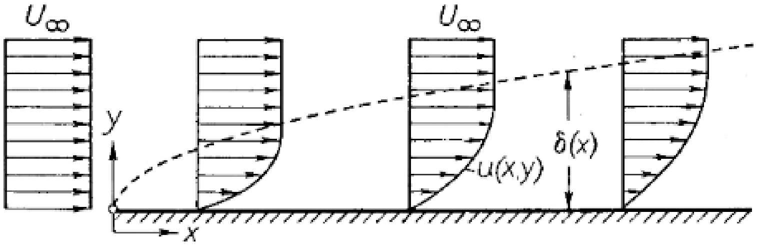

Figure 2.1: Boundary layer at a flat plate at zero incidence [From Schlichting and Gersten (2017)]

For lower Reynolds numbers, the boundary layer is laminar and the streamwise velocity changes uniformly as one moves away from the wall. For higher Reynolds numbers, the boundary layer is turbulent and the streamwise velocity is characterized by unsteady swirling flows inside the boundary layer. In the context of TBLs, alternative physical interpretations of the boundary layer thickness are often preferred, since the upper part of the velocity profile is so level that even minor alterations or inaccuracies in the profile can cause considerable discrepancies in the measured thickness. Despite this uncertainty, the parameter δ is still widely used due to its simple physical interpretation and ease of determination.

Other commonly employed measures are the integral properties of the velocity profile. As described by White (2006), an integral analysis of a control volume over a flat plate yields these properties. By applying mass conservation principles, the displacement thickness, denoted as δ^*, is formally defined (see Equation 2.1). Similarly, conservation of momentum in the x direction provides the definition of the momentum thickness, denoted as θ (see Equation 2.2).

$$\delta^* = \int_0^\infty \left(1 - \frac{u}{u_e}\right) dy \tag{2.1}$$

$$\theta = \int_0^\infty \frac{u}{u_e}\left(1 - \frac{u}{u_e}\right) dy \tag{2.2}$$

The displacement thickness δ^* represents the amount by which the non-viscous external flow is pushed outward due to the decrease in velocity in the boundary layer, whereas the momentum thickness θ represents the distance that would need to be traversed in an inviscid fluid for the total flow momentum to be equivalent to the momentum of the actual flow (Schlichting and Gersten 2017). Various Reynolds numbers can be defined based on the aforementioned magnitudes:

$$Re = \frac{U_\infty x}{\nu}, \quad Re_\delta = \frac{U_\infty \delta}{\nu}, \quad Re_{\delta^*} = \frac{U_\infty \delta^*}{\nu}, \quad Re_\theta = \frac{U_\infty \theta}{\nu} \tag{2.3}$$

The shape factor H is defined as the ratio of the displacement thickness to the momentum thickness. It serves as a non-dimensional measure of the velocity profile shape, and is particularly relevant as an indicator for stability against transition and separation. A high shape factor indicates an empty profile, approaching separation, while a low shape factor indicates a thin, full, high wall shear stress boundary layer. In line with the definitions of the integral boundary layer parameters, since the velocity u at any point within the boundary layer is always smaller than the velocity at the edge u_e, the value of the displacement thickness δ^* consistently exceeds the value of the momentum thickness θ. Consequently, the shape factor H invariably exceeds unity.

$$H = \frac{\delta^*}{\theta} > 1 \tag{2.4}$$

2.2. Turbulent boundary layer scaling

A turbulent boundary layer can be categorized into two distinct sections: the inner layer and the outer layer, complemented by an intermediate overlap region situated between the two.

The behavior of the inner layer is strongly influenced by conditions near the wall. According to Prandtl (1933), the velocity profile in this region depends on fluid properties (ρ and μ), the distance y from the wall, and the wall shear stress τ_w, which is the only direct influence from the freestream flow. Introducing the wall-friction velocity, defined as $u_\tau = \sqrt{\tau_w/\rho}$, and performing a dimensional analysis over this dependence leads to the formulation of the *law of the wall*:

$$\frac{\overline{u}}{u_\tau} = f\left(\frac{y u_\tau}{\nu}\right) \tag{2.5}$$

In contrast, the outer layer behavior is described by the Von Karman (1931) theory, which posits that the wall primarily acts as a source of resistance, reducing the local velocity $\overline{u}(y)$ below the freestream velocity U_∞ without being directly influenced by viscosity μ. However, it is affected by wall shear stress, boundary layer thickness, and the pressure gradient of the flow. A dimensional analysis over these dependencies leads to the formulation of the *defect law*:

$$\frac{u_e - \overline{u}}{u_\tau} = g\left(\frac{y}{\delta}, \xi\right) \tag{2.6}$$

where the pressure gradient parameter ξ is defined as $\xi = \dfrac{\delta}{\tau_w}\dfrac{dp_e}{dx}$.

Clauser in 1954 and 1956 demonstrated, through experimental trial and error, that for boundary layer flows characterized by pressure gradients, the self-similarity of the defect profile can be achieved by maintaining a constant value of the Clauser pressure-gradient parameter β, based on the displacement thickness. This parameter, distinct from the Falkner-Skan parameter, is defined as $\beta = \dfrac{\delta^*}{\tau_w}\dfrac{dp_e}{dx}$.

Assuming the existence of a zone within the boundary layer where both the inner and outer laws hold true simultaneously, the *overlap law* can be established:

$$\frac{\overline{u}}{u_\tau} = f\left(\frac{y}{\delta}\frac{\delta u_\tau}{\nu}\right) = \frac{u_e}{u_\tau} - g\left(\frac{y}{\delta}, \xi\right) \tag{2.7}$$

where f and g must be logarithmic functions, according to functional analysis. Consequently, in the overlap layer:

- in inner variables:

$$\frac{\overline{u}}{u_\tau} = \frac{1}{\kappa}\ln\left(\frac{y u_\tau}{\nu}\right) + B \tag{2.8}$$

- in outer variables:

$$\frac{u_e - \overline{u}}{u_\tau} = -\ln\left(\frac{y}{\delta}\right) + A(\xi) \tag{2.9}$$

where κ and B are near-universal constants for smooth walls ($\kappa \approx 0.41$ and $B \approx 5.0$) and A varies with the pressure gradient ξ.

An additional examination of the inner law reveals that three more subregions can be identified, as depicted in Figure 2.2:

- Linear (or viscous) sublayer. Very close to the wall, i.e. $y^+ \leq 5$, turbulence is suppressed and the boundary layer is governed by viscous shear, resulting in a linear velocity profile.
- Buffer layer. Between the linear sublayer and the logarithmic (overlap) layer, i.e. $5 \leq y^+ \leq 30$, the velocity profile is neither linear nor logarithmic, but rather a gradual transition between the two.
- Logarithmic (overlap) layer. In the sublayer furthest from the wall, i.e. $y^+ \geq 30$, the inner law gradually blends into the overlap layer.

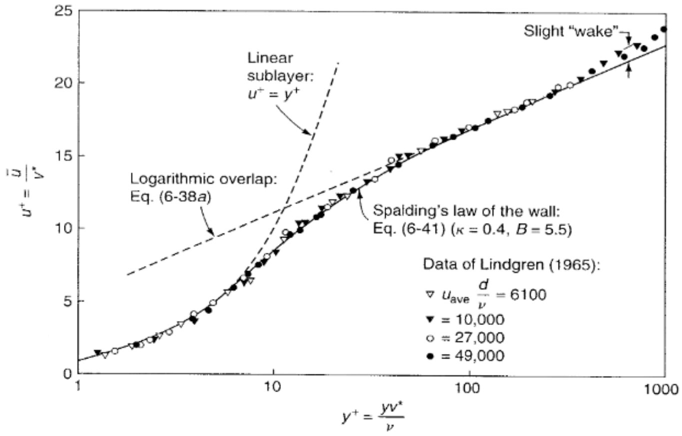

Figure 2.2: Inner law expression for a ZPG TBL expressed in inner variables [From White (2006)]

Shifting the focus to the outer law, an additional examination reveals its sensitivity to the pressure gradient parameter ξ. Coles (1956) addressed this challenge by noting that, when viewed from the freestream perspective, the surplus velocity within the outer layer relative to the log layer exhibited a nearly uniform wake-like pattern. This insight permitted the transformation of the entire velocity profile into the following expression:

$$u^+ = \frac{\overline{u}}{u_\tau} = f(y^+) + \frac{2\Pi}{\kappa} \cdot w\left(\frac{y}{\delta}\right) \tag{2.10}$$

where $f(y^+)$ represents the inner law (including the overlap region), and $\frac{2\Pi}{\kappa} \cdot w(\frac{y}{\delta})$ represents the wake component. Here, Π denotes the Coles' wake parameter, representing the wake strength, and w the wake function encoding the deviation from the law of the wall, i.e. null at $y = 0$, and unit at $y = \delta$.

2.3. Turbulent separation bubbles

A Turbulent Separation Bubble (TSB) is a complex flow feature commonly encountered within TBLs over curved surfaces or abrupt geometric changes. It represents a distinctive region where the flow partially or fully separates from the surface, creating a re-circulation zone characterized by the coexistence of turbulent and separated flow structures. Understanding the intricate mechanisms governing TSB formation, evolution, and dissipation is crucial for optimizing the performance of diverse engineering devices, including airfoils, diffusers, and heat exchangers, and is of paramount importance in addressing flow control challenges in fluid mechanics research. In this section, the detailed aspects of TSBs are introduced, focusing on flow detachment and flow reattachment to describe the underlying physics and implications of these phenomena within TBLs.

2.3.1. Flow detachment

Separation in boundary layer flows encompasses the departure, breakaway, or breakdown of the flow from a surface, as defined by Simpson (1989). At moderate Reynolds numbers, separation bubbles occur when the shear layer detaches from the surface and then reattaches downstream, likely due to turbulence entrainment (Dovgal et al. 1994; Tani 1964). For steady-freestream two-dimensional flows on low curvature or flat surfaces, separation initiates intermittently, with flow reversal occurring only part of the time at certain points. Simpson (1981) proposed quantitative definitions of detachment states near the wall, based on the fraction of time with reverse flow, characterized by the backflow coefficient χ. These include Incipient Detachment (ID), Intermittent Transitory Detachment (ITD), Transitory Detachment (TD), and Detachment (D), corresponding to χ values of 0.01, 0.20, 0.50, and $\overline{\tau}_w = 0$, respectively.

Data suggest that when instantaneous backflow exists 50% of the time ($\chi = 0.50$), the time-averaged wall shear stress $\overline{\tau}_w$ tends to null, marking both the Transitory Detachment (TD) and Detachment (D) points. Furthermore, the lengths of regions between these points can vary with geometry and flow conditions but their definitions remain consistent. Analogously, points of Transitory Reattachment (TR) occur when $\chi = 0.50$ in the reattachment region, Intermittent Transitory Reattachment (ITR) when $\chi = 0.20$, and Complete Reattachment (CR) when $\chi = 0.01$.

Two primary mechanisms leading to flow separation are pressure-induced separation and geometry-induced separation. The former, termed pressure-induced separation bubbles (PISB), occurs in the presence of large APGs around streamlined bodies. On the other hand, geometry-induced separation bubbles (GISB) are generated due to geometric features, such as the streamwise curvature of a surface, or the presence of singularities, such as a sharp corner/blunt leading edge/rounded leading edge.

In this study of a backward-facing ramp, the presence of a mild streamline curvature prompts consideration of both geometry-induced and pressure-induced separation. Given the modest curvature, it is likely that the predominant factor driving separation is the associated pressure gradient. This underscores the intricate interplay between geometric features and pressure gradients in cases where a clear distinction between geometry-induced and pressure-induced separation is less evident.

Geometry-induced separation

When it comes to separation caused by geometry, two scenarios can be identified: boundary layer separation caused by the curvature of a surface, and boundary layer separation caused by a geometric singularity, such as a sharp point (e.g. a backward-facing step, fence, or blunt face).

In the absence of streamwise pressure gradients, convex surface curvature induces a positive pressure gradient normal to the wall, reducing downstream entrainment, while concave curvature results in a negative pressure gradient, enhancing entrainment, mixing, and turbulent shearing (Simpson 1989). However, in situations involving both convex curvature and APGs, such as airfoil flows, the influence of curvature on entrainment diminishes compared to zero-pressure gradient cases. Nonetheless, the interaction between surface curvature, APGs, and TBL detachment remains context-dependent, particularly for low-curvature surfaces. Studies indicate minimal curvature effects for low-curvature surfaces (Schubauer and Klebanoff 1951; Deutsch and Zierke 1986), while convex curvature $\delta/R \geq 0.1$ has been proven to lead to detachment farther upstream than on flat plates (Baskaran et al. 1987; Sandborn and Liu 1968; Chou and Sandborn 1973). This phenomenon arises because rapid changes in surface curvature near convex surfaces induce a sudden shift in flow direction and magnitude due to local increases in flow cross-sectional area and surface pressure.

In the context of a geometric singularity, such as a backward-facing step, quick, abrupt changes in the curvature of the surface may appear, and these can yield a very unsteady and complex flow field, as depicted in Figure 2.3a. As the boundary layer departs the surface, the location of the maximum shear point no longer resides at the wall, and the separated shear layer resembles a standard plane-mixing layer. However, it differs in the fact that the low-speed side of the shear layer is highly turbulent. Additionally, a portion of the shear layer fluid is deflected upstream into the recirculating flow, giving rise to a region beneath the shear layer that exhibits substantial backflow velocity.

Pressure-Induced separation

Pure pressure-gradient-induced turbulent boundary layer separation occurs due to an APG on a smooth surface instead of a geometric singularity. Near the wall, flow slows down under an APG until backward flow emerges at the onset of detachment. Small three-dimensional flow components briefly move against the primary flow direction before being carried downstream. These reverse flows occur in regions with reduced kinetic energy and stem from forces generated by large-scale structures and the APG (Simpson 1996). These structures provide turbulent energy to the detaching flow, allowing the separation front to fluctuate in space and time. Even on smooth curved surfaces when surface geometry primarily influences separation, separation points can fluctuate, adding complexity to the separation process.

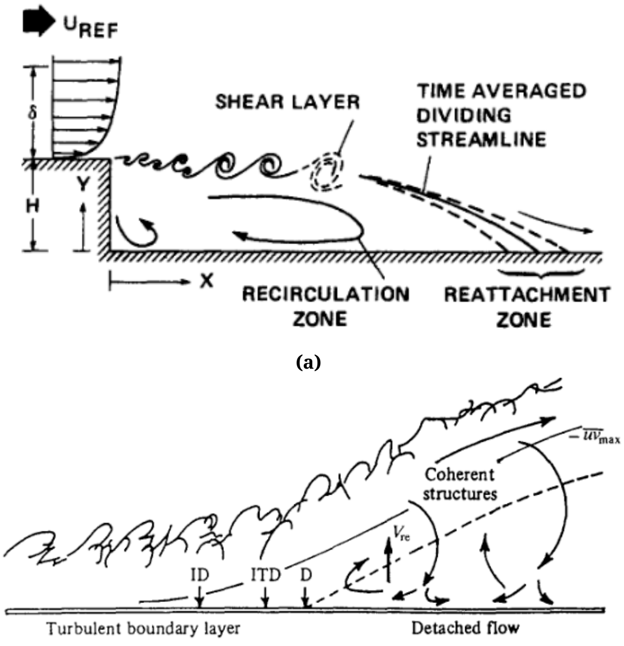

(a)

(b)

Figure 2.3: Illustrations of: (*a*) Features of a backward-facing step flow [From Driver et al. (1987)], (*b*) Pressure-induced boundary layer detachment process on a flat plat [From Simpson (1996)]

In a steady freestream with separating TBL over a low-curvature or flat surface, the mean flow upstream of the ID point adheres to the law of the wall and the law of the wake, provided that the maximum shearing stress remains below $1.5\tau_w$. Sandborn and Kline (1961) observed that a family of power-law-type mean-velocity profiles closely fits regions with significant intermittent backflow. This family of profiles is characterized by the relation:

$$h = \frac{H-1}{H} = \left(2 - \frac{\delta^*}{\delta_{99}}\right)^{-1} \tag{2.11}$$

According to Simpson (1989), in flows near equilibrium that satisfy the Coles velocity profile model, ITD occurs at $\delta^*/\delta = 0.42$ and $H = 2.70$. Alternatively, another widely used parameter for quantifying the pressure gradient is the Clauser pressure-gradient parameter, where a value of $\beta > 30$ typically indicates upcoming boundary layer separation.

Typically, pressure-induced separation has been studied extensively in two-dimensional flows. Low-speed diffusers are a good example of essentially pressure-induced TSBs, which is why most of the literature focuses on this topic, see Kaltenbach et al. (1999), Buice and Eaton (2000), Herbst et al. (2007). Recent efforts have been devoted to studying these flow conditions also in three-dimensional diffusers in order to provide accurate and detailed information on the flow physics of pressure-induced separation. For example, Ohlsson et al. (2010) present the direct numerical simulation (DNS) of a separated flow in a 3D diffuser, offering valuable insights into this complex phenomenon.

2.3.2. Flow reattachment

In the context of boundary layer behavior, particularly as it departs from a surface, it is pertinent to also consider the implications of this phenomenon further downstream the separation point. If a favorable pressure gradient is recovered past the separation point, then the flow may reattach. However, a favorable gradient alone may not always be enough for reattachment. As discussed in Section 2.3.1, the separated shear layer undergoes significant changes in the reattachment zone, the flow sharply bends downward to reattach to the surface, leading to APGs and significant disturbances due to its proximity to the wall.

Westphal et al. (1984) reports a significant backflow close to the surface under the separated shear layer before reattachment. The substantial value of the backflow skin-friction coefficient indicates that the flow near the wall exhibits characteristics similar to laminar flow, particularly at the Reynolds numbers considered in this and earlier research.

According to Simpson (1996), in the case of flow reattachment downstream of a geometrical singularity such as a backward-facing step, the distance from the step to the reattachment spot ($\gamma_{pu} = 0.5$ and $C_f = 0$) serves as an important length scale for normalizing streamwise positions. Additionally, the ratio of reattachment length to step height (X_R/H) in such scenarios is notably influenced by the expansion ratio (ER), exhibiting significant Reynolds number dependence under certain conditions. Nevertheless, instantaneous reattachment locations can vary streamwise by multiple times the step height. For instance, DNS of a backward-facing step by Le et al. (1997) at $Re_H = 5100$ and ER$= 1.2$ indicates mean instantaneous reattachment location occurring at $6.28H$ from separation.

Despite a significant increase in Reynolds stresses as reattachment is approached, downstream of the reattachment point, Reynolds stresses decay rapidly over several step heights. Meanwhile, a new sub-boundary layer begins to form within the reattached shear layer. Empirical evidence suggests that even up to approximately 50 step heights downstream of reattachment, the outer portion of the reattached shear layer retains characteristics typical of a free-shear layer, highlighting the persistence of eddies originating within the initially separated free-shear layer.

3

Separation control using vortex generators

This chapter provides a review of research findings and concepts relevant to the use of vortex generators (VGs) for controlling flow separation, a critical aspect to enhance aerodynamic performance. Section 3.1 begins with an overview of various methods of control, setting the context for the application of vortex generators. Section 3.2 distinguishes between passive and active vortex generators, detailing their respective mechanisms and operational differences. A comparative analysis follows, highlighting the advantages and limitations of each type. Finally, Section 3.3 delves into vortex dynamics, exploring the underlying physical processes that govern the effectiveness of vortex generators in mitigating flow separation. This comprehensive examination provides a solid foundation for understanding the role of VGs in flow control applications.

3.1. Methods of control

Flow control poses challenges in both industrial and academic domains, aiming to enhance device performance in various sectors like aeronautics, automotive, naval, chemical, and energy production. Lachmann (1961) defines boundary layer control as *any method altering boundary layer behavior from its natural development on a smooth surface*. Examples include: delaying or triggering laminar-to-turbulent transition, managing separation, modulating skin friction or pressure drag, regulating heat transfer, optimizing lift generation, and manipulating acoustics (Gad-el-Hak and Bushnell 1991). Among these, controlling flow separation is crucial for aerodynamic devices, reducing energy losses and enhancing performance, especially in high-load scenarios.

The two-dimensional integral boundary layer (IBL) approach elucidated by Drela (2014), offers a theoretical framework for understanding separation control mechanisms (see Appendix A). Increasing the maximum tolerated pressure gradient, or conversely, minimizing the most negative streamwise velocity gradient helps prevent boundary layer separation. This can be achieved by increasing dissipation, notably through enhancing turbulent kinetic energy. This is precisely the effect of vortex generators (Lengani et al. 2011).

The primary focus of this project is delaying flow separation by enhancing mixing and restoring lost momentum near the wall, ultimately minimizing or preventing separation within an APG. Schubauer and Spangenberg (1960) demonstrated the efficacy of various mixing devices in mitigating separation in TBLs, enabling them to withstand more substantial pressure gradients, thus delaying or preventing separation. Various approaches can achieve this goal by enhancing vorticity magnitude near the wall, as discussed by Ashill et al. (2002):

- Enhancing mixing between upper and lower boundary layers, such as using vortex generators.
- Directly increasing energy in the lower layers, e.g., through tangential blowing near the wall.
- Introducing vorticity within or just above the boundary layer, with opposite sign to that at the wall, to increase velocity in this region.
- Mitigating the APG upstream of the separation point, often achieved through body shaping.

In particular, in the field of external aerodynamics, flow control mechanisms to prevent boundary layer separation are classified into two categories: passive and active flow control. Passive flow control (PFC) techniques, like vortex generators, operate without external power, are simple and low-maintenance, and widely used for delaying separation, according to Ashill et al. (2005). Active flow control (AFC), requires an energy input, but offers advantages such as adaptability and deactivation when not needed but is more complex due to actuators. Key AFC techniques include tangential blowing and suction to add or remove momentum near the wall according to Lengani et al. (2011).

3.2. Vortex generator devices

3.2.1. Passive vortex generators

Fixed vane-type vortex generators are commonly used to control flow separation on commercial aircraft wings. These devices consist of small plates oriented perpendicular to the surface, generating streamwise trailing vortices that enhance mixing between the outer flow and near-wall region, reducing separation risk (Baldacchino 2019). Early research by Taylor (1947) laid the foundation for understanding vortex generator physics, followed by significant contributions from Gould (1956), Jones (1957), Schubauer and Spangenberg (1960), and Pearcey (1961). Research in subsequent decades, notably by NASA and Stanford, furthered understanding of vortex generator properties and design methodologies. Introduction of Particle Image Velocimetry (PIV) in the 2000s allowed for very detailed studies of vortex generator structures and their effectiveness (Lin 2002; Godard and Stanislas 2006; Lögdberg et al. 2010; Lengani et al. 2011).

Early vortex generators were typically larger than boundary layer thickness, resulting in strong vortices, three-dimensional flow structures, and increased drag. Recent studies favor smaller configurations, smaller than δ and sometimes as small as 0.2δ, strategically placed within the inner logarithmic region of the boundary layer where $y^+ < 300$. Despite their shorter vortex lifespan, these smaller vortex generators effectively control separation while inducing lower drag compared to larger ones (Lin 2002). Optimal deployment of sub-boundary layer vortex generators near the separation region requires stability in the separation region.

3.2.2. Active vortex generators

Active flow control devices offer the advantage of on-demand operation, avoiding drawbacks like additional drag during cruise flight, unlike passive techniques. Gad-el-Hak and Bushnell (1991) outlines active momentum addition techniques involving: discrete blowing or injection to generate streamwise vortices, increase turbulence/Reynolds stress with dynamically activated devices, and injection of high-velocity fluid tangentially. Control of vortex generators depends on the actuator type, including acoustic, plasma, and fluidic actuators. Fluidic actuators, particularly synthetic jets and pulsed-jet actuators, are the most commonly used options.

Synthetic jets, also known as Zero Mass Flux (ZMF) jets, transfer linear momentum to the flow system without mass injection across the flow boundary (Glezer and Amitay 2002). They generate periodic alternating pressure drops across an orifice using acoustic waves or diaphragm/piston motion. Pulsed-jet vortex generators produce periodic bursts of jets to initiate vortical structures within the boundary layer. Operational parameters like pulsing frequency and duty cycle are crucial for optimizing performance (Ortmanns et al. 2008; Eroglu and Breidenthal 2001).

Pulsed jets offer advantages over continuous jets, including altering flowfield topology and showcasing initial velocity overshoot during start-up, contributing to a robust starting structure (Ortmanns et al. 2008). The discrete vortex ring structure enables greater penetration and stronger control effects with reduced mass flux requirements (Eroglu and Breidenthal 2001). Control impact primarily occurs during start-up, allowing for shorter duty cycles without adverse effects.

Various system parameters influence the efficacy of active vortex generators, including geometric characteristics, jet pitch, skew angles, orifice shape, and spacing, as well as velocity ratio and pulse duty cycle (Kostas et al. 2007).

3.2.3. Comparison

The choice between passive and active vortex generators plays a key role in determining the effectiveness of boundary layer management. Each approach offers a unique set of advantages and disadvantages. Passive vortex generators are known for their simplicity and lack of auxiliary power requirements, while active vortex generators provide enhanced control and adaptability. However, the decision between these techniques should be made carefully, as both have their limitations. Table 3.1 provides a concise overview of the key advantages and disadvantages associated with each method.

3.3. Vortex dynamics

Shifting the focus towards the vortical fluid dynamics *downstream* of vortex generators, investigations by Velte et al. (2016) have presented the intricate interplay between viscous effects near the wall and the emergence of complex vortex systems. These revelations underscore the need to extend the knowledge beyond idealized monopole flows.

In the study by Wendt et al. (1993), the downstream development of embedded vortices is compared to that of isolated vortices, revealing several key differences. Isolated vortices maintain their circulation as they progress downstream, whereas embedded vortices experience a decrease in circulation due to the wall's influence. This reduction is attributed to a

Table 3.1: Advantages and disadvantages of passive and active vortex generators.

	Advantages	Disadvantages
Passive VGs	• Simple setup • No need for auxiliary power and hardware • Moderate sensitivity to arrangement	• Continuously protrude into the flow • Cannot be turned off when not needed • Potential additional parasitic drag
Active VGs	• Can be turned off when not needed • Enhanced control and adaptability • Potential for improved performance	• Complex setup and control • Require auxiliary power and hardware • High sensitivity to arrangement and settings

spanwise component of wall shear stress that generates a torque opposing the vortex rotation.

Additionally, the growth of the core radius is significantly greater in embedded vortices than in isolated ones with the same Reynolds number. This accelerated growth is likely due to enhanced diffusion within the vortex core, driven by the turbulent boundary layer, and increased turbulence intensity inside the core region, caused by a streamwise velocity deficit or wake. Furthermore, the core vorticity profile of isolated vortices remains circular, while embedded vortices exhibit elliptically shaped profiles downstream. This ellipticity could result from the presence of the wall or indicate unsteady phenomena like vortex oscillation or meandering.

In the particular case of two counter-rotating vortices in close proximity to each other, the interaction with the wall introduces a shearing effect, which is only partially mitigated by the presence of the opposing vortex. Vortices in a common upwash configuration tend to direct the secondary flows upwards, away from the wall, causing the vortices to rise rapidly due to the mutual interaction and thus reducing the wall shearing effect. Beyond a certain distance, the overlapping of vortices causes dissipation, altering the strength and lateral displacement of the vortices. Contrarily, vortices in a common downwash configuration direct the secondary flows towards the wall, leading to their trajectories diverging in the spanwise direction without moving far away from the wall.

To comprehend the temporal evolution of vortices in the wake of vortex generators, it is imperative to examine the phenomenon of vortex decay. Ashill et al. (2005) presents an investigation into the decay of vortices, considering factors such as device height, deflection angles, and streamwise positions. Their findings reveal that generally the vortex height increases with streamwise distance. This insight prompts researchers to consider the influence of the wall-induced vorticity layer, as depicted in Figure 3.1a. The intricate relationship between vortex height, streamwise position, and the induced vorticity layer highlights the complexity of modeling accurately vortical flows, as evidenced by the empirical adjustments made in their study.

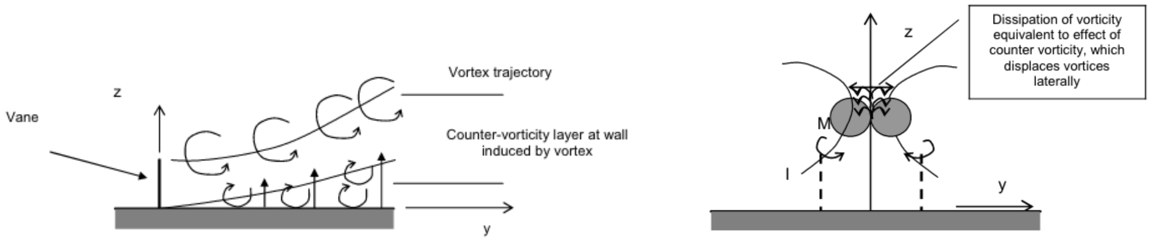

(a) **(b)**

Figure 3.1: Illustrations of: (*a*) Counter-vorticity layer at wall induced by vortex; (*b*) Flow over split vanes showing the dissipation of vorticity. [From Aider et al. (2010)]

Focusing on the topology of the vortex systems generated by vortex generators, research exemplified by Velte et al. (2012), consistently identified a basic vortex system constituted by the primary (wing tip) vortex and a horseshoe vortex generated from the roll-up vortex around the leading edge of the vane. This topology, reproduced in Figure 3.2, comprises the primary vortex (P) shed by the VG wing tip and the pressure side and suction side horseshoe vortices (H_P and H_S, respectively). Generally, the primary vortex tends to capture and sweep the suction side horseshoe vortex of opposite rotation beneath it during its early formation. On the other hand, the pressure side horseshoe vortex often evolves without significant disruption from the rest of the vortex system. Under certain circumstances though, the disturbance introduced by the vane might not be strong enough, and this can cause both sleeves of the horseshoe vortex to merge into a unique vorticity track, generating one unique primary structure (Velte et al. 2016).

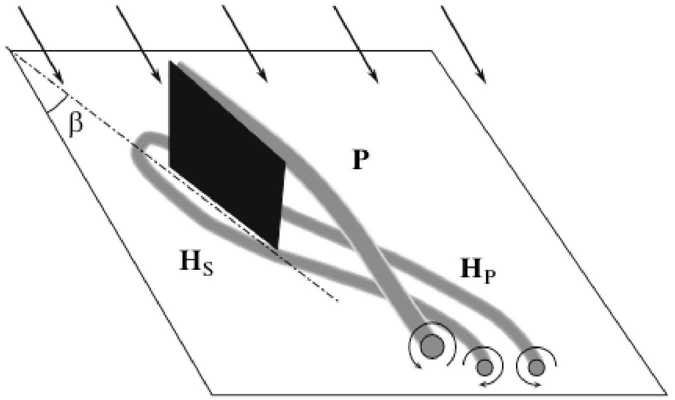

Figure 3.2: Topology of the basic vortex structure [From Velte et al. (2012)]

Nevertheless, measurements conducted using SPIV show that, in certain flow configurations, beyond the basic vortex system, secondary vortex structures can arise due to localized boundary layer separation in the lateral direction between the primary vortex and the wall. These secondary structures can draw vorticity from the primary vortex, altering the characteristic variation of the strength with u_{VG}. Notably, the presence of these structures relies heavily on the geometric arrangement of the vortex generator system, especially the vane's angle and height, and the Reynolds number. In some instances, the arrangement of counter-rotating vortex generators in cascade can be employed to eliminate secondary structures, impacting the boundary layer control. The article depicts four predominant states observed through measurements, offering an overview of their development in the wake via streamwise vorticity plots, as depicted in Figure 3.3.

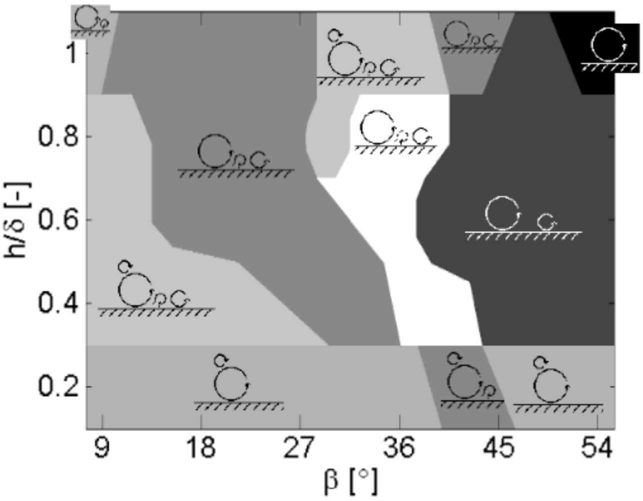

Figure 3.3: Regime map of the different vortex structures in the far wake [From Velte et al. (2016)]

Moreover, according to studies such as Ashill et al. (2005), APGs have a pronounced impact on vortex characteristics. In cases of single and spaced vanes, changes in vortex strength downstream of the device are associated with variations in wall friction velocity. However, when vanes are joined, an additional adverse effect arises, likely related to boundary layer separation upstream of the device. APGs promote the growth of vortices, causing them to merge earlier upstream in counter-rotating devices. Adjusting vane spacing proves effective in mitigating this adverse tendency, emphasizing the role of geometric configurations in optimizing vortex behavior under adverse pressure conditions.

4

Vortex generator design concepts

This chapter provides an overview of vortex generator design concepts and guidelines, examining various design trends. Section 4.1 begins with an introduction to the fundamental concepts underlying VG design, providing the necessary theoretical background. This is followed by Section 4.2, which provides a discussion on conventional vortex generator designs, highlighting their characteristics and typical applications. Section 4.3 examines sub-boundary layer vortex generators, detailing their design considerations and performance benefits. Finally, Section 4.4 investigates deployable vortex generators, exploring their innovative design features and potential advantages in dynamic flow environments. This comprehensive overview of VG design concepts aims to facilitate a deeper understanding of their roles in flow control strategies, and highlight the potential of deployable VGs as an alternative to active systems.

4.1. Fundamentals of VG design

The downstream evolution of the streamwise vortices and the effectiveness of flow control are significantly impacted by multiple VG design parameters. These variables can be classified into two categories: vane shape and array setup, as illustrated in Figure 4.1. According to the literature, the most influential variables are:

- Vane form.
- Vane height h. Commonly expressed as a fraction of the boundary layer thickness, h/δ.
- Vane length L. Commonly expressed as the length-to-height aspect ratio, L/h.
- Skew angle β.
- Intra-spacing d. Commonly normalized with the vane height, d/h.
- Inter-spacing D. Commonly normalized with the vane height, D/h.
- Streamwise position x_{VG}. Considered as the distance from the baseline separation point, and normalized with the vane height, $\Delta x_{VG}/h$.

Moreover, common configurations of vortex generator arrays can be categorized into two primary classes. In the *co-rotating* (CoR) arrangement, all blades have consistent angles of

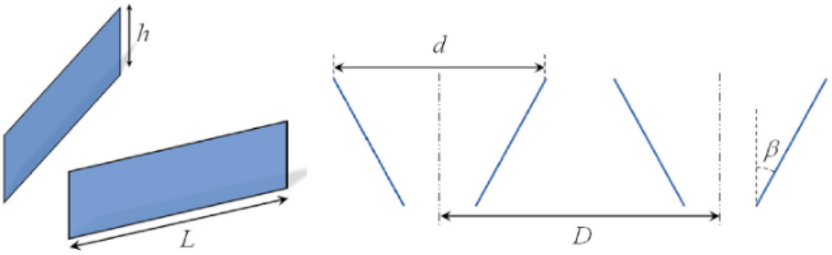

Figure 4.1: Conventional VG configuration of the counter-rotating rectangular vanes. (*left*) Isometric view; (*right*) Planar view. [From Zhu et al. (2023)]

attack relative to the stream direction, leading to trailing vortices with uniform circulation. As a consequence, the low momentum fluid is transported away from the wall, whereas the high momentum fluid is directed towards the wall. In the *counter-rotating* (CtR) arrangement, blades are arranged in a single row with alternating angles of attack, resulting in the induction of trailing vortices with opposite circulation about adjacent blades. As a consequence, the high momentum fluid is transported towards the wall between devices of the same pair, contributing to a thinner boundary layer in this region, and away from the wall between two pairs, contributing to a thicker boundary layer (Gould 1956, Cathalifaud et al. 2009). Both configurations are depicted in Figure 4.2.

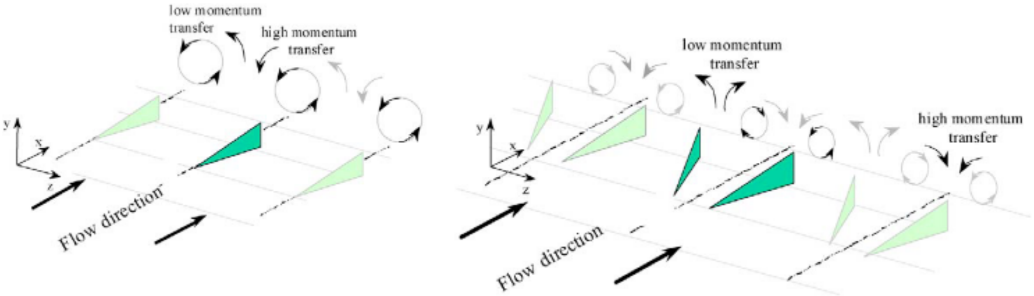

Figure 4.2: Conventional VG configuration. (*left*) Co-rotating triangular vanes; (*right*) Counter-rotating triangular vanes. [From Godard and Stanislas (2006)]

4.2. Conventional VGs

Shifting the focus towards the so-called conventional concepts of vortex generators, the concept of passive vortex generators has a long history, and its initial demonstration for controlling separation dates back to Taylor (1947). In his work, H. D. Taylor introduced the concept of traditional passive vortex generators, characterized by vane-type structures with a height on the order of magnitude of the boundary layer thickness ($h \sim \delta$). These devices typically featured a series of small plates or airfoils that protrude perpendicular to the surface and are set at an angle of incidence (β) relative to the local flow, in order to generate a sequence of streamwise trailing vortices.

The vortex system generated by a VG vane is predominantly characterized by its vortex strength, decay rate, and trajectory. These specific parameters have been employed by many researchers as indirect measures to evaluate the performance of vortex generator designs. Gould (1956) established a metric to assess the effectiveness of VG designs by considering the flow of streamwise momentum in the direction normal to the wall, taking into consideration factors such as image vortices, spacing between VGs, the impact of diffusion, and vortex trajectories. Based on this, Gould's design recommendations suggested that: the optimal spacing between VG pairs should be approximately 6 times the vane height ($D = 6h$), with a ratio of the vane pair inter-spacing (D) to the vane intra-spacing (d) close to $D/d = 3$. Additionally, the author suggested angles of incidence within the range of $15°$ to $20°$. For scenarios involving incipient separation within $15h$ of the VGs, a counter-rotating configuration with a common downwash was advised. These design criteria closely align with those proposed by Godard and Stanislas (2006) through experimentation approximately 50 years later.

Some years later, Pearcey (1961) examined a wide range of vortex generator configurations and expanded these design recommendations, providing design guidelines for both co-rotating and counter-rotating arrangements. The study suggested that counter-rotating VGs with a common upwash configuration resulted inefficient, compared to a common downwash arrangement, due to premature vortex ejection, resulting in a low near-wall residence time. While CtR VG arrays offered potential for separation elimination, they were also noted to be more complex to optimize. In contrast, CoR VGs, were identified as better suited for situations where the local flow direction is unpredictable or subject to change. These CoR VGs demonstrated versatility and adaptability, making them a favorable choice in environments where flow characteristics may vary.

Specifically, concerning the versatility of vortex generators in controlling separation, subsequent investigations conducted by Lögdberg et al. (2010) explored how sensitive the control mechanism is to variations in the dimensions and placement of the TSB relative to the VGs. These studies made use of counter-rotating, common downwash VGs and revealed that the use of vane-type arrays is robust when facing alterations in pressure gradients and shifts in separation points. However, if the system is optimized for maximum efficiency, it might show sensitivity to changes in flow conditions at the location of the VG array.

Figure 4.3 presents a variety of VG design concepts, as discussed in studies such as Lin (2002) and Kleissl (2013), which can be adapted to different contexts. Among these, vane-type designs are the most widely used, especially in aeronautical applications. The focus of this report is on VGs capable of being implemented using shape memory alloy actuation. This constraint necessitates simple structures. Consequently, this report will focus specifically on vane-type and wedge-type VGs, as these shapes can be achieved with a simple deformation of a flat plate.

4.3. Sub-Boundary Layer VGs

The use of conventional vortex generators of considerable size, on the order of the boundary layer thickness, has been a common practice in aerodynamic applications to prevent localized flow separation. However, this can lead to increased residual drag. Therefore, recent studies have focused on reducing the drag caused by VGs. It has been observed that smaller VGs tend to generate less form drag, hence this has led to the increasing popularity of actuators with a relative height $h/\delta < 1$, which are referred to as low-profile, embedded, submerged, or sub-boundary layer VGs (SBVGs). These devices can be advantageous in situations where the separation point is relatively fixed and there is *no need to cover a long downstream distance*.

Lin (2002) provides valuable insights into this area. In this study, the author reviews several research efforts on boundary layer flow separation control using SBVGs with $0.1 \leq h/\delta \leq$

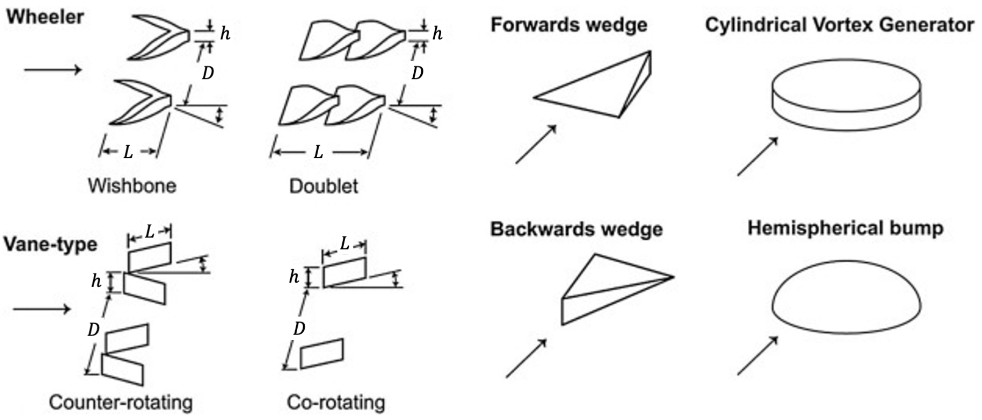

Figure 4.3: Multiple vortex generator designs. [Adapted from Kleissl (2013) and Lin (2002)]

0.5. The effectiveness of SBVGs in managing flow separation, within a limited downstream span, is evident when placed approximately $100h$ upstream of the baseline separation point. However, when compared to conventional VGs, they require adjustments in parameters like the vane aspect ratio (L/h), the inter-separation (D/h), and the skew angle (β) to ensure the generation of strong enough streamwise vortices for effective flow control.

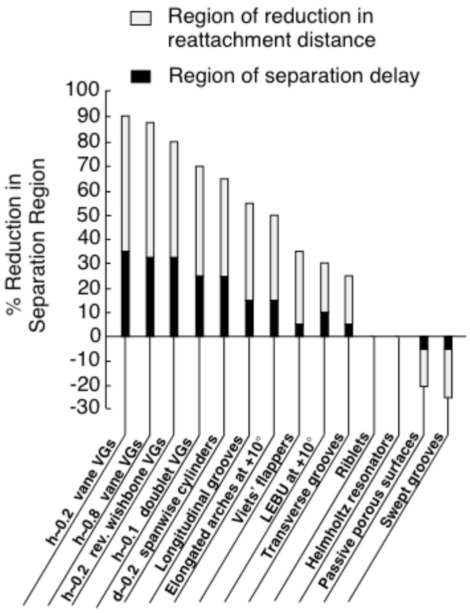

Figure 4.4: Summary of relative flow separation control effectiveness for different VG design concepts. [From Lin (2002)]

In Figure 4.4, an overview of the relative flow control effectiveness of the devices examined in Lin's study is presented. The diverse geometries and VG designs are also depicted in Figure 4.3. In terms of performance across distinct flow regimes, SBVGs prove effective in both two-dimensional and three-dimensional flow separation scenarios. Specifically, counter-rotating VGs show superior performance in two-dimensional flow separations (such as those on a curved ramp), while co-rotating VGs excel in three-dimensional flow separations (such as those on swept wings or inside compact-duct inlets).

Additionally, Lin (2002) also studies a set of different vane shapes, including rectangular, triangular, and trapezoidal profiles. Among these, trapezoidal devices emerge as the preferred choice for low-speed applications, particularly in controlling separation on aircraft wings. Triangular and rectangular vanes produce comparable vortices, but the latter introduce undesirable extra drag.

Based on the design guidelines presented by Lin, later studies from Godard and Stanislas (2006) presented a detailed parametric study of passive VGs for both CtR and CoR configurations. This optimization study is based on the criteria of the skin friction improvement ($\Delta\tau/\tau_0$) relative to the skin friction without actuation at the location of minimum skin friction coefficient ($C_{f_{min}}$) along a 2D bump (which mimics the APG on the suction side of an airfoil close to separation). This test campaign led to optimal configurations which are presented in Table 4.1 for both arrangements. These insights will provide the foundational baseline for designing the vortex generators investigated in the current research.

	VGs	h/δ	$\Delta X_{VG}/h$	L/h	d/h	D/h	β [°]	$\Delta\tau/\tau_0$ [%]	
								Min.	Max.
CtR	Triangular vanes	0.37	57	2	2.5	6	18	110	200
CoR	Triangular vanes	0.37	57	2	–	6	18	55	105

Table 4.1: Optimal parameters for both configurations of passive devices. [Adapted from Godard and Stanislas (2006)]

4.4. Deployable VGs

Fixed-vane vortex generators have been a longstanding and effective tool as flow control devices for more than half a century. Despite their established utility, a significant limitation emerges: optimizing fixed VGs for improved performance in one flow regime frequently results in performance penalties under different conditions. Consequently, ongoing efforts are dedicated to the development of VGs that can be selectively deployed *on demand*.

One example of a deployable vane actuated by means of a mechanical system is presented in the work of Aider et al. (2010), which explores the implementation of active vortex generators on a 3D bluff-body. In their study, the authors introduce an innovative configuration featuring *motorized* vortex generators, leading to a substantial reduction in both drag and lift. Notably, the VGs under study possess an unconventional geometry compared to the typical vane-type VGs employed in aeronautics. Vorticity generation is initiated by the formation of a horseshoe vortex around the VG's base, facilitated by a junction flow mechanism. Interaction among the arms of these horseshoe vortices ultimately results in the generation of pairs of counter-rotating longitudinal vortices, with the potential to modify boundary layer characteristics depending on the device spacing. Figure 4.5a provides a representation of two vortex generators, along with the associated inflow and outflow regions formed between the counter-rotating vortices.

Another noteworthy example of a deployable VG system is presented in the research conducted by Le Pape et al. (2012). Their work explores the implementation of *active* dynamic stall control based on leading-edge vortex generation. The actuator designed in this study consists of a row of deployable vortex generators, each comprising small blades positioned

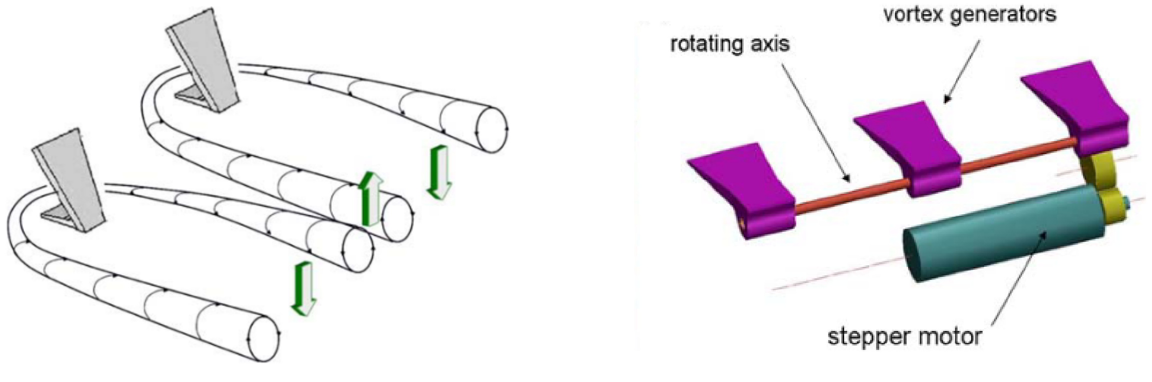

(a) **(b)**

Figure 4.5: Active vortex generator system from Aider et al. (2010). (*a*) Vortex generators together with the induced streamwise counter-rotating vortices; (*b*) Motorized rotating axis system. [From Aider et al. (2010)]

at the leading edge of the airfoil, as depicted in Figure 4.6. These blades conform to the airfoil shape when retracted. The height of the actuators can be actively controlled, enabling adjustments in height, phase, and frequency concerning airfoil oscillation. The focus of this study is not to dynamically generate vortices on a static airfoil configuration but to deploy, when needed, the VGs on an oscillatory airfoil. This feature offers flexibility in achieving various trade-offs between lift and pitching moment, contingent on the phase actuation of the deployable VGs. For a more detailed exploration of flow control through dynamic vane VGs, the study by Barth et al. (2011) provides comprehensive insights, in this case employing piezoelectric actuators.

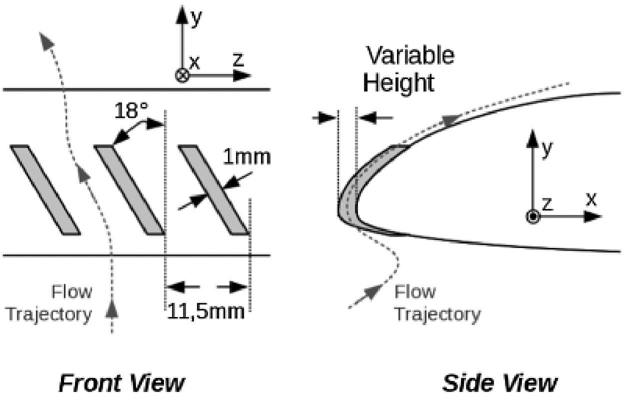

Figure 4.6: Sketch of deployable vortex generator system from Le Pape et al. (2012). [From Le Pape et al. (2012)]

Nevertheless, a notable drawback associated with the aforementioned approaches is the necessity for ample space and an energy supply to accommodate the motors and mechanical components essential for controlling VG actuation. For instance, the method described by Aider et al. (2010) requires a complete mechanical system to actuate the VGs. Similarly, Le Pape et al. (2012) not only requires a mechanical system but also a complex control system to actuate the VGs at the correct height, phase, and frequency. Due to these limitations, another subset of vortex generators, which includes deployable vanes using Shape Memory Alloy (SMA) actuation, presents a compelling alternative. This relatively less explored category offers the advantages of active systems while eliminating the need for mechanical couplings, hinges, and additional hardware.

Over the past two decades there has been a growing demand for compact and intelligent structures in a variety of applications, including mechanical, biomedical, and structural domains. Integration of SMAs into composite materials has led to the emergence of smart composites (SCs), which are characterized by their ability to monitor and respond to environmental stimuli within a single compact structure (Santosh et al. 2022). These SCs offer a range of functionalities, such as self-healing, vibration control, and actuation by shape or position control. This project focuses on SC actuators, which are powered by SMAs and offer a lightweight, compact, and reliable alternative to traditional actuators, presenting immense potential for addressing technical challenges in multiple fields.

In particular, this project focuses on the design and evaluation of a specific type of SC actuator: the bending actuator employing SMA wires. This choice is based on the broad applicability of bending actuators shaped as vortex generators in the context of flow separation control. The significance of a bending SC actuator is explained through studies by Lee et al. (2019), who investigated the shape control of a composite beam with embedded SMA wire actuators. Their findings underscored the shape control capability of SMA wire actuators and their influence on the behavior of composite structures under different loading conditions. The potential for precise control, lightweight construction, and the unique properties of SMAs, such as shape memory effect and pseudoelasticity, further reinforce the rationale behind the focus on bending SC actuators. Figure 4.7 shows a schematic drawing as well as an example of a cured SC actuator.

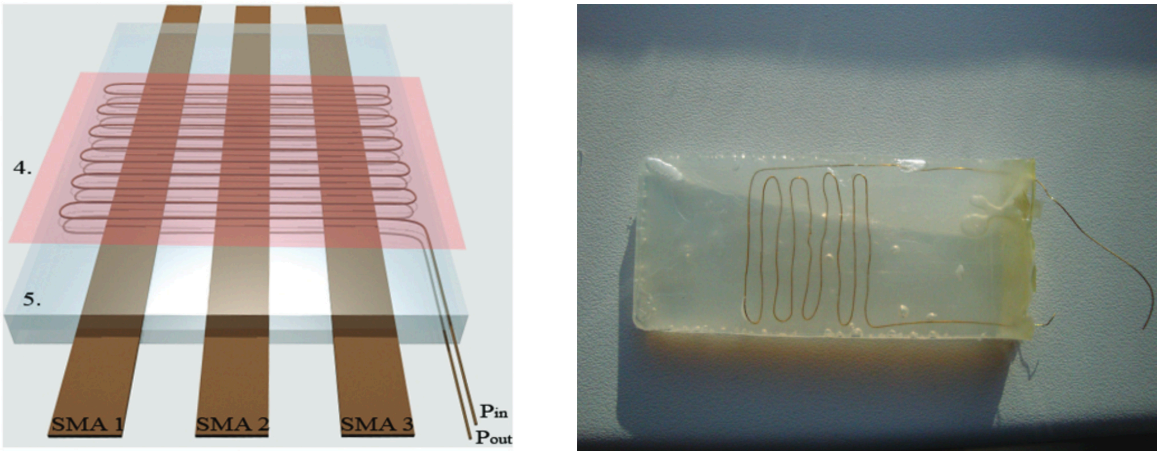

(a) (b)

Figure 4.7: SC with SMP body. (*a*) Schematic drawing: *4.* Heating area with embedded heating wires, *5.* SMP body; (*b*) Cured SMP. [From Lelieveld et al. (2016)]

One pioneer example of this approach is the concept presented by Barrett and Farokhi (1996), where a ramp VG configuration integrated with SMA actuators, a shear-flow stall sensor, and an optimal controller were combined to form a smart vortex generator (SVG) system. This system was able to generate a significant increase in α_{stall} and $C_{l,max}$ over a NACA 4415 airfoil while inducing a negligible rise in C_{d0} with very little weight and power consumption. The versatility of the smart vortex generators was underscored by their ability to improve $C_{l,max}$ through two distinct modes of operation: either by actuating the VGs to modulate airflow at low angles of attack and facilitate a smooth transition through the stall regime, or by maintaining the VGs retracted during stall onset and subsequently deploying them to relieve stall effects on the wing.

Building upon this work, Ikeda et al. (2006) presented a similar approach to employing smart vortex generators, in which the deployment of VGs was optimized for specific flight phases. Leveraging the properties of SMA and exploiting the difference in temperature between cruising altitudes and ground conditions, this study proposed a mechanism for deploying VG arrays during critical flight phases such as takeoff and landing, while retracting them during cruise, thereby optimizing aerodynamic performance across varying operational conditions. In this case, this concept was demonstrated only with a simplified mathematical model and a conceptual demonstration model.

Subsequent studies, such as Quackenbush et al. (2010), have further expanded the scope of deployable vortex generator technology by focusing on the development of Pop-Up Vortex Generators (PUVGs) utilizing modified SMA wire actuators. Diverging from previous VG designs, PUVGs employ a self-locking, two-position mechanism, facilitated by a flat plate element notched to induce elastic buckling upon actuation. This innovative approach enables continuous deployment of VGs with minimal power requirements, as the self-locking mechanism obviates the need for sustained power input once the desired position is attained.

Moreover, in this study, the author lays the foundations for successful deployable vortex generators by outlining crucial requirements essential for their viability across both new and existing aircraft.

- Flush Stowage: The device must seamlessly stow flush with the mold-line of the mounting surface to maintain an aerodynamically sleek profile.
- Minimal Intrusion: The device should exhibit minimal intrusion below the mounting surface, ideally with no below-surface intrusion, ensuring unobtrusive deployment.
- Simplified Power Leads: The device must not require complex and bulky power leads, prohibiting the use of hydraulic lines or mechanical activation devices.
- Practical Control: Simple control and zero power requirement for holding position are deemed ideal for practical implementation, emphasizing ease of use and operational efficiency.

In agreement with these requirements, The study conducted by Nissle et al. (2018) proposed a system of adaptive vortex generators capable of hinging and lifting on demand, achieved through the combination of shape memory alloys and fiber-reinforced composites (FRP). As illustrated in Figure 4.8, the integration of SMA elements into flat FRP parts creates active hybrid composites. These lightweight active VGs, weighing around 1.5 grams each, can be seamlessly incorporated into the wing structure, requiring only an electrical connection for operation.

The study demonstrated that a tip deflection of 8 mm is achievable even under wind load, and that an overload scenario has minimal influence on the tip deflection. Furthermore, cyclic activation was conducted for 1000 cycles without any noticeable reduction in the maximum tip deflection or the heating time required to reach the maximum deflection. Experimental flight tests confirmed the functionality of the system, showing that the VG elements could be deployed within 10 seconds and remain in the deployed position for several minutes. Stowing the VG elements also took only 10 seconds, facilitated by the cooling effect of airflow.

These findings represent a promising path for the development of deployable vortex generators, aligning with the goals of this research in optimizing aerodynamic performance under

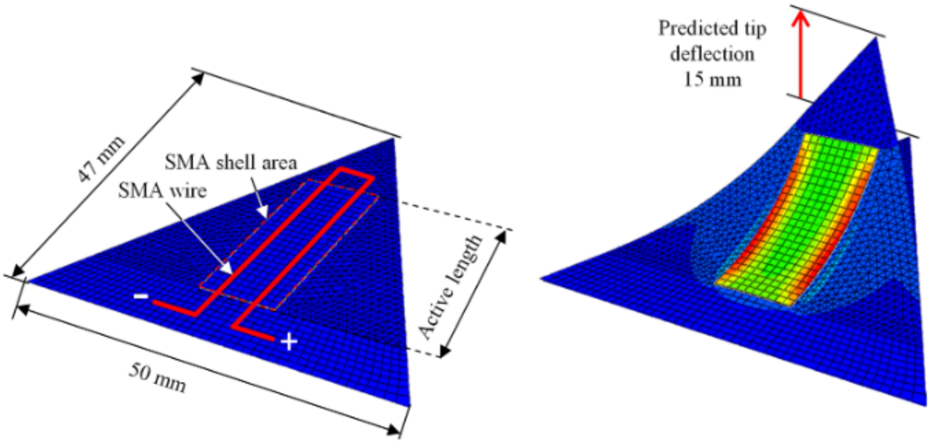

Figure 4.8: FE model of the deployable vortex generator system from Nissle et al. (2018). [From Nissle et al. (2018)]

challenging conditions and setting the baseline for the study presented in this report.

5

Summary

Flow control poses challenges in both industrial and academic domains, aiming to enhance device performance in various sectors like aeronautics, automotive, naval, chemical, and energy production. Among these, controlling flow separation is crucial for aerodynamic devices, reducing energy losses and enhancing performance, especially in high-load scenarios. The primary focus of this project is delaying flow separation by enhancing mixing between the upper and lower layers of the boundary layer and restoring lost momentum near the wall, ultimately minimizing or preventing separation within an APG.

A review of the state of the art in separation control has proved that vortex generators are the most common and well-established method to achieve this goal. Both passive and active vortex generators offer a unique set of advantages and disadvantages. Passive vortex generators are known for their simplicity and lack of auxiliary power requirements, while active vortex generators provide enhanced control and adaptability.

Deployable vortex generators using shape memory alloy actuation offer the potential to combine the advantages of both passive and active methods. However, existing research on passive vortex generators focuses heavily on traditional static devices, overlooking the improvements that shape-adaptive materials could bring to vortex generator performance. In particular, there is a lack of in-depth exploration into the relationship between aerodynamics and structural dynamics specific to deployable vortex generators. This knowledge gap is significant because static designs used in conventional passive vortex generators limit aerodynamic efficiency under different flight conditions. The recognized knowledge gap arises from the dynamic features of vortex generators constructed with shape memory alloys that allow them to retract and extend. This dynamic behavior suggests that the ideal aerodynamic configuration for these vortex generators may deviate from that of conventional static counterparts, particularly when the drag penalty is not a primary constraint for the design.

Therefore, this project aims to fill this knowledge gap by exploring the aerodynamic and structural difficulties of shape-adaptive vortex generators, particularly those utilizing shape memory alloys for retraction and extension. The goal of this project is to identify and achieve the optimal aerodynamic configuration, pushing the boundaries of conventional flow control methods and paving the way for new innovations.

Part II

Methodology

6

CFD methodology

This methodology chapter is structured into five key sections to comprehensively outline the approach and procedures employed in the CFD simulations presented in this report. Beginning with the modeling approach, Section 6.1 illustrates the theoretical framework guiding the simulation, including any simplifications or assumptions made. Subsequently, the Section 6.2 defines the metrics used to assess the accuracy and efficacy of the simulation results. Section 6.3 provides a detailed overview of the simulation environment, covering aspects such as the general details of the numerical method, geometry, boundary conditions, mesh generation, and the implementation of the turbulent modeling. Following this, Section 6.4 investigates the sensitivity of the results to variations in mesh resolution, ensuring the robustness of the numerical solution. Finally, Section 6.5 examines the fidelity of the numerical model through comparison with benchmark results and analytical solutions, confirming its accuracy and reliability for subsequent analysis and interpretation. Collectively, these sections establish a rigorous methodology for the numerical investigation of fluid dynamics phenomena, laying the groundwork for the analysis presented in this report.

6.1. Modeling approach

Most of the research concerning VGs is purely based on experimental studies, mainly involving wind tunnel measurements of backward-facing ramps, airfoils, and diffusers. As a consequence, there is a need for the development of computational tools that can assess the effect of VGs on the aerodynamic performance of multiple devices and allow the necessary modifications and optimizations without having to perform expensive full-scale experiments.

The simplest approach to investigate the impact of VGs in a flow simulation is to integrate them into the computational geometry and accurately compute the flow around each VG. Nonetheless, it is worth noting that this method demands significant computational resources. Furthermore, the challenges associated with accurately predicting TBL separation and reattachment using CFD are widely acknowledged. This complexity is particularly pronounced in cases of smooth-body flow separation, where intricate interactions between surface curvature and pressure gradients occur within the incoming boundary layer, as mentioned in Gray et al. 2023. Moreover, the process of modeling VGs itself is also considered a challenging task. The primary difficulty in simulating flow around VGs lies in their small dimensions, with vane heights often comparable with (or even smaller than) the local boundary layer thickness. Moreover, the intricate nature of three-dimensional vortical flows can introduce complexities, especially when employing eddy viscosity models in Reynolds-Averaged Navier Stokes (RANS) simulations (see Manolesos et al. 2016).

In response to these challenges, various approaches to VG modeling have been explored recently. According to Manolesos et al. (2020), VG models can be broadly categorized into three groups:

- Statistical Modeling. Such models focus on statistically representing the impact of the shed vortex (e.g., Stillfried et al. 2012 and Nikolaou et al. 2005).
- Vortex Profile Modeling. This category concerns modeling the profile of the vortex shed by the VG (e.g., Velte 2013, Zhang et al. 2011, and May 2001).
- Modeling VG Shape Influence. Here, the focus is on modeling the effect of the VG's shape on the flow (e.g., Jirasek 2005, Bender et al. 1999 and Smith 1994).

It is worth mentioning that, among all the aforementioned approaches for VG modeling, the Bender-Anderson-Yagle (BAY) model, as introduced by Bender et al. (1999), has stood out as the most favored approach, both in academic and industrial communities, for capturing the impact of VGs on the flow. This model's reputation primarily derives from its efficiency, straightforward implementation, and remarkable ease of use. The main concept behind this model is to include a source term that is dependent on the local flow into the momentum equations, based on the lifting surface theory.

Nevertheless, when using the BAY model in RANS simulations, the generated streamwise vortices may be relatively weak compared to those obtained from fully resolved (FR) simulations, even when using the same computational mesh. According to Florentie et al. (2018), this is because the BAY model assumes that the generated vortex can be described by an idealized-vortex model (usually the Lamb-Oseen model) combined with empirical relations. This method does not fully consider the specific characteristics of the situation of interest, such as the VG geometry. As a result, source-term VG models are advantageous for determining the optimal macroscopic properties of VG arrays, such as the streamwise location, but not as useful for VG shape determination.

In a relevant study, Spalart et al. (2015) conducted comprehensive simulations of flat-plate flow controlled by VGs, exploring both RANS and Direct Numerical Simulations (DNS). Their findings provide substantial support for the notion that RANS simulations can accurately capture the evolution of streamwise vortices generated by VGs over a flat surface. Given the focus of the current project on optimizing vane designs for shape-adaptive material VGs, the spotlight shifts to the specific geometry of the device. Consequently, the most promising path forward is the utilization of fully resolved RANS simulations over a flat plate.

6.2. Key performance indicators

To facilitate a comprehensive evaluation of the different design concepts of VGs, it is essential to establish a series of key performance indicators (KPIs). These indicators provide quantitative metrics for comparing different VG configurations and their effects on the flow field. In this chapter, a selection of KPIs based on a review of existing literature is presented, with the aim of identifying the most suitable metrics for this study.

Previous researchers have typically employed oil-flow visualization, streamwise pressure readings, and velocity-profile measurements to evaluate the efficacy of VGs in boundary-layer flow separation studies, such is the case in most of the studies reviewed by Lin (2002). Nevertheless, because the core emphasis of this numerical investigation centers on the impact of VGs in a flat plate configuration, the attention should shift toward the precise quantification of vortex development, their influence over the near-wall flow, and the associated loads imposed by their geometry.

Ashill et al. (2005) provides a set of parameters, known as vortex descriptors, used to characterize vortices. These descriptors encompass the strength of vortices immediately downstream of the device, the streamwise decay in vortex strength, and the vortex trajectories. These parameters, all quantifiable in numerical simulations, serve to evaluate the mixing efficiency of the vortices and streamwise extent of their effectiveness.

Furthermore, in the study by Godard and Stanislas (2006), due to the limited number of skin friction measurements available at the time, hot film probes were used to measure the wall shear stress in order to gain quantitative information on the efficiency of each configuration tested. These measurements were mainly conducted at the location of the minimum shear stress of the smooth configuration. The effect of the VGs was quantified by means of the parameter $\Delta\tau/\tau_0$, which represents the relative difference between the measured wall shear stress with and without VG actuation.

Finally, the primary objective of this project is to explore the application of shape-adaptive materials in the design of vortex generators. This innovative approach offers a significant advantage: VGs can be selectively deployed or retracted based on flight conditions. This adaptability minimizes the drag typically associated with these devices, thereby alleviating design constraints.

To evaluate the performance of the shape-adaptive VGs, the aerodynamic coefficients will be analyzed to characterize the actuator's response under varying flow conditions. Specifically, this involves assessing the trends in aerodynamic efficacy which can be related to the flow control capabilities. The analysis will focus on non-dimensional lift, drag, and lateral force coefficients to comprehensively evaluate lift, drag, and lateral forces:

$$C_L = \frac{L}{\frac{1}{2}\rho A U_0^2} \tag{6.1a}$$

$$C_D = \frac{D}{\frac{1}{2}\rho A U_0^2} \tag{6.1b}$$

$$C_Q = \frac{Q}{\frac{1}{2}\rho A U_0^2} \tag{6.1c}$$

However, in order to meet the material requirements, it is essential to measure the loads on the geometry, namely the normal (N), axial (A) and side (S) forces. For this specific test, the body axis measurements can be related to the wind axis measurements, namely lift (L), drag (D) and lateral (Q) forces, through the following equations (as depicted in Figure 6.1):

$$N = L \tag{6.2a}$$

$$A = D\cos\beta - Q\sin\beta \tag{6.2b}$$

$$S = Q\cos\beta + D\sin\beta \tag{6.2c}$$

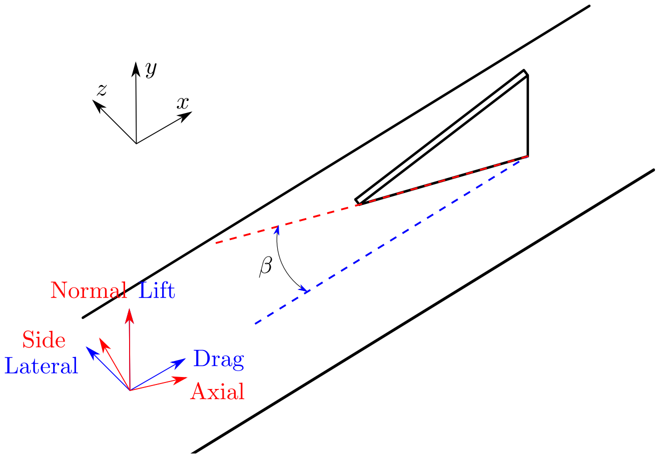

Figure 6.1: Vortex generator's coordinate systems: wind axis in *blue* and body axis in *red*.

Hence, the non-dimensional shape of normal, axial, and side forces will be monitored:

$$C_N = \frac{N}{\frac{1}{2}\rho A U_0^2} \tag{6.3a}$$

$$C_A = \frac{A}{\frac{1}{2}\rho A U_0^2} \tag{6.3b}$$

$$C_S = \frac{S}{\frac{1}{2}\rho A U_0^2} \tag{6.3c}$$

Overall, the chosen KPIs encompass vital aspects of the flow and collectively contribute to a comprehensive evaluation of VG performance:

- Vortex strength just downstream of the device: $|\omega_x|_{max}$.
- Vortex trajectories.
- Skin friction: C_f.
- Aerodynamic coefficients: C_L, C_D, C_Q.
- Normal, axial and side force coefficients: C_N, C_A, C_S.

6.3. Computational setup

The computational setup of this experiment takes inspiration from various previous studies of the effect of VGs on flat plate flow, see Fernández-Gámiz et al. (2012), Spalart et al. (2015), Fernández-Gámiz et al. (2016) and Manolesos et al. (2016).

6.3.1. General numerical method

The numerical simulation framework employed in this study is the open-source code OpenFOAM v2106, a computational tool widely acknowledged for its versatility and robustness in simulating fluid dynamics phenomena. In particular, the solver of choice is *simpleFoam*, a steady-state solver for incompressible, turbulent flow.

This choice is particularly apt for low-speed scenarios where the variation in fluid density across the computational domain is negligible, allowing for simplification of the governing equations and enhancing computational efficiency. Moreover, the interplay between the pressure and velocity fields is addressed through a segregated approach, specifically employing the SIMPLE (Semi-Implicit Method for Pressure Linked Equations) algorithm. This method decouples the pressure and velocity fields, iterating between them to achieve a consistent solution while ensuring mass conservation and enforcing the continuity equation.

While the natural evolution of the fluid flow phenomena under study is inherently unsteady, the simulation strategy pursued in this study opts for a steady-state approach. This decision, often necessitated by practical considerations such as computational resources and time constraints, offers the advantage of computational efficiency and stability, particularly in scenarios where transient effects may not be of primary interest or relevance.

6.3.2. Geometry

For the analysis of the skew angle sensitivity of the VGs, three primary actuator concepts were individually tested in isolation over a flat plate with zero pressure gradient: the single vane, the backward ramp, and the forward ramp.

The rationale behind selecting these specific models from the broad spectrum of VG concepts illustrated in Figure 4.3 stems from their perceived suitability for implementation using SMA actuation. These concepts are deemed more amenable to SMA actuation as the desired shape can be achieved through simple hinge motion along a single axis, without necessitating additional surface curvature. Moreover, in addition to these designs, in anticipation of potential future implementations, three secondary designs were examined: the curved vane and the hollow ramp (in both forward and backward configurations).

These additional designs aim to replicate a fully deployed VG, actuated by SMAs to attain an optimal form akin to that of solid devices. To emulate SMA actuation, the corresponding bending areas were incorporated to represent the hinge. The radius of curvature of the hinge of the curved vane is 1 mm, facilitating its positioning perpendicular to the ground wall, whereas the curvature of the hinge in the hollow ramp is slightly less pronounced, featuring a radius of curvature of 13 mm. A 3D sketch of all four of the tested geometries is presented in Figure 6.2. Comprehensive details of the tested geometries are available in Appendix C.

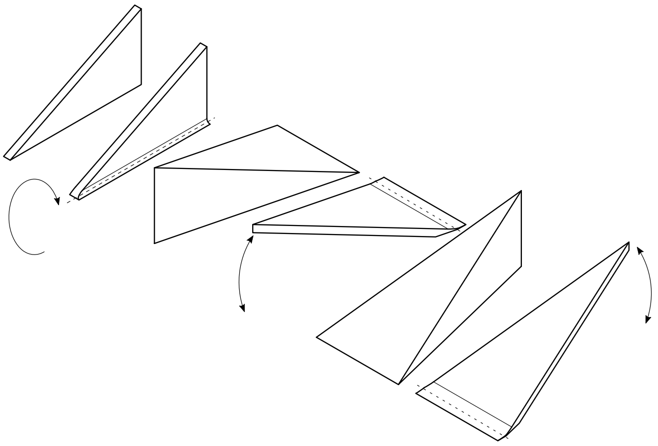

Figure 6.2: Tested geometries ($\beta = 0$ degrees). Left-to-right: single vane, single curved vane, backward ramp, backward hollow ramp, forward ramp, forward hollow ramp.

Regarding the design of the computational domain, Figure 6.3 illustrates the computational strategy proposed by Manolesos et al. (2016) to minimize computational demands in fully resolved modeling of vortex generators. By leveraging the geometric symmetry of counter-rotating VGs, the study focuses on resolving only one vane in a VG pair, applying symmetry conditions to the sides of the computational domain.

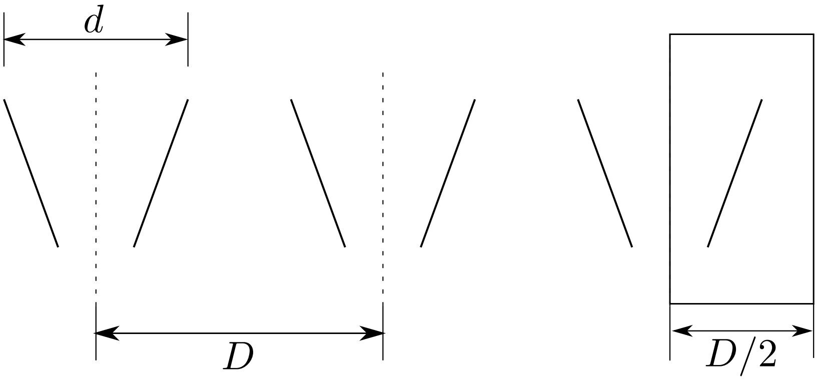

Figure 6.3: Sketch of the top view of a VG array. [Adapted from Manolesos et al. (2016)].

This approach is particularly effective for conducting skew angle sweeps and characterizing the sensitivity of the designs to the inflow angle in isolation. However, for the remainder of the study, which involves the analysis of full actuator arrays and subsequent comparison with experimental results, the influence of neighboring vanes becomes critically important. This influence affects vortex decay and the trajectories of the vortices. Therefore, to accurately capture the induced flow field, it is necessary to simulate at least one-half of the actuator array, using the central plane as a symmetry plane. Both scenarios are depicted in Figure 6.4.

The computational setups illustrated in Figure 6.4 feature a single VG and an array of VGs mounted on a flat plate where the dimensions of the domain are normalized based on either the VG height (h) or the vane inter-spacing (D). In this setup, the freestream flow aligns with the x-axis, the y-axis denotes the wall-normal coordinate, and the z-axis represents the spanwise coordinate. The VG shown is a triangular or delta vane with a length twice its height ($L/h = 2$). It is mounted on the wall at a position where the boundary layer thickness approximately matches the VG height ($h \approx \delta$). The same considerations are assumed for the isolated ramp concepts, with the only exception being the length-to-height ratio, which is increased up to $L/h = 2.5$. The rest of the details of the tested geometries are available in Appendix C.

6.3.3. Boundary conditions

The accuracy of CFD simulations strongly depends on the appropriate setting of boundary conditions. It is crucial to select and define boundary conditions meticulously to ensure that the simulation aligns with the physical realities it seeks to represent. Neglecting this aspect can lead to significant inaccuracies in the simulation results.

Figure 6.5 illustrates the specific boundary conditions relevant to the geometry under study, as outlined in the previous section. In this depiction:

- The inlet and outlet faces are designated as inlet and outlet surfaces, respectively. The inlet boundary condition is used to prescribe inflow properties such as velocity, pressure, and turbulence characteristics to establish the desired flow conditions. Conversely,

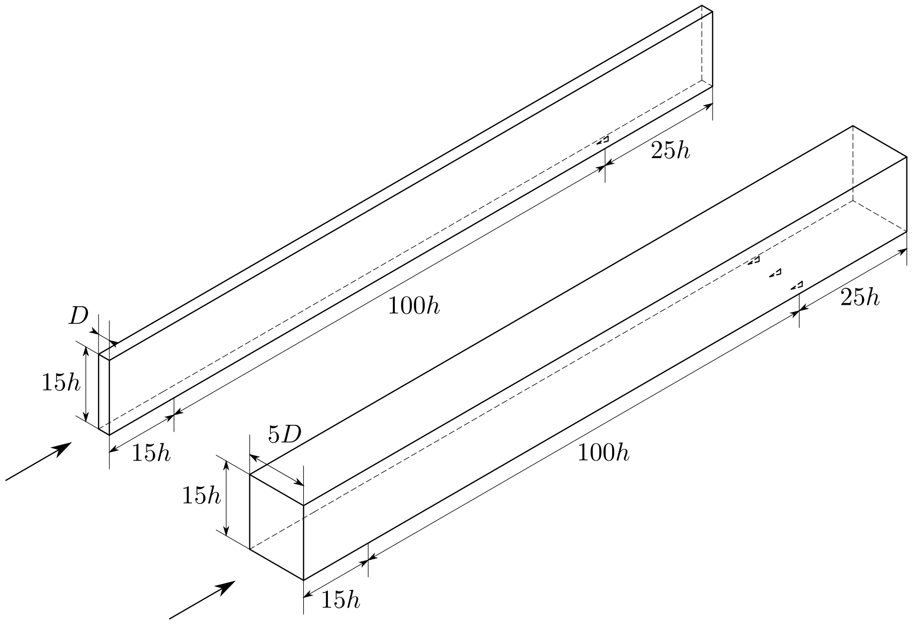

Figure 6.4: CFD computational domain: single vane (*left*) and half array (*right*).

the outlet boundary condition defines the behavior of the fluid as it exits the computational domain.

- A no-slip wall boundary condition is applied to both the flat plate and the VG walls to ensure adherence to the no-slip condition, where the fluid velocity relative to the boundary is null.
- A slip wall boundary condition is specified at the top face of the domain as well as at the precursor ground wall, enabling tangential movement of the fluid at the boundary to simulate infinite-extent conditions effectively.
- In cases where the individual VGs are studied in isolation over a flat plate, both lateral walls are defined as symmetry planes according to the approach proposed by Manolesos et al. (2016). This utilization of symmetry conditions takes advantage of the problem's symmetry, reducing computational effort. These conditions assume that fluid behavior across the boundary is symmetric, allowing for the extension of the domain infinitely spanwise, if needed. In cases where the full one-half of the domain is simulated, the symmetry plane remains defined using a symmetry boundary condition. However, the external lateral wall is also defined as a slip wall boundary to facilitate tangential movement of the fluid at the boundary and effectively simulate infinite-extent conditions.

6.3.4. Mesh

Considering the significance of flow characteristics near the VG and ground walls within the project's scope, mesh resolution is a critical factor. The grid system utilized in this study is generated using *cfMesh*, a software known for its robustness and simplicity in generating high-quality meshes for CFD simulations. The coordinate system employed is Cartesian, providing a straightforward framework for defining spatial coordinates in three dimensions.

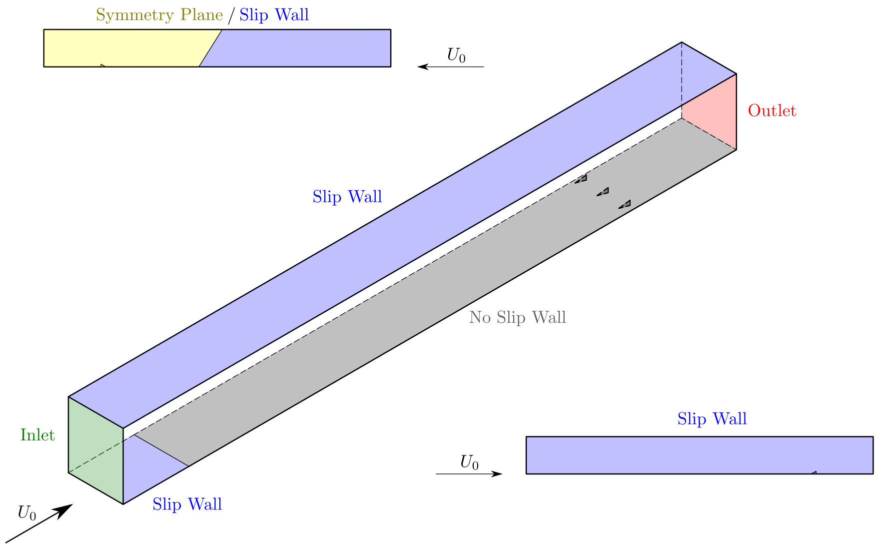

Figure 6.5: CFD computational domain: boundary conditions.

The grid system itself adopts a hexahedral unstructured grid type, offering flexibility in capturing complex geometries while maintaining grid quality and computational efficiency. Consistently applied across all simulations are two refinement areas: one encompassing the ground wall up to a wall-normal distance of 4 cm, and another delineated within a 5 mm radius around the body of each VG (visible in Figure 6.6b). Two grid resolutions are considered, comprising approximately 75 million cells for the single actuator case, and 120 million cells for the full half-array, respectively. This range of cell counts allows for a comprehensive exploration of the flow field, balancing computational resources with the desired level of detail and accuracy in the simulation results.

It is widely acknowledged that employing cell clustering near the wall and maintaining a value of the nearest-to-the-wall step in wall units, Δy^+, around 1.0 is crucial for accurately resolving flow physics within the viscous sublayer. This ensures capturing the behavior of the flow near solid surfaces, contributing to the fidelity of simulation results in regions of significant velocity gradients. In this scenario, achieving this configuration involves situating the initial grid point at a dimensionless distance from the wall of approximately $y \approx 4.5 \times 10^{-5}$ meters. This yields an average value for the first cell of $y^+ \approx 0.5$ along all the domain, demonstrating careful consideration of near-wall mesh refinement to ensure accurate modeling of boundary layer flow phenomena.

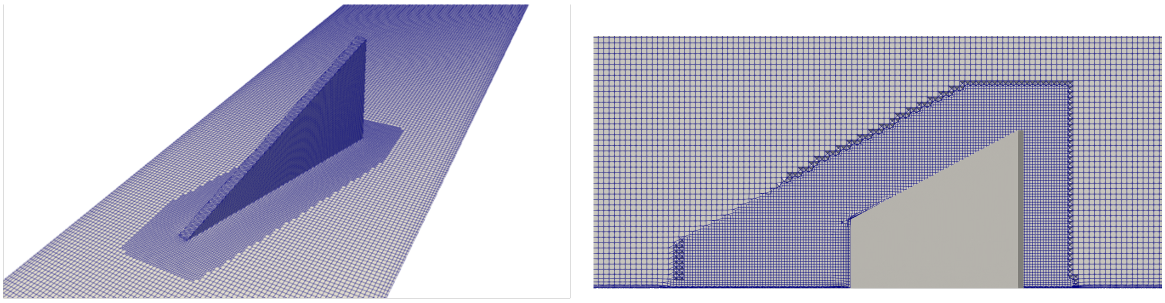

(a) (b)

Figure 6.6: Computational grid of the single vane case: (*a*) Isometric view of the VG and the lower wall; (*b*) Lateral view of proximity refinement around the VG surface.

6.3.5. Turbulent modeling

In the evaluation of the effect of vortex generators on flat plate flow, fully resolved Reynolds-Averaged Navier-Stokes (RANS) simulations are employed. RANS equations, however, pose the problem of their closure, as the Reynolds stress terms need to be modeled. Two primary approaches are prevalent: the Boussinesq hypothesis and Reynolds stress transport equation modeling. Generally, RANS simulations favor the Boussinesq hypothesis due to its computational efficiency, linking Reynolds stress to mean flow velocity gradients via turbulent viscosity (μ_t). Turbulent viscosity can be determined through algebraic relations (zero-equation models) or by solving modeled transport equations for turbulence quantities (one or two-equation models), with the latter being the most common approach.

Table 6.1 summarizes the reference studies along with the associated computational codes and turbulence model combinations used to investigate the effect of vortex generators on flat plate flow. These studies include Fernández-Gámiz et al. (2012), Spalart et al. (2015), Fernández-Gámiz et al. (2016), and Manolesos et al. (2016). Among these, the $k-\omega$ SST model (Menter 1994) is the most frequently employed turbulence model for analyzing VG flows over flat plates. This two-equation model merges the $k-\omega$ model, applicable in the inner boundary layer, with the $k-\varepsilon$ model, used in the free shear flow region.

Despite its prevalence, it is prudent in CFD studies to test various turbulence models to evaluate their suitability for the specific case under investigation. In this study, the Spalart-Allmaras (SA) model, a one-equation model, has been selected as an alternative due to its renowned performance in applications involving wall-bounded flows and boundary layers subjected to adverse pressure gradients. The comparison between these models is presented in the verification section (see Section 6.5).

Table 6.1: Studies and Associated Code-Turbulence Model Combinations

Study	Code	Turbulence model(s)
Fernández-Gámiz et al. (2012)	EllipSys 3D	$k-\omega$ SST
Spalart et al. (2015)	NTS code (compressible)	SA, $k-\omega$ SST, SARC, and $k-\omega$ SST-RC
Fernández-Gámiz et al. (2016)	EllipSys3D	$k-\omega$ SST
Manolesos et al. (2016)	EllipSys3D	$k-\omega$ SST

6.4. Mesh independence study

One critical aspect of ensuring accuracy in the CFD results lies in conducting a mesh independence study. This process involves systematically varying the grid resolution to assess its impact on the numerical solution. Convergence is achieved when further grid refinement produces minimal changes in the solution, indicating independence from the mesh resolution.

This process serves as a fundamental validation step in CFD simulations, ensuring that the results are not overly dependent on the grid resolution. It is important to ensure that the refinement between subsequent meshes is significant enough to discern meaningful differences in the results. Otherwise, excessively similar refinements may yield negligible changes, falsely suggesting mesh independence.

In this project, the mesh sensitivity study has been performed using the forward ramp geometry at a null angle of incidence ($\beta = 0$ deg.) for simplicity. To assess grid independence, the aerodynamic coefficients of the ramp (C_D, C_S, C_L) and the maximum streamwise vorticity ($|\omega_x|_{max}$) downstream of the actuator were monitored and compared across different grid resolutions. Figure 6.7a illustrates the convergence behavior of the aerodynamic coefficients as a function of the grid spacing h, defined as the cubic root of the inverse of the number of cells. Similarly, Figure 6.7b presents the convergence analysis considering the maximum vorticity of the flow downstream of the actuator.

The base size is defined as a function of the refinement level r as:

$$B_r = \frac{B_1}{2^{r-1}} \tag{6.4}$$

where B_1 is the base size of the first refinement level, $B_1 = 0.025$ m.

Both figures demonstrate that as the grid is refined (i.e., the grid spacing h decreases), the curves tend to converge towards a singular value for each quantity of interest. To quantify this convergence, Table 6.2 presents the summary of the different refinement levels of the mesh, along with the corresponding relative error of each magnitude compared to the finest mesh. Refinement level 4.68 serves as the reference case for error calculation, as it represents the upper limit of computational capabilities for a smooth automated workflow given the allocated resources. This consideration is crucial given the necessity of running a large number of simulations for the analysis of skew angle sensitivity, with some simulations potentially requiring full half-array runs, which can increase the cell count significantly.

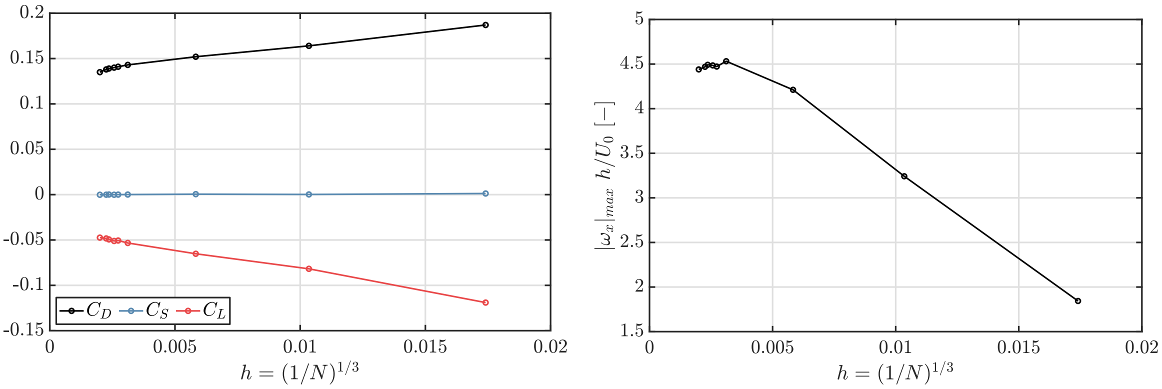

(a) **(b)**

Figure 6.7: Parameter convergence as a function of the grid spacing h: (*a*) Aerodynamic coefficients, C_D, C_S and C_L; (**b**) Maximum absolute vorticity, $|\omega_x|_{max}$.

Ultimately, based on the convergence analysis, the mesh selected for future studies is the one corresponding to refinement level 4.4, using a base size of $2.34 \cdot 10^{-3}$ m and comprising approximately 76 million cells. This choice is informed by the observation that this mesh exhibits errors of 5% or smaller across all quantities of interest, indicating satisfactory convergence. It is noteworthy that one exception, the magnitude C_S, has been excluded from consideration due to its expected null or near-null value at $\beta = 0°$ since even slight variations in the value yield significant errors when compared to the reference.

Table 6.2: Mesh independence study.

Level	Base Size [m]	Cells $\times 10^{-6}$	ΔC_D	ΔC_S	ΔC_L	ΔMax.(ω_x)
1	$2.50 \cdot 10^{-2}$	0.19	37.97%	−886.31%	−150.40%	−58.48%
2	$1.25 \cdot 10^{-2}$	0.90	20.90%	−229.20%	−72.66%	−26.98%
3	$6.25 \cdot 10^{-3}$	5.05	12.50%	−426.05%	−37.65%	−5.15%
4	$3.13 \cdot 10^{-3}$	33.09	5.65%	−155.35%	−12.44%	−2.07%
4.4	$2.34 \cdot 10^{-3}$	75.84	2.67%	−169.35%	−4.27%	−1.17%
4.5	$2.21 \cdot 10^{-3}$	87.23	1.88%	−44.95%	−1.99%	−0.66%
4.68	$1.95 \cdot 10^{-3}$	124.88	–	–	–	–

6.5. Verification

Verification is also a crucial process in ensuring the accuracy and reliability of numerical simulations using CFD. This process confirms the correctness of the programming and computational implementation of the CFD code. This is typically achieved through a series of benchmark tests, where the results of the CFD code are compared against analytical solutions or well-established experimental data for canonical flow problems.

Due to the limited public, trustworthy information regarding the study of vortex generators over a flat plate with the exact flow conditions of this study, in this project, the verification was performed using the Langley Research Center Turbulence Modeling Resource. This resource serves as a benchmark for CFD developers to obtain accurate and up-to-date information on widely-used RANS turbulence models and to verify that these models are implemented correctly.

The specific case chosen for verification is the 2D Zero Pressure Gradient Flat Plate Verification Case. This case involves a turbulent flat plate flow at a Mach number (M) of 0.2, with a Reynolds number of $5 \cdot 10^6$ based on a unit length. The body reference length is 2 units, and the solid wall of the grid extends from $x = 0$ to $x = 2$. It is important to note that although the flow is essentially incompressible at $M = 0.2$, this is a compressible flow verification case. Therefore, running this case with an incompressible code, as in this study, might yield very similar but not necessarily identical results as the grid is refined (Rumsey (2024)).

A schematic of the studied geometry along with the boundary conditions is presented in Figure 6.8. This reference case serves as a benchmark for verifying the correctness of the CFD code implementation before applying it to study vortex generators over a flat plate under similar flow conditions.

Figure 6.9a and Figure 6.9b display the convergence results for the drag coefficient (C_D) and the skin friction coefficient (C_f) measured at $x = 0.97$ m from the leading edge, respectively. These plots compare the results obtained from NASA's CFL3D and FUN3D codes with the OpenFOAM (OF) implementation used in this study. Additionally, two different turbulence models, namely $k - \omega$ SST and Spalart-Allmaras, are compared.

Overall, both graphs illustrate consistent results. The OpenFOAM implementation of the $k - \omega$ SST model slightly underestimates both of the magnitudes but is the closest to the converged solution achieved by NASA. Conversely, the results from SA tend to over-predict the given values, with a slightly larger error. To aid in quantifying the error, 5% error bars are added to both OpenFOAM results for better clarity.

For a comprehensive understanding of the skin friction coefficient evolution, the results are

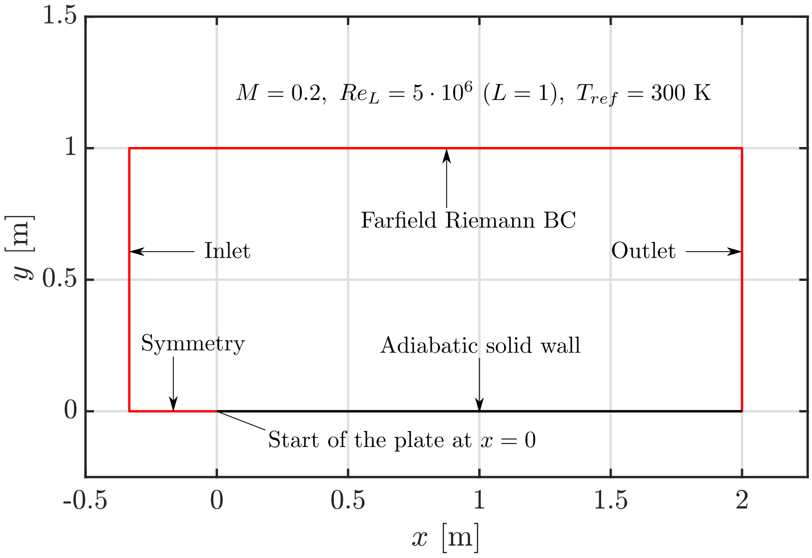

Figure 6.8: 2D Zero Pressure Gradient Flat Plate Verification Case: Boundary conditions.

calculated for the entire length of the flat plate in the streamwise direction and presented in Figure 6.10. While all NASA codes exhibit excellent agreement, the OpenFOAM results align with the findings of the previous set. The $k - \omega$ SST implementation tends to slightly underestimate the friction coefficient, while the SA implementation tends to overestimate it. This bias appears to be consistent all along the domain, hence it is a possibility that the results show some kind of sensitivity to the near-wall mesh rather than the turbulent model itself.

Lastly, Figure 6.11 compares the theoretical turbulent boundary layer profile, including linear and log-law regions, with the results obtained from NASA's CFL3D code and the OpenFOAM implementation of both $k - \omega$ SST and SA models. The SA model demonstrates excellent agreement with both theory and NASA's results. Conversely, the $k - \omega$ SST model slightly deviates, particularly in overestimating the wall-normal velocity (u^+) across the entire range of wall units (y^+). This discrepancy may stem from the model's tendency to underpredict the skin friction of the plate.

Given the focus of this numerical study on quantifying aerodynamic coefficients and skin friction, and considering the $k - \omega$ SST model's closer alignment with the verification results from Rumsey (2024), despite the boundary layer shape error, this model will be utilized to compute the remaining results in this report.

Given the extensive use of the $k - \omega$ SST model in similar research, along with the focus of this numerical study on quantifying aerodynamic coefficients and skin friction, and considering its closer alignment with the verification results from Rumsey (2024), despite the observed boundary layer shape error, the $k - \omega$ SST model will be employed for the remainder of this report.

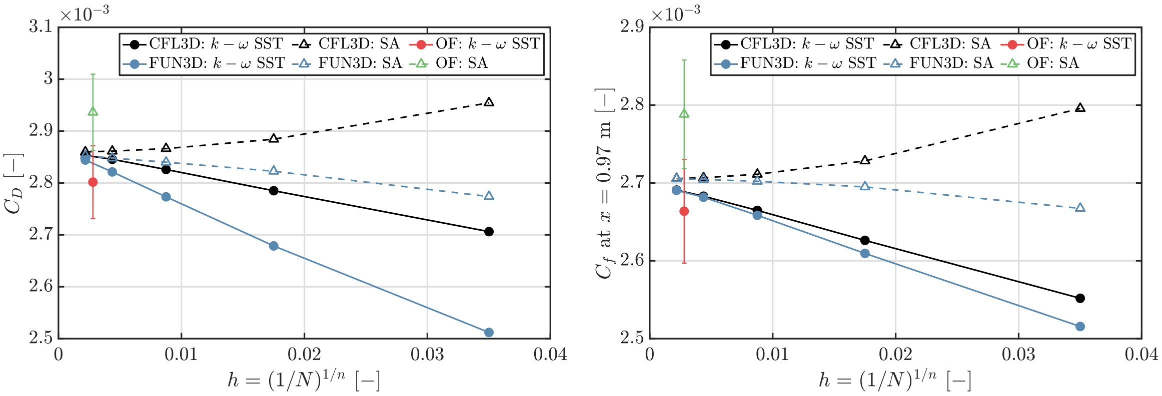

(a) **(b)**

Figure 6.9: Convergence with grid size of: (*a*) Drag coefficient (C_D); (*b*) Wall skin friction coefficient (C_f) at $x = 0.97$ m. X-axis is plotting $(1/N)^{1/n}$, which is proportional to grid spacing (h), where $n = 2$ for the 2D benchmark tests, and $n = 3$ for the 3D OF tests. $h = 0$ represents an infinitely fine grid. 5% error bars are plotted for visual help.

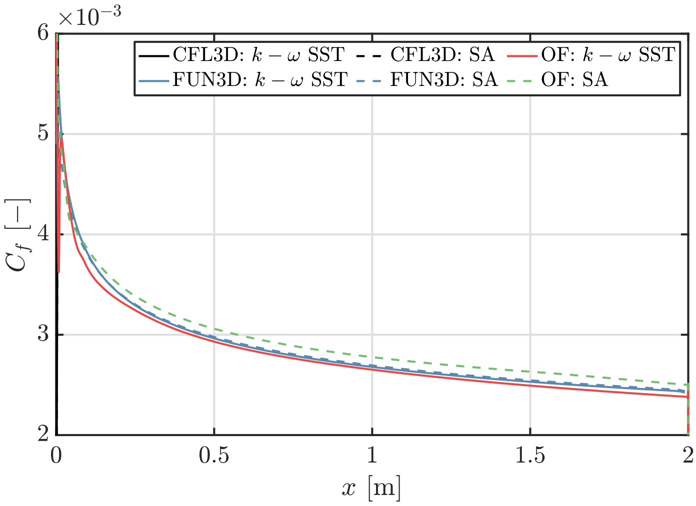

Figure 6.10: Wall skin friction coefficient (C_f) along the flat plate length.

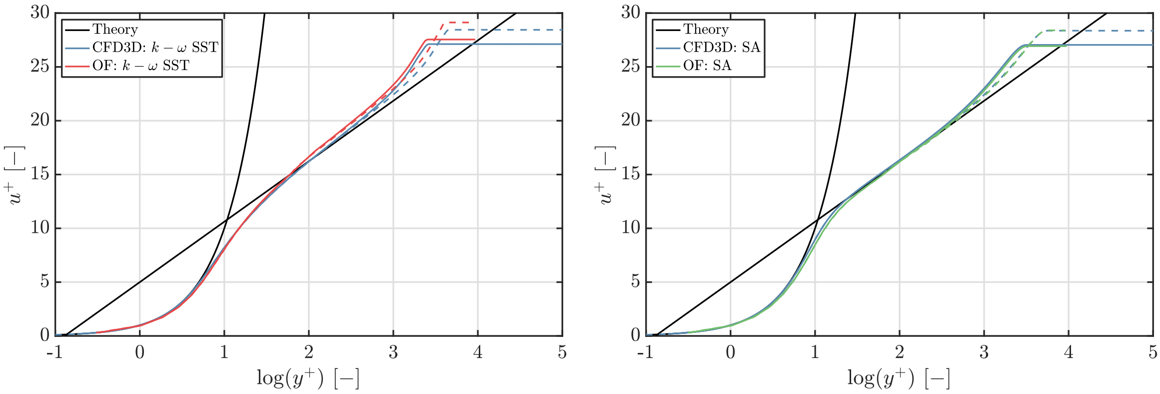

(a) **(b)**

Figure 6.11: Nondimensional boundary layer velocity profile: (*a*) $k-\omega$ SST model; (*b*) SA model. Law-of-the-wall theory with $\kappa = 0.41$ and $B = 5.0$. $x = 0.970$ m (——); $x = 1.903$ m (- - -).

7

Experimental methodology

This methodology chapter is structured into four key sections to comprehensively outline the approach and procedures utilized in the experimental investigations. Beginning with the description of the test section and separation ramp, Section 7.1 provides insights into the physical setup and configuration employed for the experiments. Subsequently, Section 7.2 elaborates on the actuators utilized in the experimental setup, detailing their specifications and operational principles. Following this, Section 7.3 delves into the methodology of Particle Image Velocimetry (PIV), encompassing its working principle, setup, image recording planes, and image processing techniques. Finally, Section 7.4 presents the test matrix utilized in the experiments, outlining the various configurations and parameters investigated. Together, these sections establish a robust methodology for the experimental investigation of aerodynamic phenomena, providing a foundation for the analysis presented in this report.

7.1. Test section and separation ramp

7.1.1. Test section

The experimental investigation was conducted within the W-tunnel facility at the High Speed Laboratory of Delft University of Technology, known for its application in low subsonic aerodynamic testing. This open-circuit wind tunnel, driven by a centrifugal fan, offers versatility with various contractions and test sections tailored to specific research needs. For this study, a 60×60 cm contraction was installed to accommodate a maximum velocity of 15 m/s at the exit of this contraction.

The chosen test section, downstream of the contraction, aligns with the turbulent boundary layer set-up developed by Dacome and Baars (2023), depicted in Figure 7.1. This configuration comprises two modular 1.8 meter test sections, designed to induce a high Reynolds number boundary layer. Although both sections were available, only the initial segment was utilized in this study.

The advantage of this setup lies in the adaptability of its components. The lower boundary features flat panels that are interchangeable, while the ceiling comprises flexible 4 mm polycarbonate panels mounted on movable spanwise beams. Adjusting the positions of these beams allows for manipulation of the streamwise ceiling curvature, regulating the pressure gradient along the tunnel. For this set of experiments, the ceiling height was adjusted specifically aiming to induce the desired adverse pressure gradient leading to boundary layer separation in the ramp. This tailored adjustment facilitated the acquisition of the necessary boundary layer characteristics essential to meet the study's requirements. Positioned above the lower contraction rim is a knife edge, along with a deflector panel, to adjust flow direction adjustment and mitigate separation effects.

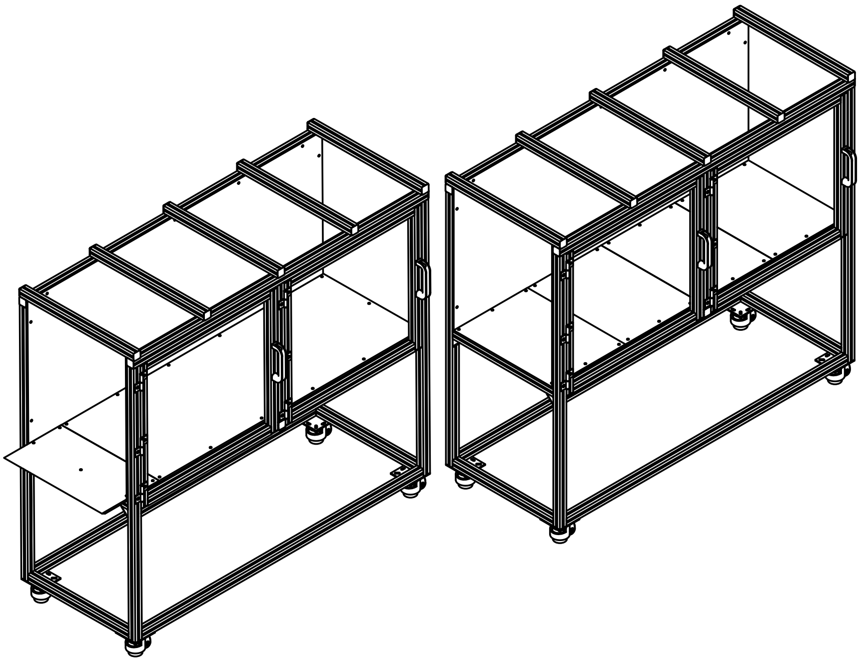

Figure 7.1: Modular turbulent boundary layer test sections developed for use in the W-tunnel by Dacome and Baars (2023).

7.1.2. Separation ramp

Flow separation on the lower wall was induced by incorporating a smoothly curved backward-facing ramp, a commonly used geometric configuration for studying pressure-induced separation phenomena.

The ramp profile used in this study, depicted in Figure 7.2, features a modular design consisting of four distinct parts. The upstream-most section is a 10 mm thick flat plate that houses a slot for the actuators. This is followed by a 4 mm thick curved plate serving as the curved region. Another 10 mm thick flat plate interfaces with an aluminum curved block, which connects to the remainder of the test section.

The modular nature of this ramp offers adaptability. Modifications from the previous setup designed by Budanko (2023) are required only for the upstream-most plate to accommodate the specific requirements of the present project.

The fundamental concept underlying this ramp design is to induce separation through a pressure gradient on a curved surface, as defined by Deck (2012) in his classification of separating flows. According to this concept, the ratio of L/H (where L is the length and H is the height of the ramp) exerts the most significant influence on the adverse pressure gradient, thereby affecting the occurrence and extent of separation. To maintain consistency with similar flow control studies, as summarized in the work of Simmons (2020) and replicated in Table 7.1, the L/H ratio has been maintained within the range of 3 to 5. Moreover, the length-to-height aspect ratio of this ramp design is $L/H = 3.9$.

Furthermore, achieving a near-two-dimensional flow scenario is also a common objective in literature studies that feature similar separation patterns, since this characteristic significantly simplifies flow control analyses. Generally, if $L/W \ll 1$, the flow can be assumed to be relatively uniform in the spanwise direction, with end effects primarily located near the lateral wall regions. However, for smooth-body backward-facing ramps, complete two-dimensionality is often challenging due to technical constraints of the wind tunnel sections, resulting in a significant region of three-dimensionality along the ramp span. In this study, the L/W ratio (where W is the width of the test section) is $L/W = 0.52$, indicating a departure from ideal two-dimensionality. This deviation is due to the fixed constraints of the test section width, requiring compromises to maintain crucial parameters such as boundary layer thickness.

The δ/R ratio (where δ is the boundary layer thickness and R is the curvature radius of the ramp) is another critical parameter influencing flow conditions. Maintaining a low δ/R ratio is essential to ensure that separation primarily arises from adverse pressure gradients rather than geometric curvature effects. A value of $\delta/R = 0.075$ in this study aligns with literature recommendations from Simpson (1996), indicating that separation due to geometry curvature starts occurring around $\delta/R \approx 0.1 - 0.15$, thus ensuring the desired separation conditions.

Notably, the study's constraints stem primarily from the necessity to maintain a boundary layer thickness of approximately 3 cm to enable the testing of vortex generators comparable in height to the boundary layer thickness. To accommodate this requirement, a special boundary layer plate and arrangement of the wind tunnel section were designed and manufactured.

Table 7.1: Curved backward facing ramp design parameters for the present and other relevant separation control studies.

Ramp Geometry	$L/W/H$	δ/H	δ/R	Profile
Simmons et al. (2022)	$4.5/4.6/1$	0.08	–	5th order polynomial
Koklu (2018)	$5.3/5.0/1$	0.25	–	Stratford
Schatzman and Thomas (2017)	$3.0/3.6/1$	0.21	0.05	Flat incline with fillets
Debien et al. (2015)	$4.7/20.0/1$	0.22	–	5th order polynomial
Gardarin and Jacquin (2009)	$2.6/1.4/1$	0.10	–	–
Lin (1992)	$3.3/18.7/1$	0.86	0.16	Flat incline with fillets
Present	$3.9/7.5/1$	0.38	0.075	Flat incline with fillets

7.1.3. Boundary layer development plate

In response to the necessity of maintaining a boundary layer thickness of $\delta \sim 2.5$ cm, to enable the testing of VGs comparable in height, and considering the operational limitations of the wind tunnel, which had already reached its maximum RPM capabilities, a strategic approach was designed to tailor the boundary layer development length to the experimental requirements. Since the undisturbed flow's boundary layer exceeded the desired thickness (according to previous studies in the same facility), the chosen strategy involved generating

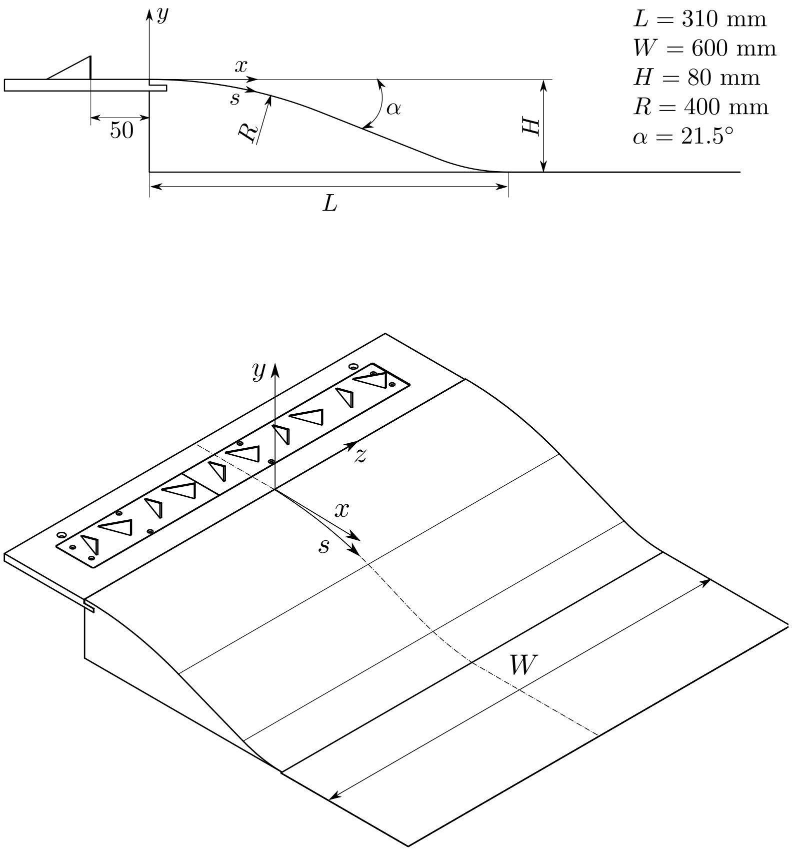

Figure 7.2: Curved backward facing ramp schematic with coordinate systems and VG actuators.

a new boundary layer by introducing a dedicated boundary layer development plate to intersect the incoming flow, thus initiating the development of a fresh boundary layer.

To determine the precise development length necessary to achieve the desired boundary layer thickness, a 2D inviscid flow solution for the test section was computed. The method involved using the characteristics of the test section, in particular the configuration of the ceiling walls, from the study presented in Budanko (2023). Using this information, the distribution of height along the streamwise direction was calculated. Subsequently, the mass conservation equation was applied to derive the velocity gradient, which, in turn, served as input for a MATLAB code adapted from the supplementary materials of Monty et al. (2016), assuming null equivalent sand roughness, to compute the velocity profile under APG conditions. By iteratively estimating the boundary layer thickness required to reach specific streamwise positions, the development length was optimized to achieve the desired boundary layer thickness. The workflow of the iterative solver, delineating the iterative process for determining the boundary layer development length, is depicted in Figure 7.3.

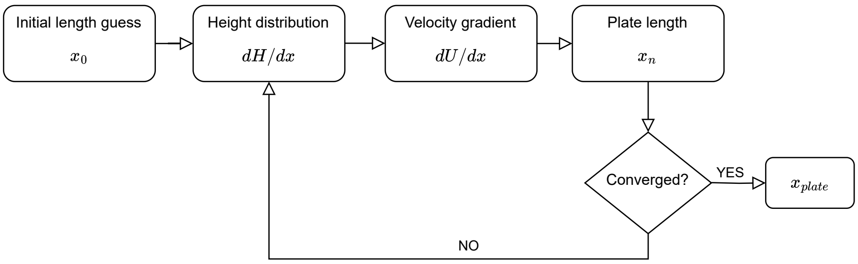

Figure 7.3: Iterative workflow to determine the length of the boundary layer development plate.

Following the determination of the boundary layer plate length, the upstream development section comprises a flat plate measuring 0.7 meters in length, purposefully designed for the experimental setup. Illustrated in Figure 7.4a, this plate incorporates a leading edge characterized by a superelliptic profile, strategically engineered to mitigate boundary layer separation and enhance flow stability.

To minimize flow blockage beneath the flat plate, the floor panels were removed, ensuring unimpeded airflow and preventing flow separation near the leading edge area. To verify that the boundary layer development plate did not trigger separation at its leading edge, preliminary tests were conducted using wool tufts, as can be appreciated in Figure 7.4b.

Additionally, the plate features multiple slots strategically positioned to accommodate actuators as required for the experimental study. To prevent interference with the flow when actuators are not in use, polycarbonate lids were fabricated to cover these slots effectively, maintaining the integrity of the airflow and experimental conditions.

The tunnel geometry, incorporating the evaluated ceiling profile, is illustrated in Figure 7.5. Initial experimentation involving a flat tunnel ceiling revealed a minimal separation region. In response, adjustments were made to the ceiling configuration as depicted in the figure. This modified configuration augmented the adverse pressure gradient acting on the flow, consequently enlarging the separation bubble. To verify that the adverse pressure gradient did not trigger separation at the test section's ceiling, another set of preliminary tests were conducted using wool tufts located at the ceiling's wall, in particular near the areas of maximum curvature.

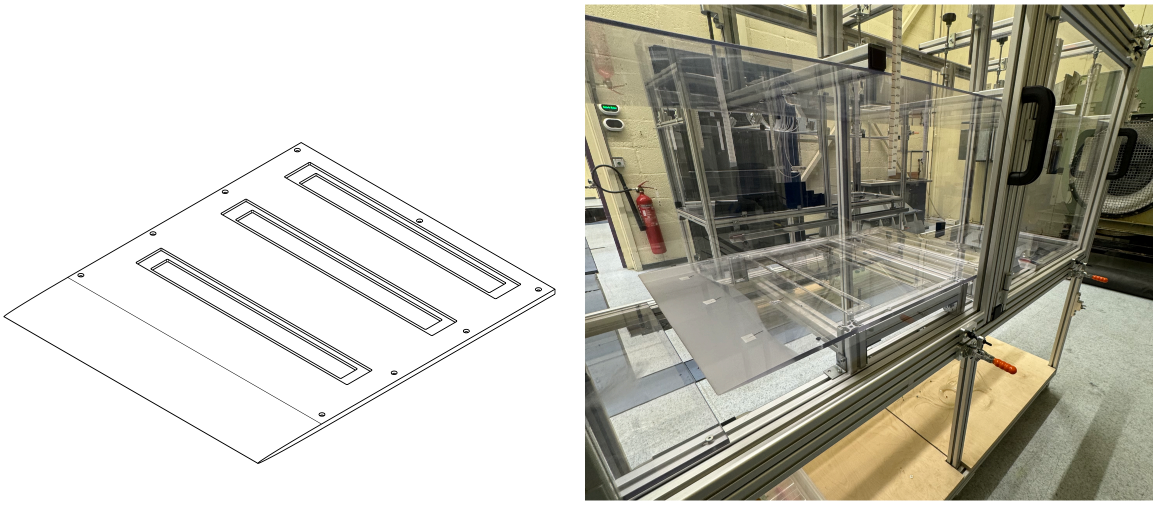

(a)

(b)

Figure 7.4: Boundary layer development plate. Illustrations of: (*a*) 3D sketch; (*b*) Implementation in the test section (with wool tufts attached near the leading edge to test flow separation).

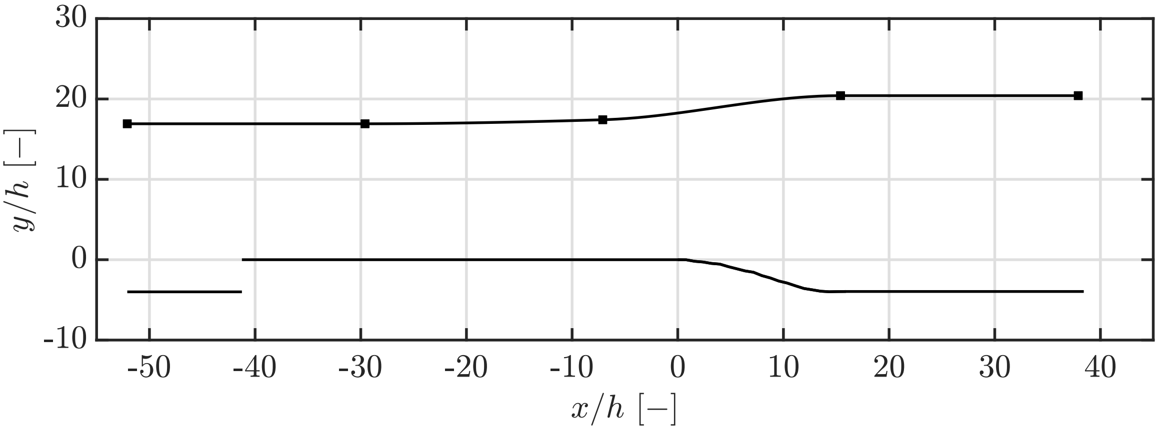

Figure 7.5: Profile of the wind tunnel test section including the ceiling. Ceiling beams represented by ■.

7.2. Actuators

The use of conventional vortex generators with heights comparable to the boundary layer thickness ($h/\delta = \mathcal{O}(1)$) has been a common practice in aerodynamic applications to prevent localized flow separation. However, this conventional approach often comes with the drawback of increased residual drag. Recent research efforts have thus shifted towards addressing this challenge by exploring alternative VG designs with reduced heights relative to the boundary layer, known as sub-boundary layer vortex generators (SBVGs). These SBVGs, characterized by a relative height $h/\delta < 1$, have shown promise, particularly in scenarios where the separation point remains relatively fixed and extensive downstream coverage is not required. However, when compared to conventional VGs, they require adjustments in parameters like the vane aspect ratio (L/h), the inter-separation (D/h), and the skew angle (β) to ensure the generation of strong enough streamwise vortices for effective flow control.

In the context of vortex generators selectively deployed on demand, concerns regarding potential increases in residual drag are mitigated, hence the focus shifts towards maximizing actuator performance when deployed. As such, the vortex generator configurations investigated in this project adopt the features of conventional VGs, with heights on the order of the boundary layer thickness.

Specifically, the actuators employed in this study comprise four configurations of VG arrays, each measuring 49.7 cm in width and 5.9 cm in length and containing a total of five individual actuators (comprising pairs of vanes, single vanes, or ramps). These actuators have been fabricated using 3D-printed materials. To streamline the manufacturing process, each array has been divided into two pieces, as illustrated in Figure 7.6. An advantageous characteristic of the ramps at a null skew angle ($\beta = 0$ degrees) is their capability to be rotated 180 degrees, thereby enabling their use as forward ramp actuators. This versatility serves as a primary rationale for selecting this particular configuration.

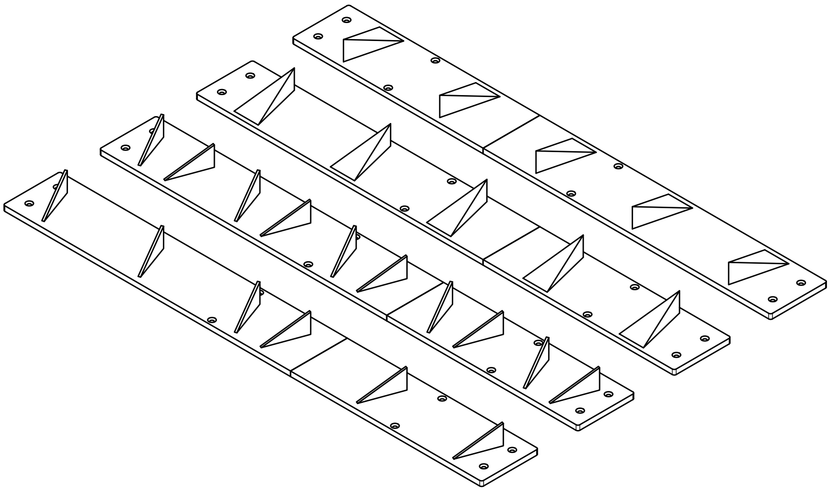

Figure 7.6: Sketch of the VG arrays tested in the experimental study. From left to right: Co-rotating vanes (CoR), Counter-rotating vanes (CtR), Forward ramp (FR), Backward ramp (BR).

As a summary, Table 7.2 presents the main parameters describing the geometry of the actuators test in the experimental study:

Table 7.2: Geometry parameters of the vortex generators under study.

Configuration	VGs	h [m]	L/h	d/h	D/h	β [deg.]
CtR	Triangular vanes	0.02	2	2.5	5	20
CoR	Triangular vanes	0.02	2	–	5	20
BR	Backward wedge	0.02	2.5	–	5	0
FR	Forward wedge	0.02	2.5	–	5	0

7.3. Particle Image Velocimetry (PIV)

In recent years, PIV has become an essential tool in fluid dynamics research for accurately measuring fluid flow velocities. This introduction provides a concise overview of the working principles behind PIV and outlines its specific application within this research framework.

7.3.1. Working principle

PIV relies on the principle of discerning correlations in the spatial distribution of suspended particles within a fluid across consecutive frames to infer its velocity field. The operation of PIV can be studied as a sequence of steps:

- Flow seeding.
- Laser illumination.
- Image capture.
- Image processing.
- Velocity computation.

Seeding the flow is the initial step in a PIV experiment. PIV is an indirect velocity measurement technique, hence it calculates the velocity of a fluid element by measuring the velocity of tracer particles within the flow. Consequently, this involves introducing small particles into the fluid under study. These particles are ideally very small, neutrally buoyant, and capable of accurately tracing the flow.

Following the flow seeding, a laser is used to create either a flat sheet (for planar PIV) or a three-dimensional volume (for tomographic PIV) of light, which is able to capture a snapshot of the fluid's condition at a specific time instant. Particles in the illuminated area scatter photons, creating an image that shows the particles' locations. Unfortunately, small particles do not scatter much light, so a powerful pulsed laser is needed to light up the flow field.

Image capture plays another crucial role in the process. One (or multiple) cameras, positioned at a specific angle, capture the scattered light, thereby recording the positions of the particles within a designated cross-section of the flow. Following the initial image capture, a brief time delay Δt is introduced. This delay allows the fluid to undergo slight evolution. Subsequently, a second image is captured to document the new positions of the particles. This time delay ensures that changes in fluid motion are accurately recorded. The visual data is subsequently digitized into images.

Image processing is the stage where recorded images undergo processing. Each image is dissected into small interrogation windows, and the displacement of particles from the first image to the second is computed within these regions. After this, the displacement data is used to calculate the velocity vectors of the particles. By considering the time delay between the images and the spatial arrangement of the interrogation regions, the instantaneous velocity of the fluid at those specific points can be determined. This step is fundamental in providing a spatially resolved velocity vector field, a key outcome of PIV experiments. For reference, the typical setup for a planar PIV experiment is depicted in Figure 7.7.

PIV offers some remarkable advantages that make it stand out from other state-of-the-art flow measurement techniques. Firstly, it is a non-intrusive method, unlike traditional techniques that use probes such as pressure tubes or hot wires. This allows PIV to excel even in high-speed flows with shocks and near-wall boundary layers, preserving the undisturbed nature of the fluid. Secondly, it is a whole-field technique, meaning it can capture images and obtain data from large parts of the flow field, unlike other techniques which only capture data from a single point. This leads to a high spatial resolution, providing a comprehensive view of complex flow phenomena. Lastly, PIV is characterized by its quantitative precision,

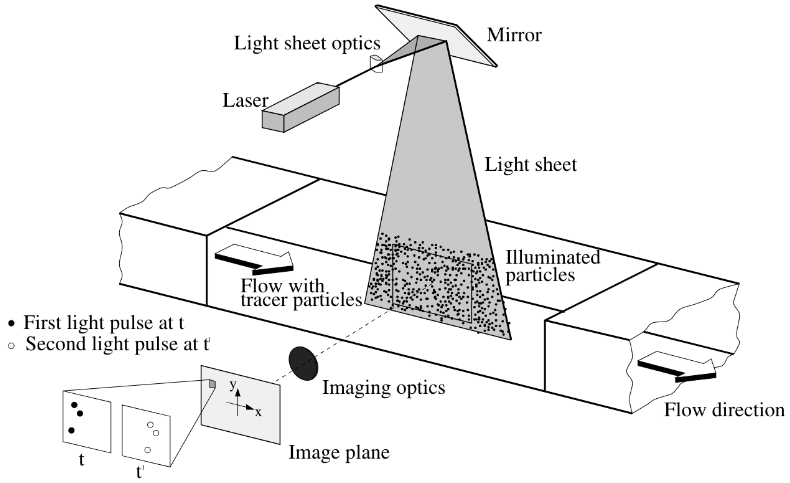

Figure 7.7: Experimental setup for planar PIV in a wind tunnel. [From Raffel et al. (2007)]

providing not only visual qualitative data but also accurate and reliable velocity measurements.

While offering notable advantages, PIV also presents certain challenges that deserve consideration. Firstly, as noted previously, PIV relies on indirect velocity measurements, meaning it assesses fluid velocity by tracking tracer particles within the flow, which are usually introduced before the experiment. For each experiment, it must be ensured that the tracer particles will accurately track the motion of the fluid elements. While smaller particles will track the flow more effectively, they have a lower light scattering efficiency, so a compromise must be found. Secondly, PIV requires optical access for the laser to illuminate the flow field and the cameras to capture images. According to this, a transparent viewing area is needed, which may not always be the case in certain experimental setups, limiting the applicability of the technique. Lastly, PIV requires a complex setup, implementing PIV effectively demands meticulous calibration, precise alignment of optical components, and post-processing of captured images. Fortunately, advancements in PIV technology and software have mitigated some of these complexities, making the technique more accessible over time (Raffel et al. 2007).

Table 7.3 summarizes the main points made regarding the advantages and disadvantages of this flow measurement technique.

Advantages	Disadvantages
Non-intrusive measurement	Indirect measurement
High spatial resolution	Needs optical access
Whole field technique	Complex setup
Quantitative	

Table 7.3: Advantages and disadvantages of PIV as a flow measurement technique.

7.3.2. Planar PIV

In the previous section, the basic working principles of PIV for a planar 2- or 3-component measurement were presented, without delving into extensive specifics. Nevertheless, these fundamental principles serve as the foundation for the more sophisticated methods currently in use in both, industry and academia. This section presents a more detailed view of planar PIV (2-Dimensional, 2-Component), which is the technique that will be used in the experimental tests within this project.

Planar PIV relies on the principle of measuring the displacement of suspended particles within a fluid to infer the in-plane velocity field, i.e. $u(x, y)$ and $v(x, y)$, in a 2D domain. According to this, the main components of a test setup are the tracer particles, the illumination, and the imaging. Both the tracer particles and the illumination, share many common treats in both planar and stereoscopic PIV. The imaging part, however, differs notably. This component will be examined in detail here.

When setting up an experiment, several critical parameters come into play on the imaging side. These parameters encompass the magnification factor (M), focal length (f), aperture (D), and the f-stop ($f_{\#}$), which relates the focal length to the aperture. A comprehensive understanding of these factors is key to achieving the desired outcomes.

The magnification factor, M, is the ratio between the sensor and the object size and represents how the object size is scaled in the final image.

$$M = \frac{\text{sensor size}}{\text{object size}} \tag{7.1}$$

Both the focal length and aperture are lens-related characteristics, and their relationship is defined by the f-stop, $f_{\#} = f/D$. The f-stop dictates the amount of light entering the lens and influences the depth of field. A lower f-stop indicates a larger aperture, allowing more light and a shallower depth of field, often resulting in background blur. Conversely, a higher f-stop reduces the aperture size, permitting less light and expanding the depth of field, ensuring more elements remain in focus.

There are two important considerations when configuring these parameters. First, the depth of field should be at least as thick as the laser sheet's dimensions. Additionally, it is imperative that particle images are of sufficient size. The diameter of particle images in pixels can be calculated using the following equation:

$$d_{\tau} = \sqrt{(Md_p)^2 + [2.44\lambda(1+M)f_{\#}]^2} \tag{7.2}$$

This formula accounts for both the physical size (first term) of the particles and the diffraction diameter (second term). In the case of a digital camera based on a CCD chip, the camera sensor is an array of pixels sensible to light. If the particle image diameter is too small ($d_{\tau} < 1$), peak-locking occurs, which means that the subpixel displacement cannot be distinguished. Contrarily, if the particle image diameter is too large, it is likely that many particle images overlap. For optimal accuracy, $d_{\tau} \approx 2 - 3$ px, according to Tropea et al. (2007).

To assess tracer particle movement in images and determine a velocity field, a systematic approach is adopted, the so-called image windowing method. This approach involves breaking down the images into smaller areas referred to as interrogation windows, each containing a minimum of 10 tracer particles, as suggested by Tropea et al. (2007).

Corresponding windows in two successive frames are compared through a statistical analysis technique called cross-correlation. The cross-correlation value (ϕ) evaluates the level of particle matching between the two interrogation windows, hence a correlation map can be generated. Among the correlation peaks, the one with the highest value is selected, as it represents the mean motion of the tracer particles. Peaks other than the highest are disregarded since they typically arise from noise or correlations between non-matching particles.

$$\phi(m,n) = \frac{\sum_{i,j=1}^{K,L} I(i,j) \cdot I'(i+m, j+n)}{\sigma(I) \cdot \sigma(I')} \tag{7.3}$$

The samples I and I' are taken from the images, with I' being larger than the template I. Essentially, the template I is shifted around within the sample I' without going beyond its boundaries. For each shift (x, y) chosen, the sum of the products of all overlapping pixel intensities produces one cross-correlation value. By performing this operation for a range of shifts $(-M \leq x \leq +M, -N \leq y \leq +N)$, a correlation plane of size $(2M+1) \times (2N+1)$ is created (Raffel et al. 2007).

In order to improve measurement accuracy, it is important to keep the interrogation windows as small as possible. However, if these are too small, particles may move in and out of the window between pulses, resulting in non-real peaks in the cross-correlation map and a decrease in signal-to-noise ratio. Generally, the maximum in-plane displacement of the particles should not exceed one-quarter of the interrogation window size. To tackle this limitation, a multi-pass processing approach is frequently used. In successive passes, the pair of interrogation windows is shifted by the displacement calculated in the previous pass before computing the correlation map. This allows for the use of smaller windows, which can also be altered to adjust to changes in particle position and further enhance measurement precision.

Once the pixel displacement is calculated, it must be converted to physical space, considering camera and lens parameters, including magnification and potential image distortion. The exact transformation is determined through calibration, which involves imaging a calibration target with known dimensions, such as millimeter paper on a flat plate. Once the displacements are mapped to physical space, determining the velocity field becomes straightforward, given the known time separation between the two image exposures:

$$u(x,y) = \frac{\Delta x}{M \Delta t} \tag{7.4}$$

$$v(x,y) = \frac{\Delta y}{M \Delta t} \tag{7.5}$$

7.3.3. Recording planes

With the velocity field established through the described PIV methodology, it is crucial to strategically select recording planes which capture effectively the flow structures and their interactions with the vortex generators. To facilitate the acquisition of results, a total of four recording planes were strategically selected for analysis:

- Three planes in wall-normal streamwise direction ($X - Y$):
  - Center plane: $z/h = 0.0$.
  - Middle plane: $z/h = 1.35$.
  - Off-center plane: $z/h = 2.5$.

- One plane in wall-normal spanwise direction ($Y - Z$):
    - Crossflow: $x/h = 0.0$.

As depicted in Figure 7.8, each of these recording planes serves a distinct purpose in capturing relevant flow characteristics and phenomena. The wall-normal streamwise planes cover the entire length of the ramp, allowing the study of boundary layer velocity profiles, the identification of detachment and reattachment points, and the characterization of separation bubble size and shape. While a single streamwise plane may suffice for studying a purely two-dimensional flow field, the three-dimensional nature of the uncontrolled and especially the controlled flows in this test section, requires multiple streamwise planes along the span to better characterize the flow field. These planes facilitate the observation and analysis of the spanwise evolution of critical variables regarding the separation bubble.

In addition to the wall-normal streamwise planes, crossflow planes provide essential insights into spanwise flow variations. One plane positioned close to the ramp curvature inception captures the flow field before the separation region, allowing the characterization of the adverse pressure gradient effect. This plane not only enables the observation of the flow field generated by the VG actuators immediately downstream but also facilitates the study of phenomena such as vortex decay, translation, merging, and other dynamic interactions. By comparing the results in this same plane while varying the streamwise position of the VG actuators, the effects of vortex behavior and decay can be systematically analyzed, offering valuable insights into flow control mechanisms and VG performance.

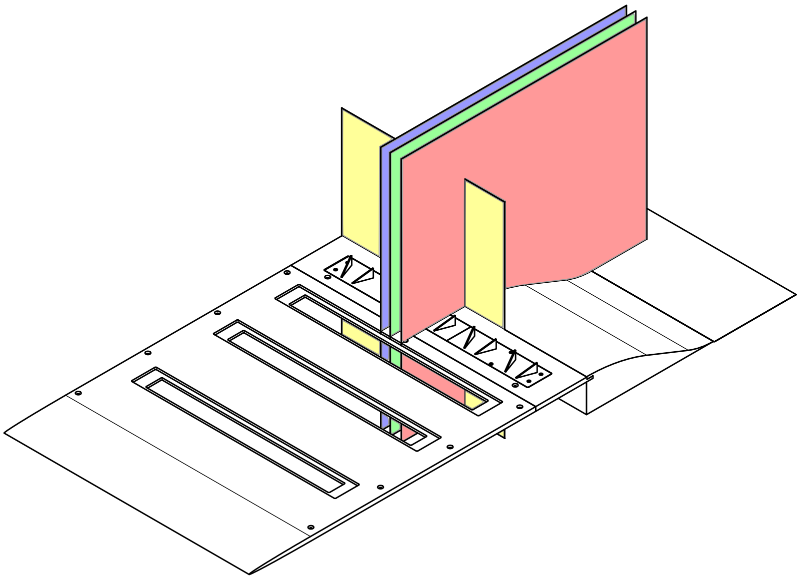

Figure 7.8: Three-dimensional illustration of the PIV recording plane positions in relation to ramp geometry. Center plane in *red*, middle plane in *green*, off-center plane in *blue*, crossflow plane in *yellow*.

7.3.4. Experimental setup

Having identified the recording planes essential for capturing the comprehensive flow field data, the next step is to detail the experimental setup used to acquire these measurements. The experimental setup, depicted in Figure 7.9, facilitated the imaging of the recording planes presented in the Section 7.3.3. To capture the streamwise planes, the laser was positioned downstream of the test section exit, while the two cameras were placed beside the test section, pointing in the $-z$ direction, across the test section's wall. Utilizing two side-by-side cameras expanded the field of view, providing comprehensive coverage along the separation ramp length. For crossflow planes, the laser was positioned perpendicular to the test section's lateral wall, with the laser sheet directed in the $+z$ direction. In this setup, a single downstream camera captured the crossflow planes, resulting in the recording of only two out of the five VG pairs in the crossflow plane.

To maintain high-quality imaging and minimize reflections, black non-reflective tape was applied across the ramp and various surfaces of the test section, including background walls. Additionally, regular cleaning with ethanol ensured clean conditions for camera lenses and all surfaces.

All image acquisition and processing were executed using LaVision's DaVis 8.4.0 PIV software. LaVision sCMOS cameras with 2560×2160 pixel resolution and Nikon 60 mm lenses were employed for both streamwise and crossflow planes. The laser source, a Quantel Evergreen Nd:YAG laser, was configured to generate a laser sheet using an optical arrangement comprising diverging and converging lenses to form the beam waist, followed by a cylindrical lens for expansion into a thin laser sheet. While similar optical setups were used for both planes, varying focal length lenses were chosen due to differences in distance from the laser. The laser sheet thickness, approximately $1 - 2$ mm throughout the camera field of view, ensured optimal illumination and imaging conditions.

The technique utilized to establish the laser sheet thickness for the streamwise planes involves positioning measuring paper at a known angle relative to the incoming laser sheet. By measuring the total thickness of the laser sheet on the angled measuring paper and considering the known angle of incidence, the actual thickness of the laser sheet can be calculated using basic trigonometric relationships. Conversely, for the crossflow planes where the laser sheet was directed through the lateral wall of the test section, a simpler yet effective approach to control the laser sheet is employed. This entails creating a cut-out from non-reflective paper, shaping it to the desired sheet shape and thickness. In this instance, a 2 mm aperture was created, as depicted in Figure 7.9b.

Flow seeding was provided by a SAFEX fog generator in the wind tunnel's fan chamber, utilizing a glycol-water solution to generate particles with $1 - 3$ μm mean diameter, ensuring adequate flow field visualization for accurate data acquisition and analysis.

For camera and processing software calibration, a LaVision single-sided calibration plate was utilized. These white single-sided calibration plates are commonly utilized for calibrating 2D PIV setups. The calibration process involves capturing views of the plate using the different cameras, and identifying manually the reference points. The rest of the marks on the plate are automatically detected, and the information from all detected marks is utilized in the bundle adjustment calibration algorithm. This live calibration procedure also calculates the intrinsic and extrinsic camera parameters.

During PIV acquisitions across all four planes, various parameters were adjusted to optimize image quality and ensure accurate velocity determination. Initially, camera focus and aperture settings were fine-tuned to improve particle visibility and mitigate peak-locking issues. Due to the dim appearance of particles in images caused by the considerable distance between planes and cameras, the aperture was set to $f_{\#} = 5.6$ to increase light capture. Focusing

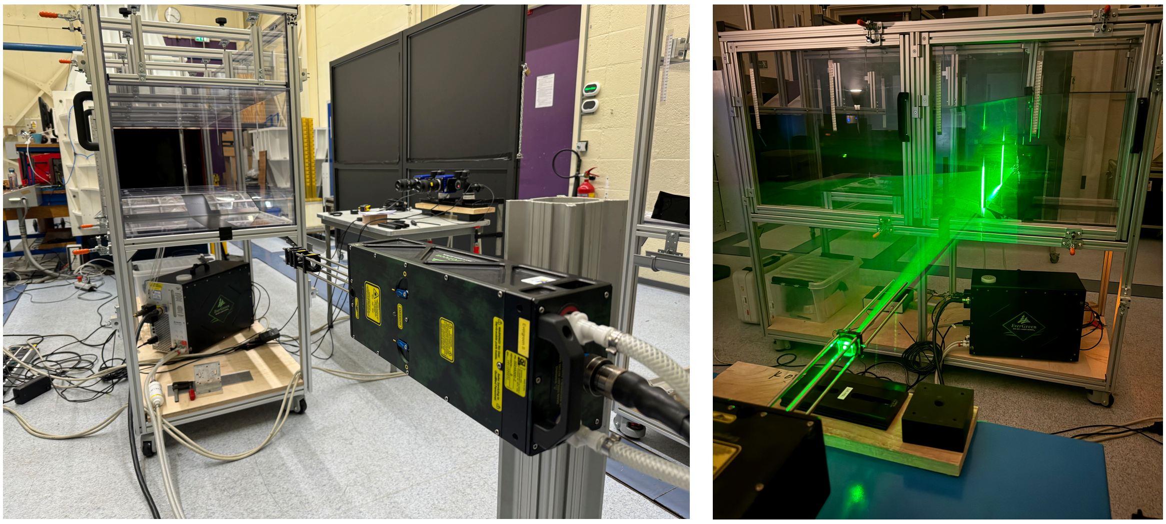
(a) (b)

Figure 7.9: Pictures of camera and laser setups for: (*a*) Streamwise planes; (*b*) Crossflow planes.

the cameras deliberately aimed to achieve imaged particle diameters of around 3 pixels, reducing peak-locking phenomena and facilitating sub-pixel interpolation during processing.

Furthermore, given the high dynamic range of the imaged separating flow, particularly in near-wall regions where velocity approaches zero, a relatively high pulse spacing (dt) was necessary for accurate velocity determination within the streamwise planes. Through empirical tests, a pulse spacing of 100 μs was deemed optimal for these planes, ensuring sufficient temporal resolution while minimizing effects of particle displacement between successive image pairs. On the contrary, for recordings within the crossflow plane, the pulse spacing was reduced to 50 μs. This adjustment was essential to ensure that particles were captured within the plane thickness (which is normal to the main flow direction), thereby facilitating the computation of cross-correlation and the pertinent velocity field. Furthermore, the recording rate remained consistent across all image acquisitions at 15 Hz.

Details of camera settings and field-of-view size for both planes are summarized in Table 7.4, providing a comprehensive overview of the configuration parameters used for PIV acquisitions. These optimized settings were crucial for obtaining high-quality PIV measurements, enabling accurate analysis and interpretation of flow field characteristics.

7.3.5. Image processing

Before conducting the cross-correlation procedure for velocity field determination, the raw images were pre-processed to enhance the signal-to-noise ratio. Initially, the average intensity value of all source images was calculated and used to normalize the measurements. Following this, a time filter was applied to eliminate background noise by subtracting the minimum intensity over a sequence of subsequent snapshots. This filtering process, spanning 11 consecutive images, effectively reduced noise, especially in areas where reflection intensity remained constant over time, such as walls and vortex generators. By applying a suitable high-pass filter, only the low frequencies of the slow-moving reflections were attenuated, eliminating them while preserving the intensities of the particles.

After the pre-processing routines, velocity fields were derived from the processed images using the conventional cross-correlation PIV method, employing a multi-pass approach. The initial passes utilized a window size determined by the recommended practice of adopting a window four times larger than the largest particle displacement, set initially at 64×64 pixels. The final window size was determined empirically to balance precision, noise sensitivity, and computational efficiency, set initially at 32×32 pixels.

For increased precision in critical regions, such as near the wall, in some particular cases, the window size of the final pass was reduced to 8×8 pixels. While this adjustment may slightly compromise the overall accuracy of the results due to increased noise sensitivity, it significantly enhanced the resolution of data points near the wall, facilitating a more detailed characterization of the incoming flow boundary layer, presented in Section 9.3.

Moreover, in an attempt to reduce the effect of the camera alignment with respect to the incoming flow, in the particular case of the crossflow plane recordings, the velocity field of the uncontrolled flow recordings was subtracted from the resulting velocity field for each of the measurements, allowing to exclude biases due to camera positioning.

A 50% overlap was maintained in all passes to ensure adequate spatial resolution. Additionally, the presence of the wall was identified from the raw images using the particle wall reflections. The mask was created based on this data and applied after initial cross-correlation processing.

The processing settings employed during pre-processing and cross-correlation are summarized in Table 7.4, providing a comprehensive overview of the parameters utilized to generate the velocity fields.

Table 7.4: PIV velocity field imaging and processing settings.

Plane	FoV [mm]	$f_\#$	dt [μs]	Initial passes	Final passes
Center	540×245	5.6	100	$1,\ 64 \times 64$ px, 50%	$2,\ 32 \times 32$ px, 50%
Middle	540×245	5.6	100	$1,\ 64 \times 64$ px, 50%	$2,\ 32 \times 32$ px, 50%
Off-center	540×245	5.6	100	$1,\ 64 \times 64$ px, 50%	$2,\ 32 \times 32$ px, 50%
Crossflow	190×160	5.6	50	$1,\ 64 \times 64$ px, 50%	$2,\ 32 \times 32$ px, 50%

7.4. Test matrix

In summary, the experimental study involved testing four distinct vortex generator arrays, each positioned at varying streamwise locations relative to the inception of the ramp curvature. To assess the effects across the spanwise direction of the test section, recordings were conducted at three different wall-normal streamwise planes. Additionally, to provide deeper insights into the streamwise results and quantify the impacts of vortex decay and trajectories, an additional crossflow plane was recorded in the wall-normal spanwise direction.

The configurations of the tested vortex generator arrays and the planes at which measurements were recorded are summarized in Table 7.5, providing a comprehensive overview of the experimental setup and the corresponding data acquisition points.

It is worth noting that, alongside the configurations and planes presented in Table 7.5, an additional uncontrolled flow run was recorded for each of the planes. This recording serves multiple purposes: it provides a baseline against which the effectiveness of the vortex generators can be evaluated, and it offers a source of data that can be utilized to correct for background noise, such as camera alignment issues, thus enhancing the accuracy and reliability of the experimental results.

Table 7.5: All tested VG configurations. The x positions of the VG positions correspond to the distance (upstream) from the inception of the ramp curvature. Center, Middle and Off-Center measure the flow field along the $X - Y$ planes; Crossflow measures along the $Y - Z$ plane.

VG	β [deg.]	$x_{VG}/h = 4.5$	$x_{VG}/h = 10.5$	$x_{VG}/h = 18$	$x_{VG}/h = 28$	Plane
CtR	20	×	×	×	×	Center
		×	×	×	×	Middle
		×	×	×	×	Off-Center
		×		×		Crossflow
CoR	20	×	×	×	×	Center
		×	×	×	×	Middle
		×	×	×	×	Off-Center
		×		×		Crossflow
BR	0	×	×	×	×	Center
						Middle
		×	×	×	×	Off-Center
		×		×		Crossflow
FR	0	×	×	×	×	Center
						Middle
		×	×	×	×	Off-Center
		×		×		Crossflow

Part III

Results and Discussion

8

Skew angle sensitivity

The advantages of CFD studies lie in their ability to investigate the details of particular fluid dynamics phenomena in a controlled environment. In comparison with the experimental tests, this technique enables the simultaneous acquisition of all field quantities, potentially leading to a deeper understanding of the flow. Consequently, CFD serves as a valuable tool for cases where experimental studies are too expensive or complex.

In this project, the objective of the CFD study is to characterize the sensitivity of the various VG designs to the skew angle, β. Because the core emphasis of this numerical investigation centers on the impact of VGs in a flat plate configuration, the attention should shift toward the precise quantification of the associated loads imposed over their geometry, the vortex development, and their influence over the near-wall flow. This computational approach complements the experimental study by facilitating a parametric sweep, which allows for the assessment of both the aerodynamic loads affecting the actuators, as well as the vorticity of the flow in a crossflow plane downstream the actuator.

The three primary actuator concepts were individually tested in isolation over a flat plate with zero pressure gradient. Consistent with typical values of β cited in studies such as Godard and Stanislas (2006) and Ashill et al. (2001), the range of study was set to $\beta \in [15, 25]$ degrees for the vane designs and $\beta \in [0, 10]$ degrees for the ramp designs. Additionally, in anticipation of potential future implementations of deployable VGs actuated using shape memory alloys, three secondary designs were tested: the curved vane, and the hollow ramp (in both forward and backward directions).

8.1. Load coefficients

Given the challenges associated with the manufacturing of a deployable vortex generator actuated using a shape memory alloy, accurately estimating the magnitude of these loads is paramount for this project since they are a significant constraint for future implementations. If the VG is actuated via a hinge mechanism, minimizing the loads that tend to induce stress along the hinge axis is crucial for ensuring the viability of the design. Figure 8.1 presents the nondimensional axial, normal and side loads (C_A, C_N, C_S, respectively) acting on the actuator body as a function of the skew angle according to the CFD simulations. Note that, to make designs comparable, the reference area used to calculate the coefficients is based on h^2, which is the common factor for all the designs.

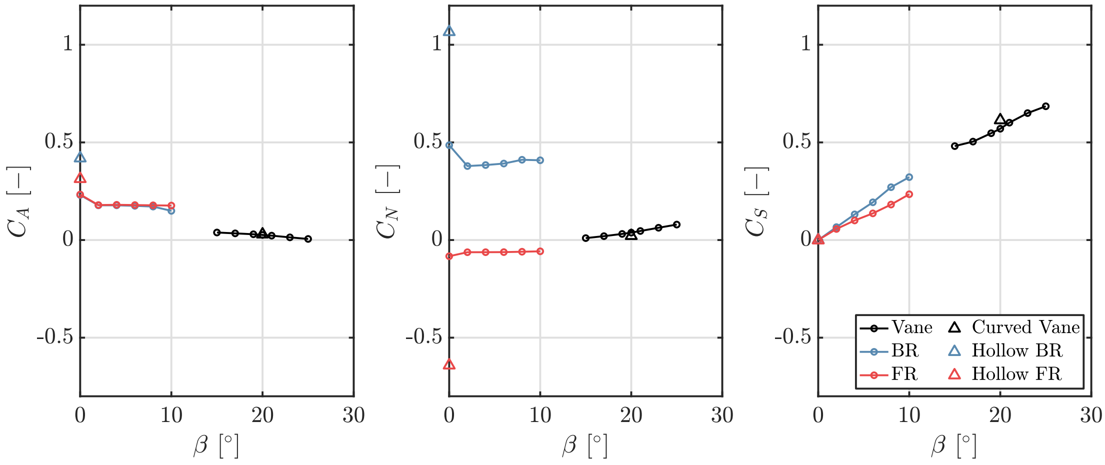

Figure 8.1: Axial (C_A), normal (C_N), and side (C_S) loads exerted on the actuator body in relation to the skew angle (β).

As depicted in Figure 8.1, the axial load on all of the actuator designs exhibits a minimal sensitivity to the skew angle, with nearly identical trends observed for both orientations of ramps. The single vane shows a slightly decreasing trend for increasing values of β. This behavior can be attributed to the low frontal area of the vane designs, and the aerodynamic effect of the lateral walls of the ramp, which effectively cut through the air, mitigating a significant blockage. Overall, these findings are promising for potential deployable systems, since they indicate robustness against axial loads.

Conversely, the normal loads exhibit very different trends among the three designs. The orientation of the ramp significantly influences the resultant load in the normal direction. The backward-facing ramp generates a substantial positive normal load that tends to increase for large angles of incidence, whereas the forward ramp experiences a relatively small and constant wall-normal-negative load. These results are direct effects of the areas of low and high pressure, respectively, created by the ramp actuators near their upper surface.

To illustrate this, Figure 8.2a and Figure 8.2b depict a slice along the symmetry plane of the forward and backward ramp geometries, respectively, at $\beta = 0$ degrees. As it can be appreciated, the results of the backward ramp clearly show a point of stagnation near the geometry leading edge, as well as a big area of low pressure over most of the upper surface of the actuator. Conversely, the forward ramp generates a minimal perturbation on the pressure field apart from a relatively high-pressure area near the geometry leading edge, and a low-pressure area near the trailing edge.

The vane design yields an intermediate result between these cases, showing a small positive normal load, which tends to increase linearly with the angle of incidence. It is important to note that the normal load in particular may be critical for potential implementations of deployable VGs using the ramp concept specifically, as it could induce hyperextension of the hinge, leading to additional fatigue on the joint. Given the current shape memory alloy technology, minimizing the number of cycles and hyperextensions of these joints is crucial for extending the lifespan of such devices.

Focusing on the side force coefficient, this load exhibits the most significant sensitivity to the

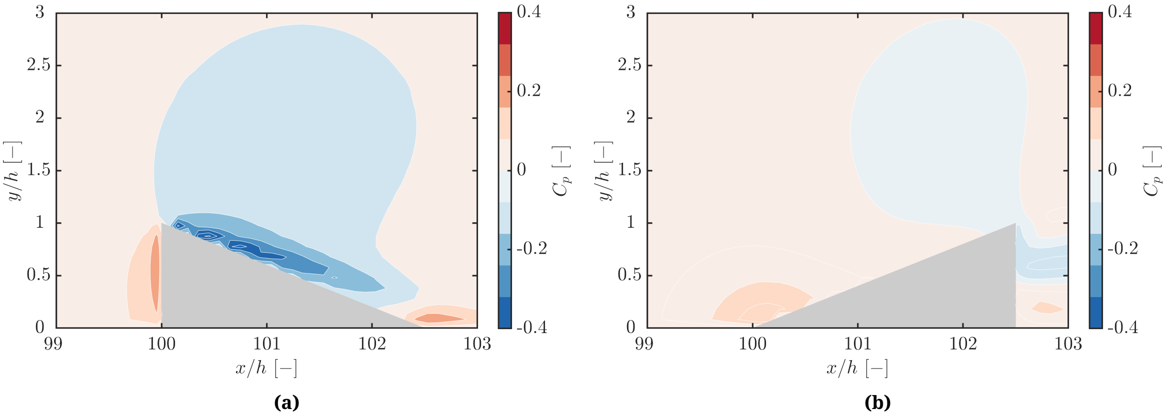

Figure 8.2: Contours of C_p along the actuator symmetry plane, measured at $\beta = 0$ degrees. Illustrations of: (*a*) Backward-facing ramp actuator, (*b*) Forward-facing ramp actuator.

skew angle: increasing the incidence angle tends to increase the frontal area of the actuator facing the flow, resulting in a linear increase in the side load for all three designs. Since the vane concept has been studied at higher angles of incidence compared to the ramps, with a similar lateral wall area, the side load forces reach higher load values. Similarly to the normal load, the side load may pose challenges for potential implementations of deployable VGs using the vane concept, as it could induce extension of the hinge, presumed to be oriented along the axial direction of the body. Overall, balancing the skew angle to minimize side loads while preserving the desired vorticity shedding by the actuator is crucial.

Precisely, shifting the focus towards the potential implementation of deployable versions of these design concepts, it is valuable to further characterize prospective design versions and compare their performance to the baseline designs. In this context, three additional concepts were numerically tested using the same CFD methodology: a curved version of the vane and a hollow version of the ramps (in forward and backward orientation).

The curved vane represents the baseline vane with the addition of fillets on the base, mimicking the bending of the material around the hinge axis. Conversely, the so-called hollow ramp concept involves the same ramp studied but without lateral walls, essentially transforming it into a single wedge-shaped plate bent at an angle of $21°$ with respect to the ground wall.

Upon reviewing the results presented in Figure 8.1 and Figure 8.5, it appears that the modification in the vane geometry has a minimal impact, with negligible variations in both loads and shed vorticity compared to the baseline version. However, the alteration on the ramp yields significant changes.

The variation in axial and side forces is relatively minor. Presumably, this is due to the inflow conditions at $\beta = 0$ degrees where the side load is not expected to vary significantly, and the increase in axial load is expected to be moderate as well. However, the normal load reveals a drastic change in both of the ramp configurations. Figure 8.1 illustrates that the value of the normal load doubles at $\beta = 0$ degrees. Interestingly, the effect of the hollow geometry induces similar yet opposite shifts in the results of the normal loads for the backward and forward ramps.

To provide visual context, Figure 8.3a and Figure 8.3b depict a slice along the symmetry plane of the hollow backward and forward ramp geometries, respectively, at $\beta = 0$ degrees.

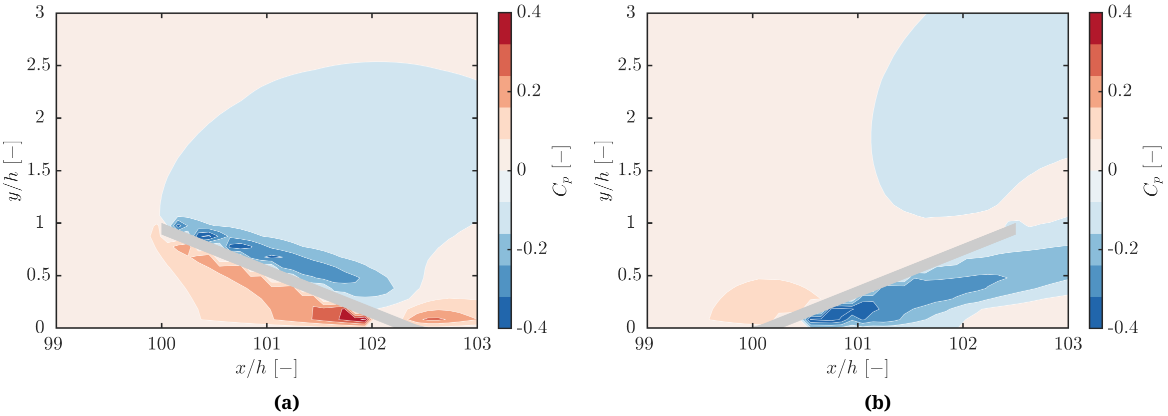

Figure 8.3: Contours of C_p along the actuator symmetry plane in streamwise direction, measured at $\beta = 0$ degrees. Illustrations of: (*a*) Backward-facing hollow ramp actuator, (*b*) Forward-facing hollow ramp actuator.

In this case, it becomes evident that the increase in normal load in the backward ramp is attributed to an augmented pressure difference between the upper and lower surfaces of the device. Specifically, the upper surface shows a region of low pressure comparable to the full geometry case, but the high-pressure area, particularly near the hinge axis, is amplified. Contrarily, the forward ramp showcases a similar high-pressure area near the hinge, but an amplified low-pressure region along the lower surface of the plate.

In addition, to quantify the effect of aerodynamic loads on a potential deployment mechanism, the moment coefficients with respect to the bending axis have been calculated. Figure 8.4 presents the aerodynamic moments relative to the body reference frame of the object. The reference point for the moment calculations is determined as the projection of the centroid on the ground wall for the vane concepts and the midpoint of the hinge axis for the ramp concepts.

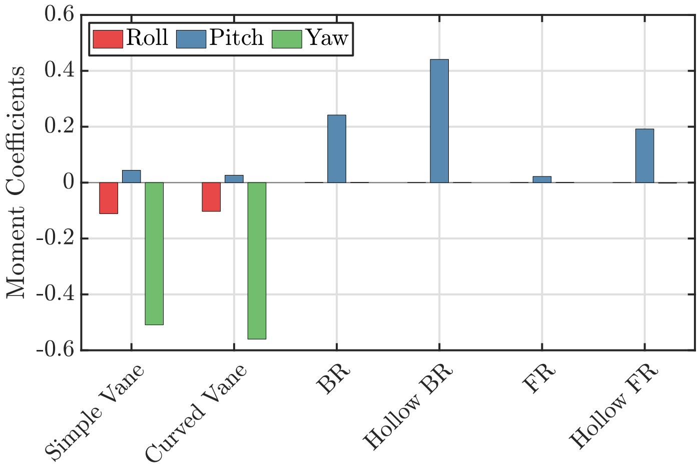

Figure 8.4: Aerodynamic moment coefficients with respect to the hinge axis.

From these results, it is evident that the effect of vane curvature near the wall is minimal. The shape of the geometry, in both simple and curved versions, primarily induces yaw and roll movements of the actuator. As anticipated, this moment is potentially detrimental in the long term for an SMA-actuated device.

Regarding the ramp designs, the results show that while the roll and yaw moments are negligible in both cases, the pitch moment is a significant factor. This aligns with the large normal loads presented previously. The implementation of a hollow version of the ramp is particularly critical in this regard. The pitch moment coefficient increases significantly—by 82.77% in the BR and a staggering 767.64% in the FR—compared to their respective baseline concepts.

8.2. Vortex strength

With the load and moment coefficients analyzed, the next step is to evaluate the effectiveness of the vortex generators in terms of vortex strength, a crucial parameter for understanding the aerodynamic performance of these devices. Ashill et al. (2005) provides a set of parameters, known as vortex descriptors, used to characterize vortices. These descriptors encompass, among others, the strength of vortices immediately downstream of the device. Figure 8.5 collects the results of the maximum vorticity measured immediately downstream of the VGs as a function of the skew angle.

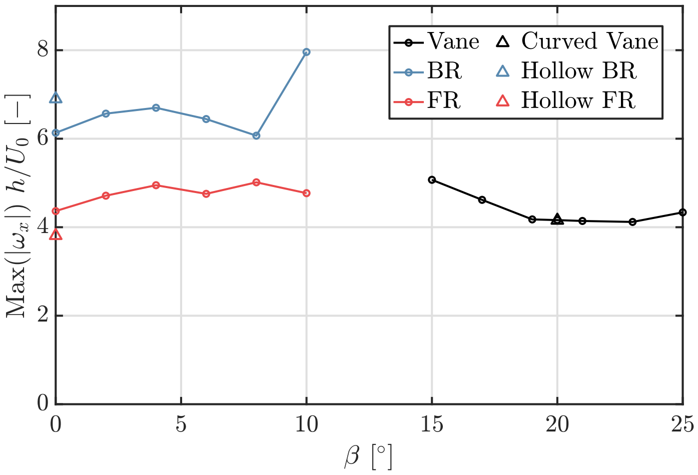

Figure 8.5: Maximum flow vorticity (ω_x) measured directly downstream of the actuator, in relation to the skew angle (β).

The ramp concept exhibits notable sensitivity to the inflow angle. Both the backward and forward-facing ramps show a linear increase in maximum shed vorticity for small angles of β. However, around $\beta = 4$ degrees, this trend changes: increasing the angle beyond this point no longer monotonically increases the vorticity value. For larger values of β, the vorticity shed by the forward ramp tends to oscillate around $|\omega_x|h/U_0 = 5.0$. In contrast, the backward ramp's vorticity decreases significantly to levels similar to those at $\beta = 0^\circ$, except at $\beta = 10^\circ$, where it shows a drastic increase and reaches the maximum total value.

In the case of single vanes, the highest shed vorticity values are observed at the smallest angle of incidence studied, i.e., $\beta = 15^\circ$. Beyond this angle, increasing the angle of attack leads to lower vorticity values. For $\beta > 19^\circ$, the configuration shows very little sensitivity, making it more robust under diverse flow conditions.

Regarding the disparities in vorticity magnitude among VG concepts, Figure 8.6 illustrates the comparison between vorticity fields immediately downstream of the conventional design (left) and the curved/hollow designs (right). In this comparison, it becomes evident that, consistent with observations from Figure 8.5, the influence of base curvature in the single vane configuration is nearly imperceptible, with both fields exhibiting nearly identical characteristics. The hollow FR design also showcases remarkably similar vortex structures to its solid counterpart, albeit with a slightly reduced vorticity magnitude. This is effectively captured in the difference in vorticity magnitude.

Conversely, the backward ramp, in accordance with the values of maximum streamwise vorticity, demonstrates noteworthy disparities between designs. Not only does the vorticity magnitude appear greater, but the vortex structure also exhibits slight deviations. Notably, less vortex core flattening occurs, since the vortex cores appear less compressed against the ground wall, potentially contributing to augmented lateral displacement, as evidenced by the contours.

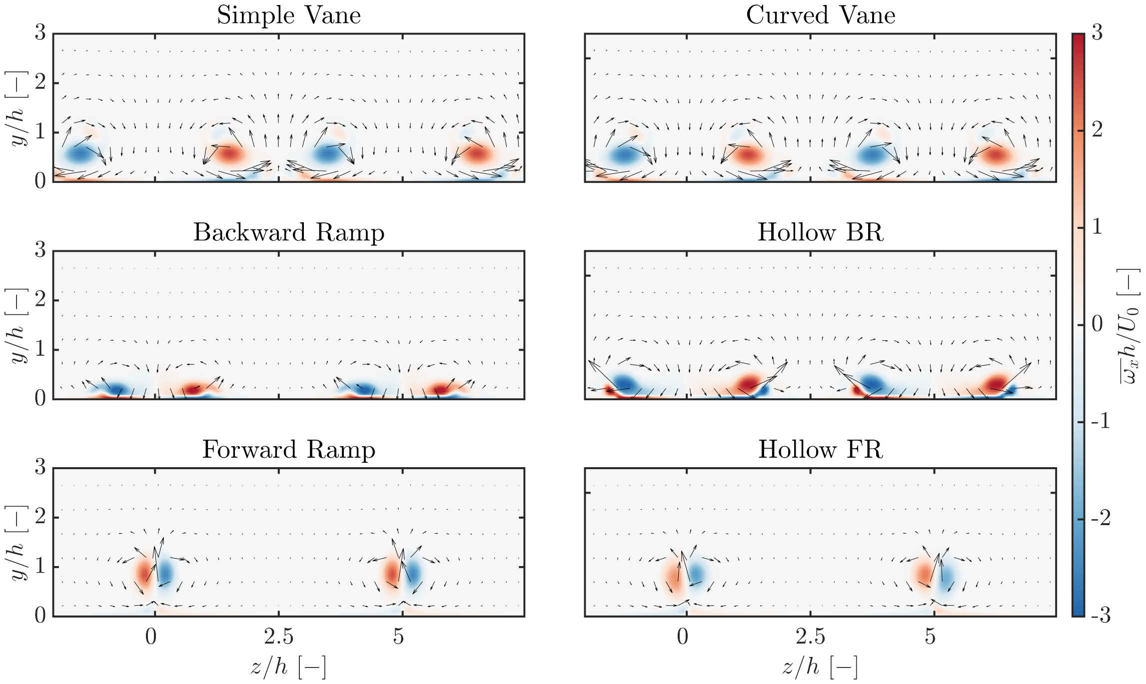

Figure 8.6: Comparison between conventional (*left*) and hollow/curved (*right*) VG designs: Contours with superposed velocity vector field of maximum streamwise flow vorticity ($|\omega_x|$) measured directly downstream of the actuator.

The numerical study presented in this chapter offers important insights into the sensitivity of multiple vortex generator designs to the skew angle in a ZPG flat plate configuration. Via the analysis of the aerodynamic loads, moments and vortex shedding, the three primary actuator concepts, along with three secondary designs, have been characterized. These findings reveal substantial variations in loads and moments across different VG designs. This underscores the necessity for meticulous design considerations to mitigate stresses along the hinge axis, in a potential future implementation of deployable VGs.

Moreover, the study showcases the advantages of the vane design, characterized by moderate sensitivity to inflow angles and comparable vorticity shedding to the ramp designs. In this case, it is important to note that in a counter-rotating vane array setup, the vorticity would be shed by two actuators simultaneously, potentially enhancing the mixing capabilities. However, the vane design faces challenges in terms of side loads and moments, which align with the rotation direction of a potential hinge. This suggests that a mechanism actuated using shape memory alloys would deteriorate rapidly after a few cycles or lead to aeroelastic phenomena, requiring a redesign of the actuation mechanism.

Furthermore, the exploration of additional concepts, such as the hollow ramps, reveals significant alterations in aerodynamic loads with respect to the baseline designs. In particular, the hollow ramp concepts show potential problems with normal loads and pitching moments, aligning with the rotation direction of a potential hinge. Consequently, similar to the vane design, a mechanism actuated using shape memory alloys would likely deteriorate rapidly after a few cycles.

The complementary experimental study into the aerodynamic efficiency of these designs in controlling the flow separation presented in the next chapter will provide a different scope and valuable insights. By assessing factors such as boundary layer control, separation bubble characteristics, and overall flow control effectiveness, the full picture of VG performance for flow control can be assessed and informed decisions can be made about the viability and performance of each design concept.

9

Uncontrolled flow characterization

This chapter aims to present an analysis of the uncontrolled separated flow generated by the adverse pressure gradient induced by the test section conditions. This analysis will serve as a baseline against which the flow control capabilities of the studied actuators will be assessed.

Following this effort to characterize the incoming flow, Section 9.1 begins by identifying the relevant metrics necessary for a comprehensive evaluation of the flow field. Following this, Section 9.2 presents an analysis of the mean flow field results, detailing the overall behavior and properties of the uncontrolled flow and the separation bubble. Finally, in Section 9.3 the characterization of the boundary layer is examined, providing insights into its development and impact on the flow dynamics. This thorough investigation establishes a fundamental understanding of the uncontrolled flow, essential for assessing the effectiveness of various flow control techniques.

9.1. Relevant metrics

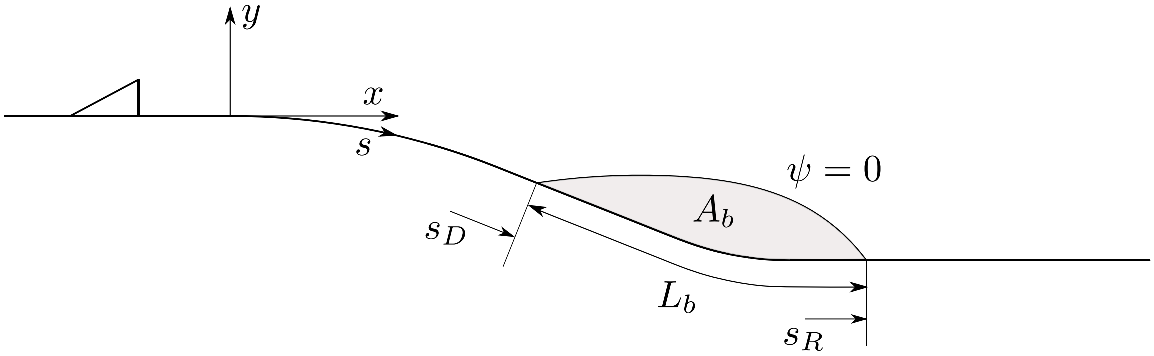

Figure 9.1: Schematic representation of the curved backward-facing ramp along with the multiple coordinate systems and the magnitudes for the analysis of the separation bubble.

Before moving to the analysis of the uncontrolled flow, it is convenient to introduce the analysis metrics relevant to the quantitative study of both, controlled and uncontrolled flows.

Illustrated in Figure 9.1 is a schematic representation of the curved backward-facing ramp under study, along with the multiple coordinate systems under consideration and the significant magnitudes for the analysis of the separation bubble.

As depicted in the figure, in addition to the Cartesian reference frame centered at the inception of the ramp's curvature, a wall coordinate s is established, also centered at this origin. This coordinate facilitates the measurement of the separation bubble's length (L_b) along the wall. Furthermore, the area of the separation bubble (A_b) is defined by convention as the area enclosed between the $\psi = 0$ line and the wall.

Specifically, the $\psi = 0$ curve has been selected to define the upper boundary of the separation bubble due to its efficacy in representing the obstruction encountered by the incoming flow. Furthermore, this streamline intersects the wall at the locations of Total Detachment (TD) and Total Reattachment (TR), where the mean streamwise velocity is also null, thereby offering a robust indicator of the bubble dimensions.

Among the metrics and parameters that will remain consistent throughout this study are:

- The $U = 0$ curve, which denotes the locus of null streamwise velocity, conventionally represented as a dashed line in this report.
- The $\psi = 0$ curve, indicating the *zero streamline*. At this position, the net volume flux across the wall-normal direction becomes null. It is conventionally represented as a solid line in this report. Its y coordinates are defined by integrating the streamwise velocity profile in the wall-normal direction and finding the zero-crossing, if it exists:

$$y(x, \psi = 0) = \{y : \int_0^y U(x, y')dy' = 0\} \tag{9.1}$$

- The backflow coefficient χ, denoting the percentage of the time in which the flow is reversed, i.e. $U < 0$.
- Markers denoting various flow conditions, including:
  - Incipient Detachment/Complete Reattachment (ID/CR): $\chi = 0.01$.
  - Intermittent Transitory Detachment/Reattachment (ITD/ITR): $\chi = 0.20$.
  - Transitory Detachment/Reattachment (TD/TR): $\chi = 0.50$.

9.2. Mean flow

The metrics presented in Section 9.1 provide a robust framework for evaluating and interpreting the flow behavior throughout this study. With these established, we now transition to the analysis of the mean flow field to gain further insights into the flow dynamics. The PIV measurements of the uncontrolled mean flow were obtained through the averaging of a total of 500 images. Figure 9.2 depicts the mean streamwise velocity field, accompanied by the $U = 0$ and $\psi = 0$ contours.

Across all three recording planes, a prominent separation bubble area is evident, setting an ideal condition for assessing the efficacy of the flow control actuators. However, to gain a finer understanding of the uncontrolled flow dynamics, it is important to note the variance of the flow field along the test section span. Notably, shifting the recording plane in the spanwise direction correlates with a reduction in the separation bubble area, a phenomenon which can

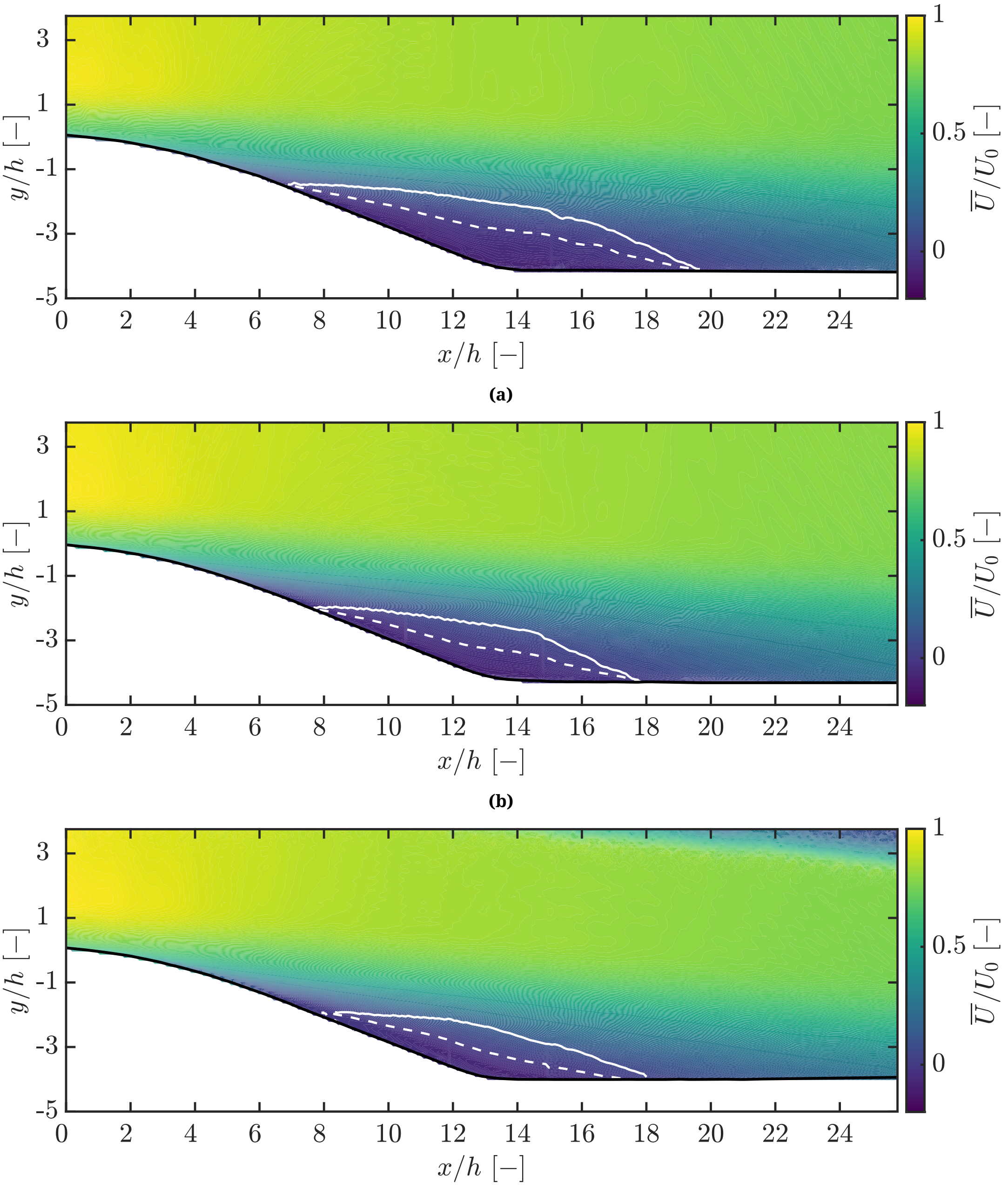

(a)

(b)

(c)

Figure 9.2: Contour map of mean streamwise velocity $\overline{U}/U_0$ with overlayed $U = 0$ (- - -) and $\psi = 0$ (——) curves. (*a*) Center plane; (*b*) Middle plane; (*c*) Off-center plane. *Note: the area of low velocity observed in the top right corner of* (*c*) *is attributable to a modification in the laser setup, specifically a reduction in the laser beam width. This alteration does not correspond to the actual flow physics.*

be directly attributed to the limited spanwise extent of this test section, leading to end-effects arising due to the influence of the lateral walls' boundary layer. It is noteworthy that the boundary layer on the lateral walls has a way longer development length than that of the floor (originating merely 0.7 m upstream), implying that the boundary layer thickness of the lateral walls may extensively exceed that of the floor plate.

In addition to the velocity field, the dataset also facilitates the computation of the backflow coefficient χ, representing the percentage of time during which the flow is reversed. Figure 9.3 depicts the contours of the backflow coefficient, accompanied by the $U = 0$ and $\psi = 0$ contours, along with the makers denoting ID, ITD, TD, TR, ITR and CR points (from left to right). It is pertinent to note that regions with $\chi < 0.01$ are left blank for clarity.

The computation of the backflow coefficient contours facilitates the determination of the remaining relevant metrics for the study of the separation bubble, as introduced in Section 9.1. The measurements of bubble area and length, along with their relative deltas with respect to the results of the center plane are summarized in Table 9.1. Notably, the observed decrease as the recording plane is shifted in the spanwise direction reaches values up to 39.26% and 24.53% in area and length, respectively. These results validate the hypothesis that the flow field in this test section predominantly exhibits 3D characteristics, with the end-effects due to the boundary layer of the lateral walls exerting a significant influence on the final results.

Additionally, Figure 9.4 shows a comparative analysis of the detachment and reattachment points for the different separation regions along the span. These results highlight the fact that, due to the smooth curvature of the backward-facing ramp, the separation phenomenon does not occur at a fixed position, but rather intermittently along a wide region of between $2h$ (center plane) and $3h$ (off-center plane). Moreover, consistent with similar studies, the detachment region appears significantly smaller than the reattachment region, indicating a higher variability in the reattachment positions compared to detachment ones.

Table 9.1: Summary of separation bubble measurements for all three recording planes.

Plane	A_b $\times 10^3$ [m^2]	L_b [m]	ΔA_b [%]	ΔL_b [%]
Center	6.157	0.265	–	–
Middle	4.507	0.226	-26.80	-14.72
Off-Center	3.740	0.200	-39.26	-24.53

9.3. Boundary layer characterization

In addition to the analysis of the mean flow results, an attempt to characterize the incoming uncontrolled flow entails analyzing the PIV measurements of the streamwise planes at the location immediately preceding the detachment region, where the flow is assumed to be relatively undisturbed, thus enabling the characterization of the boundary layer. To achieve this, it is advantageous to employ slightly modified window size settings for the PIV postprocessing. Unlike the baseline postprocessing parameters utilized in the rest of the analysis, for this specific purpose, a smaller window size with a high aspect ratio is preferred, since it allows to obtain a higher resolution, especially in the near-wall area, where PIV postprocessing techniques usually show limitations.

Specifically, in order to obtain the following results, a window size of 8×8 pixels with an elliptical weighting factor of $4:1$ was employed. This configuration allows for finer resolution in

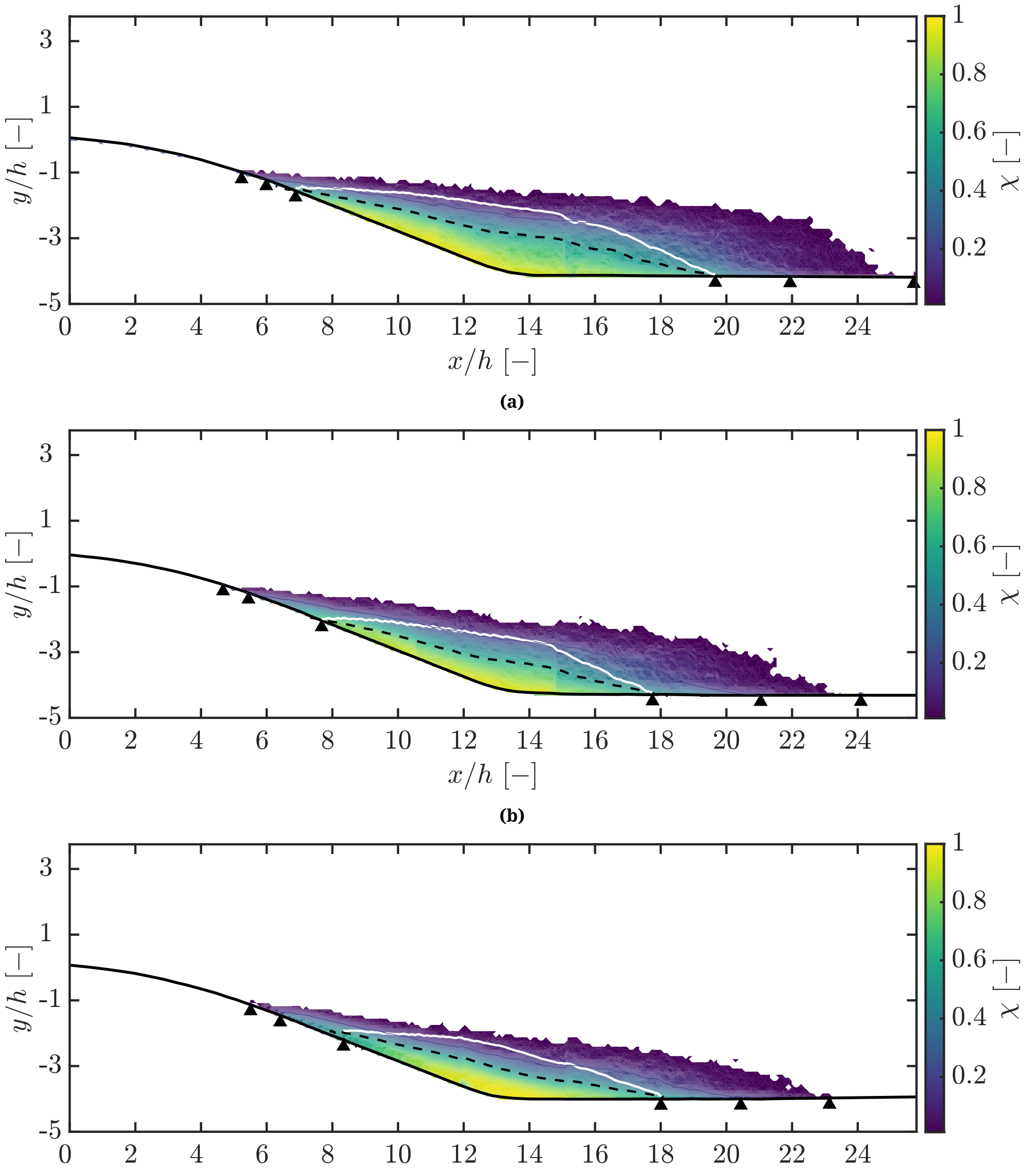

(a)

(b)

(c)

Figure 9.3: Contour plots of backflow coefficient with overlayed $U = 0$ (dashed) and $\psi = 0$ (solid) curves and ID, ITD, TD, TR, ITR and CR markers (in this order, from left to right). (*a*) Center plane; (*b*) Middle plane; (*c*) Off-center plane.

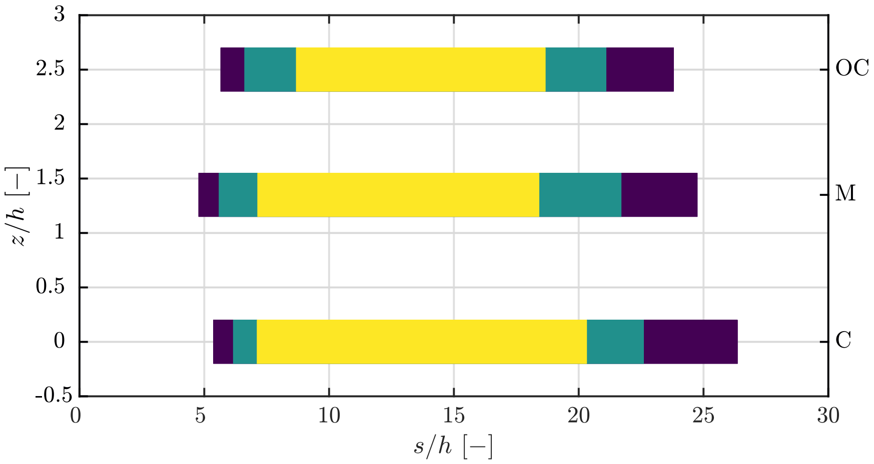

Figure 9.4: Comparison of detachment and reattachment points along the ramp span. Wall segment between: TD and TR in *yellow*, ITD and ITR in *green*, ID and CR in *blue*. C stands for center plane, M for middle plane and OC for off-center plane.

the wall-normal direction, crucial for resolving the sharp velocity gradient in the near-wall region.

Figure 9.5 presents a comparison of the boundary layer velocity profiles obtained from all three streamwise recording planes, along with the integral boundary layer properties derived from these profiles. The average of the measured freestream velocities, calculated as 17.61 m/s, will be adopted as the freestream velocity U_0 for subsequent analyses in the report.

Unlike the results of the uncontrolled flow separation bubble, where the measurements are highly influenced by 3D effects of the spanwise flow, the boundary layer measurements are taken upstream of the separation region, specifically at the inception of the ramp. Given the location of these measurements, it is reasonable to assume that the observed variability in boundary layer characteristics along the test section span is predominantly influenced by factors such as measurement uncertainty rather than substantial physical variations in the flow itself. Notably, the boundary layer thickness, defined as the wall-normal distance where the local mean velocity reaches 99% of the freestream value, exhibits slight variations across the test section span, ranging from 30.0 mm in the center plane to 26.7 mm in the off-center plane. These slight variations can be attributed to the measurement uncertainty and are consistent with expectations for boundary layer behavior in this experimental setup.

In a further effort to characterize the incoming uncontrolled flow, an approach to estimate the friction velocity (u_τ) involves depicting the boundary layer velocity profile using the nondimensional magnitudes y^+ and u^+. It is assumed that every boundary layer follows the same general topology, comprising a viscous sublayer and a log-law region, and complemented by an intermediate buffer layer region situated between the two. Additionally, due to the limited accuracy of the PIV measurements near the wall, most of the data points are expected to fall within the log-law or the outer layer region. Under the assumption that the measurements should conform to the theoretical log law, u_τ emerges as the only free parameter within Equation 2.8 that can be adjusted to achieve a satisfactory fit between the observed and theoretical curves.

Figure 9.6 depicts the outcomes of adjusting the friction velocity to maximize the correlation, quantified using the R^2 indicator, between the experimental data and the theoretical

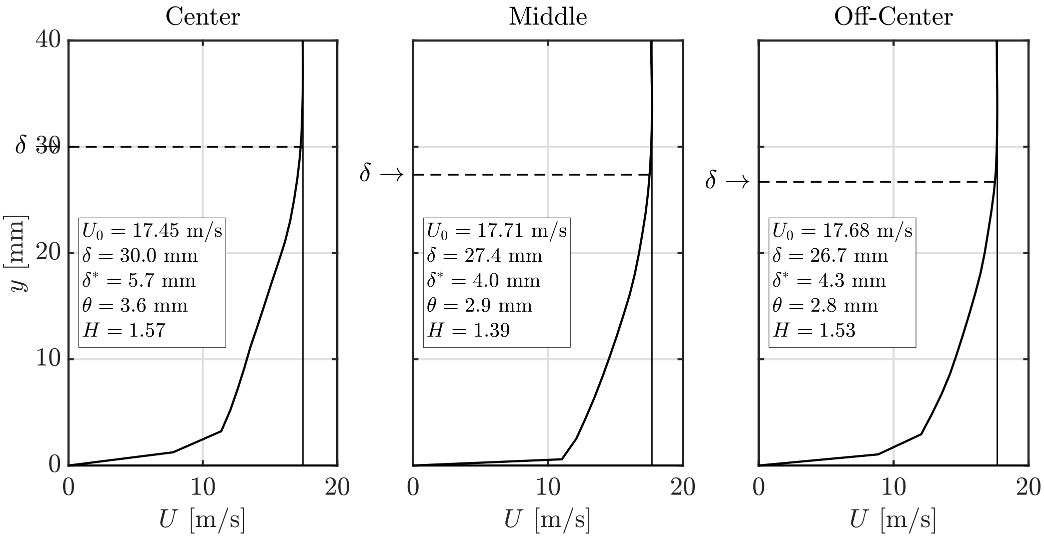

Figure 9.5: Comparison between the boundary layer velocity profiles.

curve. The correlation has been computed within the regions deemed well-predicted by the logarithmic law of the wall, specifically between the upper limit of the buffer layer (set at $y^+ = 30$) and the lower limit of the outer layer (set at $y^+ = 300$), both depicted as dashed lines in the plot. Data points identified as outliers, denoted by crosses, have been excluded from the calculation to enhance the accuracy of the results.

Overall, the results show a strong correlation with the theoretical law. However, again it is important to note that the observed variability in boundary layer characteristics along the test section span is likely attributable more to measurement uncertainty than to actual physical variations in the flow.

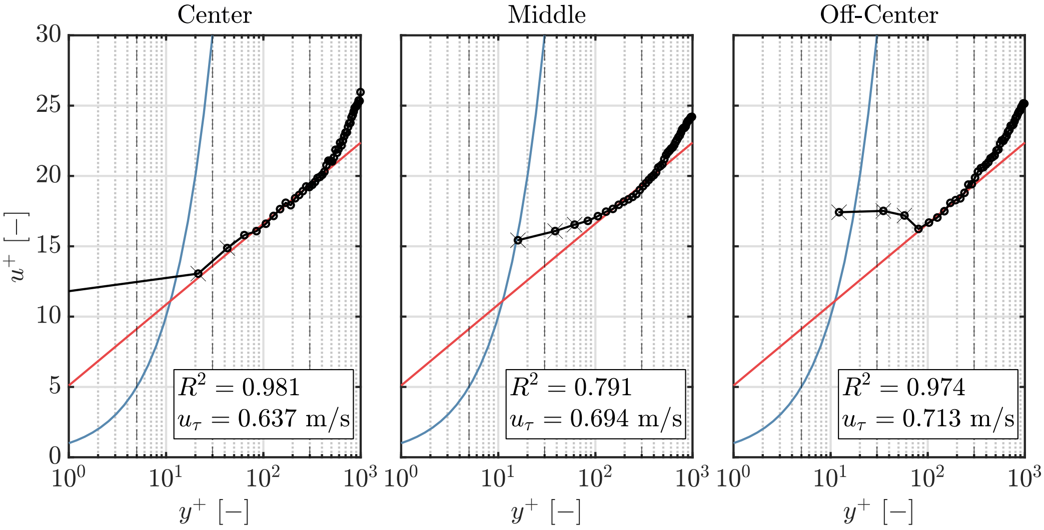

Figure 9.6: Inner-scaled mean flow streamwise velocity profile expressed in nondimensional form. Linear in *blue*, log-law in *red*, experimental data in *black*.

For reference, Table 9.2 provides a summary of all key boundary layer parameters upstream of the ramp across all three recording planes, alongside their respective average values and derived metrics.

Table 9.2: Parameters of the uncontrolled turbulent boundary layer upstream of the ramp across all three recording planes.

Plane	U_0 [m/s]	δ [mm]	δ^* [mm]	θ [mm]	H [$-$]	u_τ [m/s]	Re_τ [$-$]	Re_θ [$-$]
Center	17.45	30.0	5.7	3.6	1.57	0.64	1288	4450
Middle	17.71	27.4	4.0	2.9	1.39	0.69	1269	3447
Off-Center	17.68	26.7	4.3	2.8	1.53	0.71	1272	3322
Mean	17.61	28.0	4.7	3.1	1.50	0.68	1276	3740

10

Controlled flow characterization

This chapter aims to analyze the controlled flow downstream of the separation region influenced by the applied flow control strategies. In contrast to the uncontrolled flow discussed in the preceding chapter, this analysis focuses on assessing the efficacy of various VG concepts in mitigating separation and modifying flow behavior.

First, Section 10.1 examines the flow characteristics along the wall-normal streamwise planes, in an attempt to quantify the flow control capabilities of the various VGs. Subsequently, Section 10.2 presents the flow measurements along the wall-normal spanwise planes, in an attempt to understand the diverse vortex systems created and their potential effect on the separated flow.

10.1. Streamwise planes

Figure 10.1 presents the results of the percentage reduction in separation bubble area (A_b) with respect to the uncontrolled case for both the central and the off-center planes. This plot includes all four different VG designs across the four different actuator positions upstream of the ramp. To maintain clarity and visual simplicity, the results from the middle plane have been excluded as they only provide data points for two out of the four VG designs (CtR and CoR), all of the results can be found summarized in Table 10.1. It is important to note that all results are relative to their respective uncontrolled cases, which vary for each plane, as demonstrated in Chapter 9.

10.1.1. Center plane

Several conclusions can be drawn from these findings. Focusing on the results obtained from the center plane, depicted as a solid line, a prominent observation is the notable ineffectiveness of the forward ramp concept. It is evident from the plot that, for positions $x_{VG}/h > 15$, namely $28h$ and $18h$ upstream of the ramp, this concept demonstrates minimal flow control effectiveness, resulting in a negligible impact on the bubble size area. While a closer streamwise position demonstrates some extent of reduction in separation bubble area (up to 29.85%, notably at $x_{VG}/h = 10.5$), shifting the actuator too close to the separation ramp to $x_{VG}/h = 4.5$ results again in a drop in flow control performance, leading to only a 11.13% reduction.

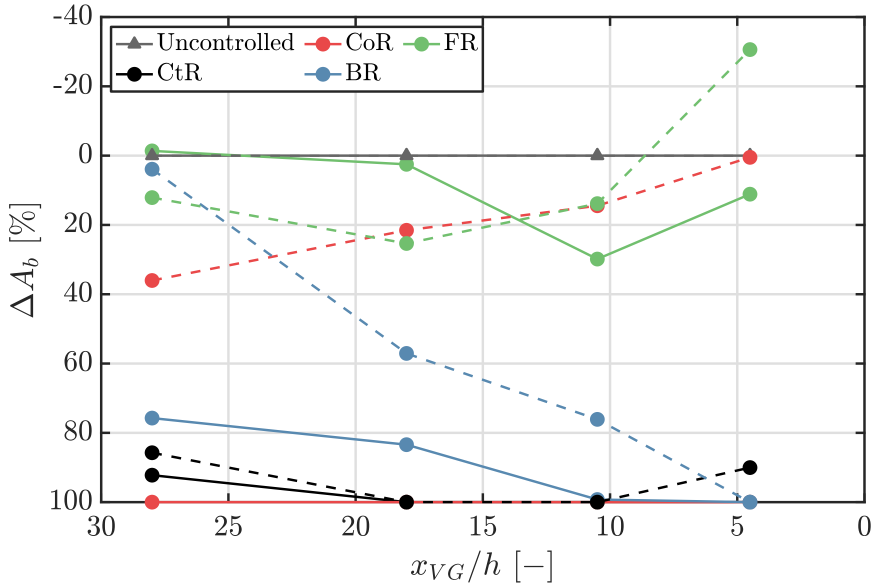

Figure 10.1: Percentage reduction in separation bubble area (A_b) compared to the uncontrolled case. Center plane (——), Off-center plane (- - -).

Conversely, the backward ramp displays overall superior results and potential for further investigation and application. The position farthest from the ramp ($x_{VG}/h = 28$) exhibits a 75.74% reduction in bubble area. However, as the actuator is shifted downstream, the flow control efficiency tends to improve, culminating in a complete elimination of the separation bubble at the two closest streamwise positions to the ramp.

Regarding the vane actuators, the counter-rotating vane array demonstrates excellent flow control capabilities, with only a small region of separation evident at the $x_{VG}/h = 28$ position, while the remaining streamwise positions demonstrate optimal results. In contrast, the co-rotating vane array achieves perfect outcomes across all four streamwise positions. These findings suggest that, over such a development length and considerable distance from the ramp, neighboring vanes in the counter-rotating array may exert a detrimental effect on the decay and trajectory of vortices.

Specifically, the difference in results between the vane setups can potentially be attributed to two main factors. Firstly, in the co-rotating case, all vanes induce a downwash at the centerline, possibly giving the system more control over separation than in the counter-rotating case, where the induced velocity at the centerline is a mix of upwash and downwash. Secondly, the presence of more streamwise vortices in the counter-rotating array might alter the trajectories of the vortices. Further investigation of the crossflow vortex dynamics in this report will provide more insights into these phenomena.

10.1.2. Off-center plane

To assess the efficient spanwise flow control capabilities of each vortex generator system, also the percentage reduction in bubble area in the off-center plane (the plane between VG actuators) was studied.

In this case, the forward ramp model shows still a significant ineffectiveness. While the two positions farther away from the ramp, namely $28h$ and $18h$ upstream of the ramp, demonstrate slightly improved results compared to those recorded in the central plane, with reduction values around 12% and 25%; shifting the actuators closer to the ramp yields a clear detrimental effect. At streamwise positions in proximity to the ramp, this design not only proves unproductive but may trigger the flow separation, as evidenced by the off-center plane result at $x_{VG}/h = 4.5$. This outcome could be attributed to the significant upwash generated by the device, indicating that the vortex system developed near the wall surface is insufficient to control the flow. Moreover, as suggested by Ashill et al. (2002), it is also likely that this actuator also separates the boundary layer upstream of itself in the presence of an adverse pressure gradient.

In contrast, the backward ramp exhibits a significant decline in performance compared to recordings from the central plane. At the position farthest from the ramp ($x_{VG}/h = 28$), this design demonstrates limited effectiveness. Nevertheless, noteworthy improvement in flow control efficiency in both of the recording planes is observed as the actuator is shifted downstream, leading to a perfect 100% reduction in bubble area at the position closest to the ramp. This outcome suggests that this design suffers from a rapid decay in control power along the streamwise direction, possibly influenced by a decay in vortex strength and the trajectory of the vortex core.

Regarding the vane actuators, the results exhibit remarkable agreement with the literature, in particular with studies by Lin (2002) or Godard and Stanislas (2006). The counter-rotating vane array demonstrates excellent flow control capabilities, particularly at the two central positions in the streamwise direction, $x_{VG}/h = 18$ and $x_{VG}/h = 10.5$. Moreover, it demonstrates strong agreement between the center and off-center planes, indicating efficient spanwise flow control capabilities as observed in the aforementioned studies. Only small regions of 9.98% and 14.26% of the uncontrolled separation bubble are present in the off-center plane for the $x_{VG}/h = 28$ and $x_{VG}/h = 4.5$ positions, respectively.

In particular, the region of separation observed at $x_{VG}/h = 4.5$ can be attributed to the proximity of the actuators to the separation location. The mixing in this region can induce significant spanwise inhomogeneity and, according to Ashill et al. (2005), just downstream of the vanes, the vortices induced by counter-rotating VGs can cause an increase in the boundary layer shape factor, indicative of a higher potential for flow separation. This phenomenon may be explained by the vortices sweeping low-energy air from either side of them into the boundary layer.

Conversely, the co-rotating vane array exhibits a drastic decrease in performance compared to recordings from the central plane. Results from this plane indicate a significant decline in flow control capability, which deteriorates as the distance to the ramp decreases, ultimately resulting in null flow control efficiency at $x_{VG}/h = 4.5$. This finding corroborates previous studies on vane-type vortex generators, such as Lin (2002), which conclude that counter-rotating VGs tend to be more effective in controlling a 2D type of flow (like this backward-facing ramp), while co-rotating arrays perform better in 3D separation scenarios (such as swept wings or inside compact-duct inlets).

In summary, the previous results suggest that the counter-rotating array of vanes emerges as the overall best-performing actuator, demonstrating robustness under different circumstances. This finding aligns with the aforementioned relevant studies in the literature. However, as introduced in Chapter 8, a significant potential drawback of these devices, particularly when considered for deployable vortex generators, is the structural stress to which the vane joint is subjected. The design under study in this report consists of a vane protruding normal to the ground surface. Hence, it is conceivable that a potential version manufactured using shape memory alloy actuation may struggle to maintain this shape for an extended period under the effect of aerodynamic loads. Therefore, it is pertinent to consider the promising results of the backward ramp design as a more feasible, backup option, if needed.

To gain deeper insights into VG performance, understanding the evolution of the vortex system (including its strength and trajectory) generated by the VGs in space is crucial. The subsequent section delves into the crossflow field analysis.

Table 10.1: Percentage reduction in separation bubble area (A_b) compared to the uncontrolled case.

	$x_{VG}/h = 28$	$x_{VG}/h = 18$	$x_{VG}/h = 10.5$	$x_{VG}/h = 4.5$
Center Plane				
Ct-R	92.22%	100%	100%	100%
Co-R	100%	100%	100%	100%
BR	75.74%	83.41%	99.24%	100%
FR	-1.37%	2.51%	29.85%	11.13%
Off-Center Plane				
Ct-R	85.74%	100%	100%	90.02%
Co-R	36.04%	21.54%	14.47%	0.49%
BR	3.92%	57.08%	76.11%	100%
FR	12.11%	25.35%	13.85%	-30.60%
Middle Plane				
Ct-R	73.28%	100%	100%	100%
Co-R	99.99%	100%	100%	100%

10.2. Crossflow planes

To comprehensively assess the flow control capabilities of each VG design, it is very useful to analyze not only the streamwise flow field but also the crossflow flow fields. According to Wendt et al. (1993), the vortex is best characterized in the crossflow plane, where the pattern of secondary flow properties provides a graphical depiction of the vortex structure. These recording planes, normal to the flow direction, allow for the observation of the wall-normal (y) and spanwise (z) components of the velocity. Additionally, both the velocity and vorticity fields help in understanding the vortex system created and its potential effect on the separated flow.

10.2.1. Comparison between CFD and PIV

Before delving into the analysis of the experimental results, it is interesting to first gain a deeper understanding of the impact of an APG on the vortex structures. Since no experiments were performed under zero pressure gradient conditions in this research, this understanding can be facilitated by comparing the scenario with APG, represented by the experimental data, with the scenario with ZPG, represented by the numerical data.

It is crucial to acknowledge that this comparison serves as an estimation, considering the presence of other influencing factors beyond the APG affecting the disparity between results. The CFD approach relies on RANS modeling, employing an eddy viscosity model to model the whole range of turbulence scales. While efficient and cost-effective, this approach struggles to accurately predict complex turbulent flows with secondary motions and swirling effects (see Bush et al. 2019). Additionally, the numerical model does not fully replicate the walls of the wind tunnel section, hence it also neglects the effect of the lateral walls, which tend to induce spanwise 3D flow, as discussed in Chapter 9.

Qualitative assessment of vortex flow is achieved by juxtaposing vorticity fields captured by PIV under APG and flow separation conditions with CFD results obtained for ZPG flat plate conditions. Figure 10.2 illustrates the comparison between the vorticity fields of all four VG actuator arrays located at the downstream-most position ($x_{VG}/h = 4.5$) for both PIV and CFD results.

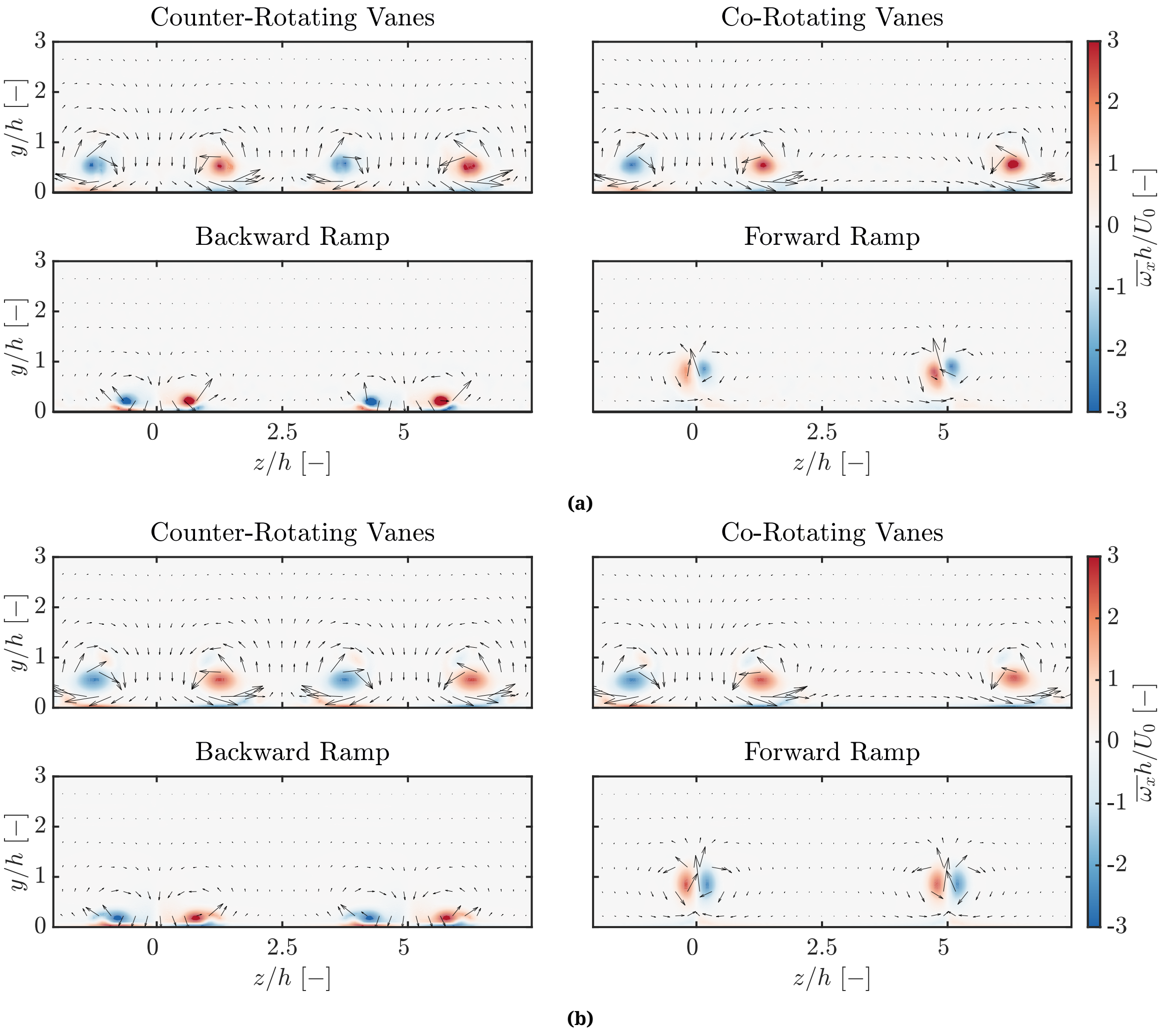

(a)

(b)

Figure 10.2: Mean flow streamwise vorticity $\overline{\omega_x}h/U_0$ contours with superposed velocity vector field for all four actuators in $x_{VG}/h = 4.5$. (*a*) PIV measurements; (*b*) CFD results. Only one out of every 4 vectors in the z-direction and one in 8 vectors in the y-direction is shown for clarity.

Overall, noticeable differences are evident between the PIV and CFD results. For both vane array systems, show a remarkable difference in vortex cores. Larger core diameters, typically associated with APG conditions, as indicated by previous studies such as Westphal et al. (1987), are attributed to increased vorticity diffusion leading to larger vortex center growth. In this case, however, the largest vortex cores are present in the CFD results.

This discrepancy between results may stem from two factors. Firstly, the recording plane immediately downstream of the actuators captures vortices strong enough to overcome the effects of the APG at this very early stage. This idea is supported by the findings of Ashill et al. (2002), who noted that in $2h$-spaced vanes, the vortex strength just downstream of the vanes is not significantly affected by the APG (the vane spacing in this research is $2.5h$). Secondly, the larger vortex cores in the CFD results are not due to the typical vortical diffusion of an APG, but rather could be influenced by numerical diffusion inherent to RANS modeling.

In addition, Ashill et al. (2001) suggest that an APG affects the vortex strength by reducing the effective height of the device. In this context, both ramp designs show noticeable changes in the vortex shape, particularly observable in the case of the backward ramp, which shows flatter vortex structures closer to the ground wall in the CFD results. According to Westphal et al. (1987), this contour flattening occurs when the vortex core grows to a sufficient fraction of the height of the vortex center from the wall. Given the larger vortex core growth rate of the CFD results, this phenomenon is expected to occur earlier in the vortex lifespan in this scenario. Nevertheless, in their studies Lögdberg et al. (2009) showed that the pressure gradient effectively accelerates this phenomenon, hence it is likely to manifest after a longer development distance in the APG scenario too.

To further analyze the lateral and vertical displacement of the vortices, Figure 10.3 presents superposed iso-vorticity contours ($|\omega_x|h/U_0 = 0.90$) for all four VG designs. Additionally, Figure 10.4 shows the iso-vorticity contours with the actuators positioned two steps upstream at $x_{VG}/h = 18$. To enhance visual clarity and account for the decay in vortex strength, the iso-contour represented corresponds to $|\omega_x|h/U_0 = 0.34$.

As suggested by Jeong and Hussain (1995), various methods for vortex identification exist, including the $Q-$, λ_2-, $\Delta-$, and $|\omega|-$ criteria. For consistency with the relevant literature, this study defines the vortex center as the position of maximum absolute streamwise vorticity, $|\omega_x|_{max}$. Similar to the findings of Lögdberg et al. (2009), the vortices generated by the VGs are relatively strong and steady, suggesting that any of these methods would be effective. The plot illustrates the significant increase in vortex area, particularly for the vane designs, and highlights substantial differences in spanwise displacement across the cases.

Comparing the results at both positions reveals an acceptable correlation between PIV and CFD results. The effect of the adverse pressure gradient (APG) is less pronounced than in the case of the vorticity contours. The size of the primary vortex cores and the position of maximum vorticity show a high correlation, particularly for recordings with the actuators at $x_{VG}/h = 4.5$. Consistent with the vorticity contours, CFD results indicate slightly larger vortex cores. A notable difference is observed in the shape of the main vortex cores generated by the backward-facing ramp, where the CFD results clearly depict a flattening of the cores.

As the distance from the actuator increases, the differences between the methods become more pronounced due to the increasing complexity of the turbulent flow and the influence of secondary motion and swirling effects on vortex decay and trajectories. Nevertheless, for most of the development length of the vortices originating at $x_{VG}/h = 18$, the streamwise pressure gradient is moderate, consistent with the setup of the ceiling wall depicted in Figure 7.5. This results in a reasonable correlation between methods despite differences in test conditions.

The primary cores of the FR vortex system dissipate effectively after $18h$, and are thus not captured by any of the methods. Interestingly, the vortex cores in CFD results are no longer consistently larger than those in experimental results; they are similar in size or even smaller,

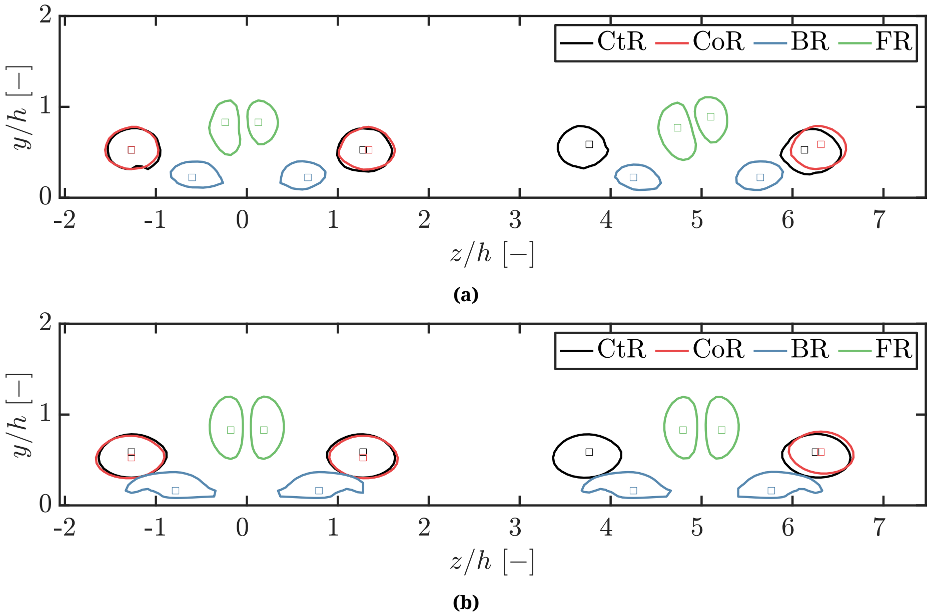

(a)

(b)

Figure 10.3: Contours of $|\omega_x|h/U_0 = 0.90$ in (*a*) PIV measurements; (*b*) CFD results for $x_{VG}/h = 4.5$. Point of maximum absolute streamwise vorticity $|\omega_x|_{max}$ represented by □.

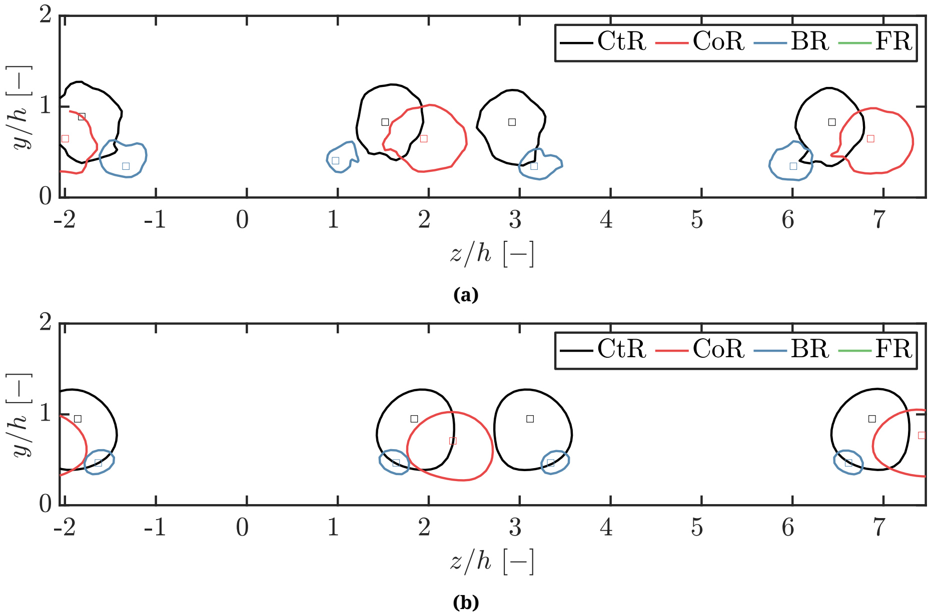

(a)

(b)

Figure 10.4: Contours of $|\omega_x|h/U_0 = 0.34$ in (*a*) PIV measurements; (*b*) CFD results for $x_{VG}/h = 18$. Point of maximum absolute streamwise vorticity $|\omega_x|_{max}$ represented by □.

as observed in the BR vortex system. This suggests that RANS modeling may have a dissipative effect equivalent to that of the APG.

Regarding the vane actuators, the CtR vane results show substantial correlation in shape and size with the PIV results. However, the CFD results, particularly for the CoR VG, exhibit a greater tendency for outward displacement and asymmetry compared to PIV results. This displacement can be partly attributed to the effect of wall blockage. Since CFD employs a slip boundary condition on the lateral wall to simulate infinite-extent conditions, the effect of the lateral walls is neglected, potentially leading to an overestimation of this lateral displacement. A more detailed examination of the vortex trajectories will be presented in a subsequent section of this report.

10.2.2. PIV measurements: $x_{VG}/h = 4.5$

Following the comparative analysis of experimental and numerical findings, the pure experimental results are now presented, examining the controlled flow dynamics induced by the VG actuators. Figure 10.5 and Figure 10.8 depict the nondimensional vorticity and velocity fields for all four VG designs, tested at two different streamwise positions, namely $x_{VG}/h = 4.5$ and 18 upstream of the ramp inception. The first set of recordings, with the actuators located at $x_{VG}/h = 4.5$ provides the flow field $2h$ downstream of the actuators, allowing a clear visualization of the developed vortex system characterizing each of the designs. Conversely, the second set of measurements, with the actuators positioned at $x_{VG}/h = 18$, i.e. 32 centimeters upstream of the recording plane, allows for the analysis of the streamwise vortex decay and the evolution of the vortex trajectories.

From the vorticity contours, along with the superimposed vector field, it is possible to infer the topology of the vortex systems developed by each of the actuator arrays. Firstly, the CtR vane array produces two pairs of well-defined counter-rotating vortices, inducing significant regions of common downwash and upwash in the between vanes and between VG pairs, respectively. Notably, while the region of common downwash is expected to cause the strongest distortion of the boundary layer over the greatest streamwise extent, according to Pauley and Eaton (1988), the common upwash vortices interact strongly with each other, but only weakly with the viscous flow near the wall and their image vortices. This phenomenon explains the relatively poorer results in bubble area reduction observed in the off-center plane for the CtR array at the $x_{VG}/h = 4.5$ position (see Figure 10.1).

The primary distinction between the presented results of the CtR and the CoR vane arrays is the presence of an additional vane corresponding to the second pair in the spanwise direction. As evident from the vorticity and velocity fields, the presence of this vane, yields a region of negligible vorticity between actuators, where the downwash and upwash generated by both co-rotating vanes collide, resulting in an almost null wall-normal velocity region. Given the off-center recording plane is precisely located at this position between vane actuators, this behavior explains the inconsistency in the flow control capabilities along the span of the co-rotating vane setup, as depicted Figure 10.1.

Regarding the ramp concepts, despite their similarities, their shed vortex systems show very distinct behavior. The BR concept generates a pair of counter-rotating horseshoe vortices near the wall, following a topology similar to that of the counter-rotating array. However, in this case, the distance between vortex cores is significantly reduced compared to the CtR array due to the actuator geometry, resulting in reduced downwash and upwash regions, as

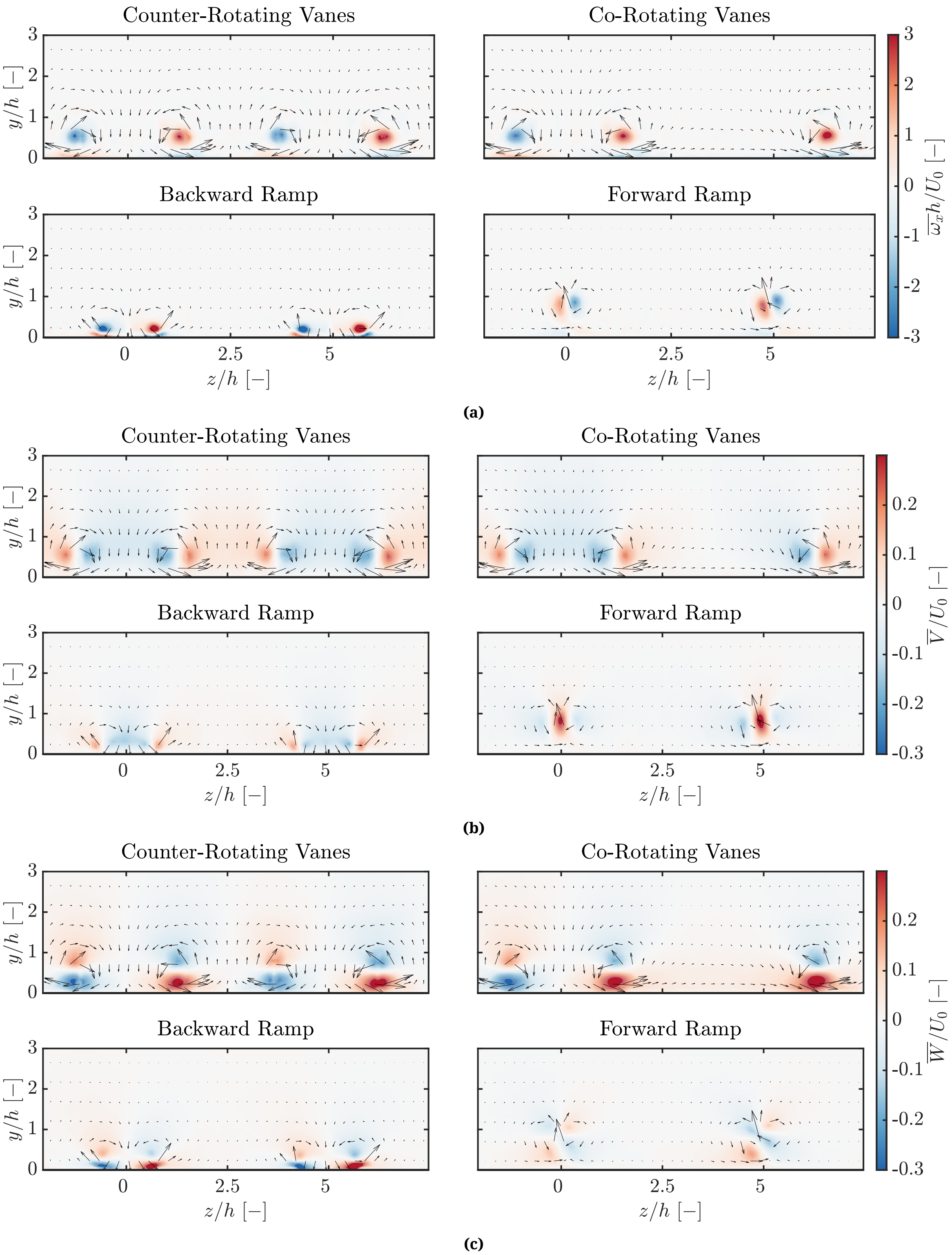

Figure 10.5: Contours with superposed velocity vector field of: (*a*) Mean flow streamwise vorticity $\overline{\omega_x}h/U_0$; (*b*) Mean flow wall-normal velocity $\overline{V}/U_0$; (*c*) Mean flow spanwise velocity $\overline{W}/U_0$ for all four actuators in $x_{VG}/h = 4.5$. Only one out of every 4 vectors in the z-direction and one in 8 vectors in the y-direction is shown for clarity.

indicated by the wall-normal velocity graph (see Figure 10.5). These results correlate with the findings obtained in the streamwise recording planes, explaining the difference in flow control capabilities between the center and off-center planes. However, the fact that this actuator concept achieves perfect flow control in both center and off-center planes when located only $x_{VG}/h = 4.5$ upstream of the ramp inception suggests that the benefits of the common downwash region may outweigh the detrimental effects of the common upwash region.

Finally, the forward-facing ramp configuration shows a system of counter-rotating vortices that collide at the trailing edge of the ramp. In this case, the total shed vorticity is notably smaller than that of other systems. The wall-normal and spanwise velocity fields indicate a very high wall-normal velocity corresponding to the ramp edge and very small spanwise velocities. These velocity distributions corroborate the results obtained in the streamwise recording planes. Notably, the fact that the forward ramp actuator triggers an increase in separation bubble area when located in the closest position to the ramp inception can be attributed to this peak in upwash in both the center and off-center planes. To exemplify these descriptions and just for enhanced clarity and visualization, the vortex systems described previously have been depicted in Figure 10.6 based on the results of the CFD simulations.

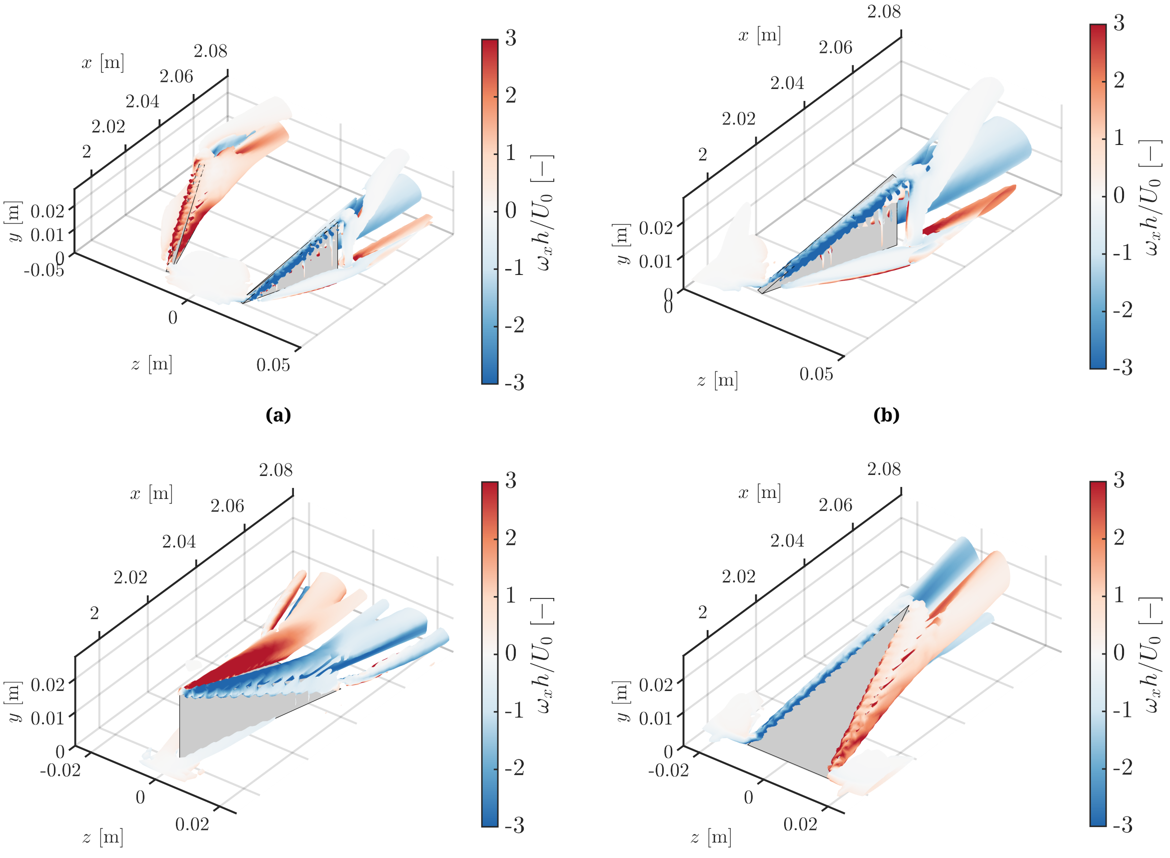

(a)

(b)

(c)

(d)

Figure 10.6: Iso-surfaces of $Q = 5000\ \mathrm{s}^{-2}$ colored by $\omega_x h/U_0$ according to CFD results. (*a*) Counter-rotating VG pair; (*b*) Single vane; (*c*) Backward ramp; (*d*) Forward ramp.

In addition to the qualitative description of the vortex systems, analyzing the vorticity fields along the crossflow planes facilitates the quantification of vortex circulation, denoted as Γ. The vortex circulation is calculated by integrating the streamwise vorticity over the area A

according to:

$$\Gamma = \iint_A \omega_x \, dA \tag{10.1}$$

where A is defined in this report as the area enclosed by the contour $|\omega_x| h/U_0 = 0.45$. Identifying each primary vortex using iso-vorticity contours enables the calculation of the vortex decay for each individual vortex, thereby facilitating a quantitative investigation of spanwise differences in evolution. Considering that, as evident in Figure 10.5, four primary vortices are clearly discernible for all VG designs (except CoR, which shows only three), for the remainder of this section, primary vortices will be denoted from 1 to 4 based on their spanwise position. Vortex 1 will refer to the first vortex in the $+z$ direction, while vortex 4 will designate the last.

Figure 10.7 presents the values of nondimensional circulation $\Gamma^* \equiv \Gamma/(hU_0)$ for each vortex alongside their respective average and standard deviation values for each of the VG designs.

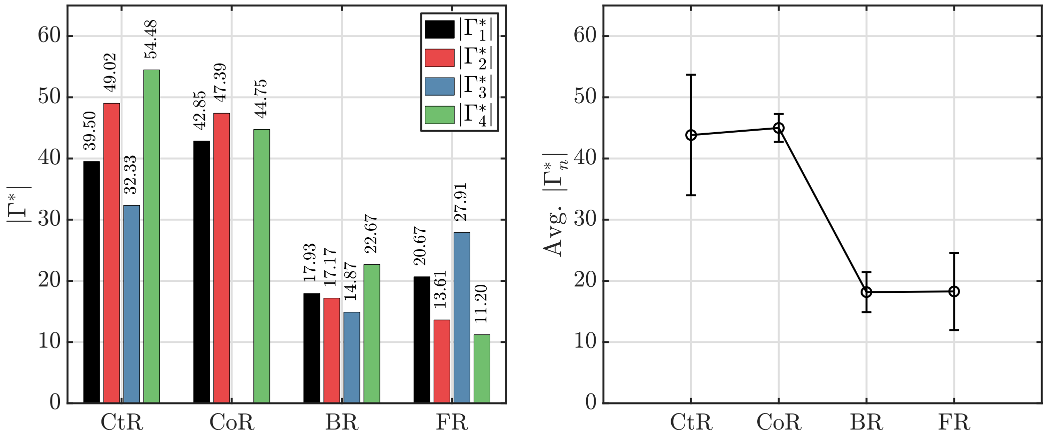

Figure 10.7: Nondimensional circulation $|\Gamma^*| \equiv |\Gamma|/(hU_0)$ for each vortex (*left*) alongside their respective average and standard deviation values (*right*) for each of the VG designs at $x_{VG}/h = 4.5$.

The circulation results corroborate the findings depicted in Figure 10.5: the circulation values for both vane concepts are more than double those of the ramp concepts. Moreover, the spanwise 3D effects are evident from the disparities in circulation values between vortex pairs. The CoR array demonstrates how the absence of one of the vanes significantly alters the spanwise evolution of circulation. In this case, the absence of the 3rd vortex leads to a slight decrease in the circulation of the 2nd and 4th vortices, while the circulation of the 1st vortex increases.

Interestingly, compared to the BR concept, where most vortices exhibit similar circulation magnitudes, the FR concept (despite being tested at $\beta = 0°$) shows a clear bias towards vortices with positive streamwise vorticity (1st and 3rd), as these consistently exhibit larger circulation magnitudes. Comparing these results with those from an additional scenario will facilitate the calculation of the vortex decay.

10.2.3. PIV measurements: $x_{VG}/h = 18$

In addition to the results recorded shortly downstream the actuators, it is interesting to observe the same features after a longer development distance in order to better quantify the streamwise evolution of the vortices. For this purpose, the recordings of the crossflow plane with the actuators further upstream at $x_{VG}/h = 18$, provide valuable insights. Figure 10.8

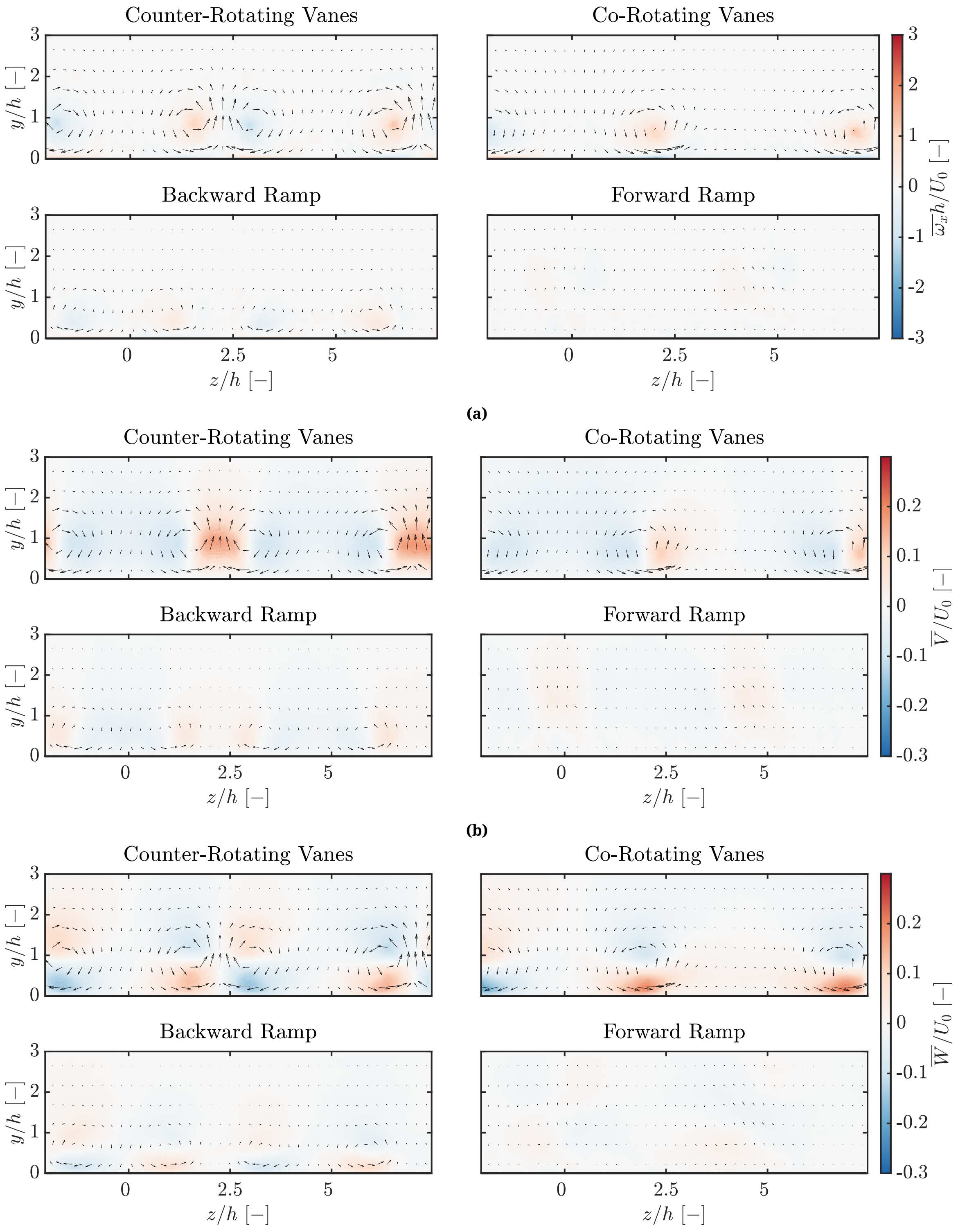

(a)

(b)

(c)

Figure 10.8: Contours with superposed velocity vector field of: (*a*) Mean flow streamwise vorticity $\overline{\omega_x}h/U_0$; (*b*) Mean flow wall-normal velocity $\overline{V}/U_0$; (*c*) Mean flow spanwise velocity $\overline{W}/U_0$ for all four actuators in $x_{VG}/h = 18$. Only one out of every 4 vectors in the z-direction and one in 8 vectors in the y-direction is shown for clarity.

presents vorticity and velocity contours of these results. Moreover, Figure 10.9 presents the values of nondimensional circulation for each vortex, along with their respective average and standard deviation values for each of the VG designs. It is essential to note, however, that at this position, the trajectory of vortex 1 leads part of its core out of the field of view of the PIV recording plane. Hence, the results depicted in this table for CtR and CoR may potentially underestimate the absolute value of the circulation corresponding to these vortices.

Upon initial inspection of the vorticity field, a significant decay in vorticity values is apparent for all the VG designs when compared to the results presented in Figure 10.5. However, although weaker, the structures in three out of the four vortex systems analyzed previously remain visible and consistent. In both the CtR and CoR array setups, the common downwash and upwash regions can still be distinguished. This consistency is confirmed by the streamwise measurements, where both achieve a perfect separation control (except for the CoR setup in the off-center plane which, as introduced previously, exhibits a significant performance drop). Furthermore, the circulation results support these findings: the circulation values for both vane concepts are approximately half of those observed at the previous VG position. These findings align with the theory presented in Ashill et al. (2001), suggesting that the vortices induced by single-rotation vanes decay downstream of the device in a manner similar to that of counter-rotating devices with spacing between the vortices.

The backward ramp concept experiences a critical decay in the vortex strength along the stream, since at this position, this concept exhibits nearly negligible circulation values in all of the studied vortices. Despite this, the velocity contours still show some regions of upwash and downwash, but these are insufficient to avoid the flow separation entirely. The proximity of the wall and the interaction between the vortex pair may contribute to the accelerated decay observed. The forward ramp configuration demonstrates no discernible signs of vorticity, indicating minimal impact from the VG actuation at this stage. This observation is again consistent with the results obtained from streamwise measurements.

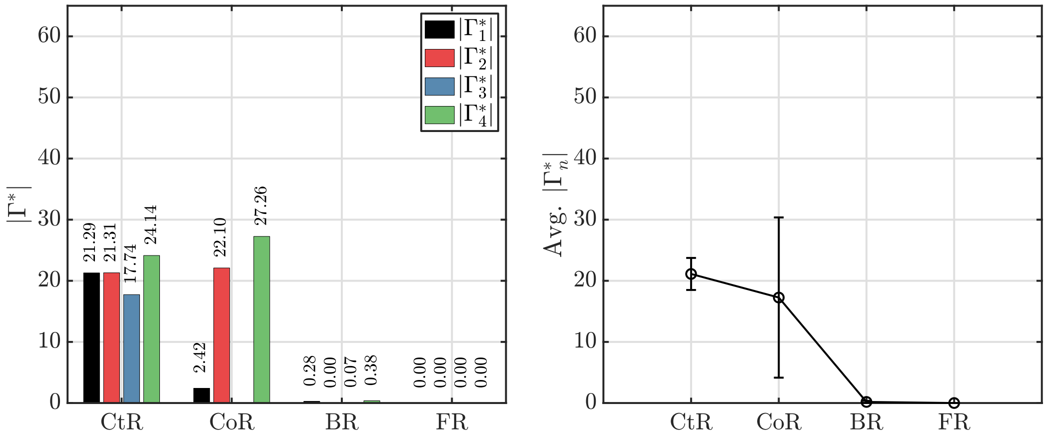

Figure 10.9: Nondimensional circulation $|\Gamma^*| \equiv |\Gamma|/(hU_0)$ for each vortex (*left*) alongside their respective average and standard deviation values (*right*) for each of the VG designs at $x_{VG}/h = 18$.

Based on the circulation values obtained for two different development lengths, a linear estimation of vortex decay along the stream can be computed. Figure 10.10 illustrates the nondimensional circulation values as a function of streamwise development length for all four VG designs, accompanied by a schematic contour plot displaying the color code assigned to each vortex. Table 10.2 provides the values of vortex decay, expressed as $d\Gamma^*/dx^*$, with $x^* \equiv x_{VG}/h$, along with their respective average and standard deviation values for each VG design.

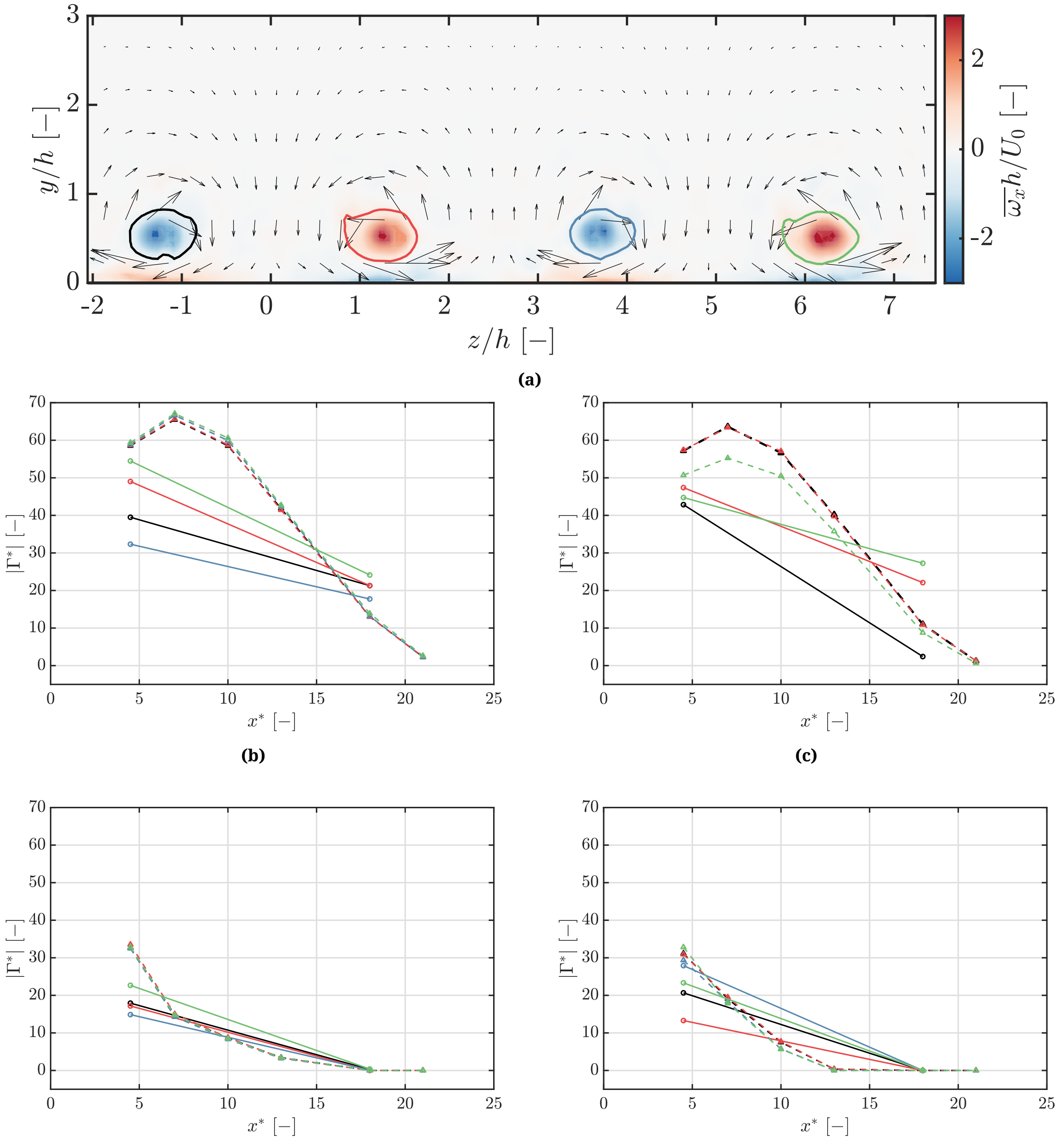

(a)

(b)

(c)

(d)

(e)

Figure 10.10: Circulation evolution as a function of the streamwise travel distance in PIV (——) and CFD (- - -) results: (*a*) Main vortex cores (CtR vane array at $x_{VG}/h = 4.5$); (*b*) Counter-rotating vane array; (*c*) Co-rotating vane array; (*d*) Backward ramp; (*e*) Forward ramp.

The plots illustrating the circulation evolution as a function of streamwise distance reveal a decreasing trend towards null circulation as the distance grows. As expected, the circulation of a vortex near a wall decreases as a consequence of the spanwise component of the wall shear stress which gives rise to a torque opposing the rotation of the vortex (Wendt et al. 1993). On average, excluding the biased values of CtR and CoR in vortex 1, all VGs experience decay of similar magnitude. These findings challenge the hypothesis proposed by Ashill et al. (2001), which suggests that the streamwise decay of vortex strength for counter-rotating vane devices spaced apart by at least one device height is an order of magnitude lower on

Table 10.2: Circulation decay $|d\Gamma^*/dx^*|$ for each of the captured vortices alongside their respective average and standard deviation values for each of the VG designs.

	$\left\lvert\frac{d\Gamma_1^*}{dx^*}\right\rvert$ [–]	$\left\lvert\frac{d\Gamma_2^*}{dx^*}\right\rvert$ [–]	$\left\lvert\frac{d\Gamma_3^*}{dx^*}\right\rvert$ [–]	$\left\lvert\frac{d\Gamma_4^*}{dx^*}\right\rvert$ [–]	Avg. $\left\lvert\frac{d\Gamma_n^*}{dx^*}\right\rvert$	Std. Dev. $\left\lvert\frac{d\Gamma_n^*}{dx^*}\right\rvert$
CtR	$1.35^\dagger$	2.05	1.08	2.25	$1.68^\dagger$	$0.56^\dagger$
CoR	$2.99^\dagger$	1.87	–	1.30	$2.03^\dagger$	$0.83^\dagger$
BR	1.31	1.27	1.10	1.65	1.33	0.23
FR	1.01	1.53	1.18	2.07	1.45	0.47

† Part of the vortex core is out of the PIV field of view.

a logarithmic basis than that of joined counter-rotating vanes and wedges. However, in this study, with a limited number of data points, vane VGs have simply demonstrated the ability to generate more circulation under the same conditions. Consequently, given a similar decay compared to ramp concepts, they generally perform better overall as they operate over longer downstream distances.

In particular, the CoR array provides an interesting scenario to quantify the effect of the missing vane over the rest of the array. Comparing the PIV measurements of both, CtR and CoR VGs, shows a noticeable change in the decay trend of vortex 4 (depicted in green). The evolution of the circulation shows how, instead of converging towards a single point of null circulation, like most of the vortices do in the rest of the scenarios, vortex 4 show remarkably different trends. On the one hand, it can be appreciated how the circulation at $x_{VG}/h = 4.5$ is significantly reduced compared to the analogous vortex in the CtR array. However, the absence of the 3rd primary vortex (blue) significantly decreases the decay rate of vortex 4, suggesting that this particular vortex may reach longer streamwise distances. This result corroborates the hypothesis that the interaction between counter-rotating vortices may enhance a quicker vortex strength decay.

In addition to the PIV results, the ZPG CFD circulation results have been calculated for multiple intermediate points to provide better context for the trends depicted. Consistent with the previous comparison between PIV and CFD measurements, the numerical results recorded $4.5h$ downstream of the actuators tend to over-predict vortex circulation compared to experimental results. However, for longer development lengths, the CFD results tend to under-predict circulation due to the increasing influence of secondary motions.

The trends observed in these results reveal several interesting findings. Both vane configurations exhibit a similar decay trend, where circulation increases up to measurement positions $7h$ downstream of the actuators. Beyond this point, vortex decay becomes more pronounced, leading to a progressive decrease in circulation until it reaches null circulation in measurements $21h$ downstream the actuator. Given that the CFD results tend to under-predict circulation for long development lengths, and considering the streamwise results of the controlled case, which demonstrate effective control capabilities even after $28h$, it is important to note the following: under the circulation criteria defined in this report (contour defined by $|\omega_x|h/U_0 = 0.45$), null circulation does not necessarily equate to null flow vorticity or poor flow control performance. This distinction highlights that effective flow control can still be achieved despite the apparent reduction in circulation.

From the low circulation values presented in Figure 10.9 for the vortices of the BR setup, it can be inferred that circulation almost completely decays after $18h$. Indeed, CFD results show that the decay trends for the ramp configurations are very similar to each other but differ notably from the vane concepts. In this case, the most drastic decrease in circulation occurs after small development distances, followed by a more linear progression. The BR ramp, in particular, shows very good agreement with the PIV results, accurately predicting the point of null circulation.

However, in this configuration, the FR setup exhibits null circulation for all four vortices, implying the possibility of earlier circulation decay. CFD results indicate that the point of null circulation may occur well before $18h$ downstream of the actuator, as predicted. Thus, the vortex decay presented in Table 10.2 may overestimate the real value.

10.2.4. Vortex core trajectories

To better characterize the streamwise evolution of the vortex systems, comparing the vortex trajectories between the different systems is very insightful. Figure 10.11 represents superposed $|\omega_x|$ iso-contours for all four actuators setups, for different original actuator positions, along with the determined vortex center according to the described rationale. For improved visibility, Figure 10.11a represents the $|\omega_x|h/U_0 = 0.90$ iso-contours, whereas Figure 10.11b depicts the $|\omega_x|h/U_0 = 0.34$ contour.

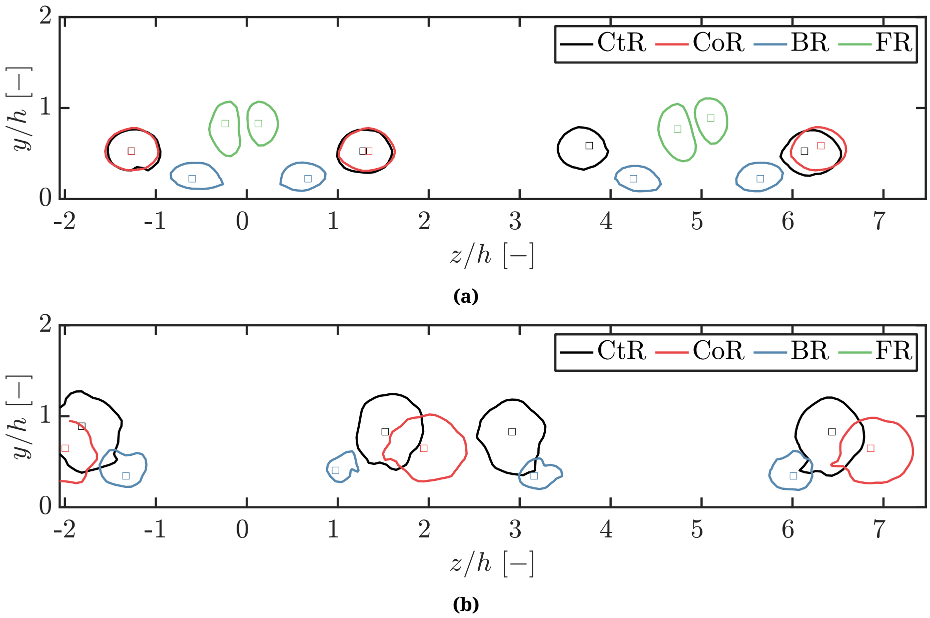

(a)

(b)

Figure 10.11: Contours of: (*a*) $|\omega_x|h/U_0 = 0.90$ for $x_{VG}/h = 4.5$; (*b*) $|\omega_x|h/U_0 = 0.34$ for $x_{VG}/h = 18$. Point of maximum absolute streamwise vorticity $|\omega_x|_{max}$ represented by □.

Figure 10.11a clearly illustrates the vortex system topologies described in Section 10.2.2. As expected, the CtR and CoR configurations show very similar topologies in the central plane pair (since the actuators in this region are effectively identical copies), but exhibit slight differences in the vortex center position of the vortex located further in spanwise direction. This discrepancy can be attributed to the effect of the missing neighboring vane. Regarding the ramps, both display similar copies in both of the recorded actuators.

Examining the vortex evolution as the VG arrays are moved upstream reveals more significant differences between the two vane configurations. As shown in Figure 10.11b, the displacement of their vortex cores differs notably with a longer development length. According to Pauley and Eaton (1988), a vortex pair with common downwash tends to move apart as it develops, producing an ever-widening region of boundary-layer thinning. This diverging motion can be explained using inviscid flow theory, particularly the vortex image method. The influence of the wall on the vortex can be mathematically represented through a mirror-image vortex situated beneath the ground wall, inducing circulation with opposite sign. Employing the principles of the Biot-Savart law simplifies the determination of the velocity induced by the mirror-image vortex onto the real vortex. Alternatively, a qualitative understanding can be employed. It becomes evident that the induced velocity from the mirror vortex acts in a lateral direction (depending on the circulation), thereby prompting a corresponding spanwise movement of the actual vortex. This theory is schematically depicted in Figure 10.12.

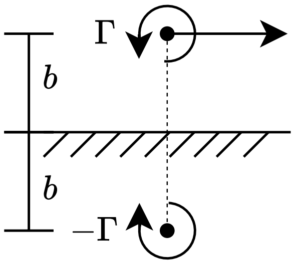

Figure 10.12: Method of images: vortex near a wall.

In the case of an array of vortices, originally the induced velocity by the adjacent real vortex leads to a stronger induced force away from each other due to the mirrored vortices at the plate, however, when two vortices move away from each other, they inevitably move closer to the vortex from the neighboring pair. Consequently, a new counter-rotating pair with common upwash is formed. The induced velocities in the new pair tend to lift the vortices, causing them to rise from the wall, as described by Jones (1957). In the CoR configuration, where one vane is missing compared to the CtR system, the blockage, as well as the induced velocity field, created by that vortex disappears, causing the other vortices to move apart quicker. This results in the vortex system covering a larger span, as seen in Figure 10.11b.

Finally, it is important to remember that the presented measurements are taken in adverse pressure gradient conditions. Hence, according to Ashill et al. (2002), under adverse pressure gradient there is an increased tendency for vortices to merge and consequently to decay more rapidly. According to further studies (see Ashill et al. 2005) increasing the spacing between the vanes reduces this adverse tendency. Hence, under ZPG conditions, it can be assumed that the vortex system generated by these actuators (at least the CtR, CoR, and BR) can perform comfortably at more than $18h$ upstream of the separation point.

11

Proposed design

Based on the results obtained from the study of various actuator systems, a comprehensive understanding of their performance and feasibility emerges. The investigation into the diverse VG concepts reveals several key features that inform its suitability for practical application and are discussed in this chapter. In the particular case of the forward ramp, the formation of closely spaced vortices at the wall-normal position of the ramp trailing edge was observed, accompanied by a propensity for vortex merging due to their close proximity. This phenomenon, together with the significant sensitivity of vortex strength to adverse pressure gradient, led to a rapid decay of the vortex system, mainly due to the APG effect of limiting the device's effective height. Notably, the forward ramp exhibited very limited effectiveness in flow control compared to its backward-facing counterpart, with positive results observed only within a specific region of the separation bubble area. Despite expectations of downforce generation, according to the CFD results the observed effects were not excessively large within the range of β angles investigated. When considering a more feasible design, the hollow forward ramp, implementation challenges further compounded the unsuitability of the forward ramp concept, particularly due to the substantial increase in normal load resulting from changes in pressure distribution. Consequently, based on these findings, the forward ramp concept is deemed unsuitable for further consideration.

Similarly, the examination of the backward ramp concept presented its characteristics and potential limitations. The formation of horseshoe-shaped vortices shedding from the ramp's lateral edges was noted, with vortices spaced at a distance proportional to the ramp width. Over the streamwise distance, vortices tend to laterally separate, leading to increased coverage. However, vortex strength is significantly affected by APG. While effective flow control was demonstrated within a limited streamwise region, namely only the position closest to the separation point, susceptibility to strong vortex decay and increased normal load presented significant challenges for practical implementation. Modifications such as a hollow ramp showed promise in enhancing vorticity shedding, suggesting avenues for further exploration. However, the overarching conclusion based on the observed characteristics is the rejection of the backward ramp concept for practical application.

Moving on to the co-rotating vane array concept, distinct features emerged from its investigation. The formation of a main vortex shedding from the wingtip edge, along with lateral separation of vortices over the streamwise distance, demonstrated effectiveness in flow control, particularly within the specific spanwise regions downstream the actuator. However, the poor flow control efficacy far from the actuator spanwise region, along with challenges related to implementation, such as the significant side load at high skew angles, and the need for further investigation into performance optimization, led to the rejection of the co-rotating vane array concept.

Lastly, the examination of counter-rotating vanes provided insights into its performance and feasibility. The formation of counter-rotating vortices from each pair of actuators shedding from the wingtip edges showed promising results, with almost perfect flow control observed for all studied scenarios over the curved backward-facing ramp. Despite challenges related to implementation, even with a curved ramp shape, the strong potential exhibited by the counter-rotating vane concept suggests avenues for further exploration and optimization.

The findings from the study highlight the complexity of actuator systems for flow control applications. While certain concepts exhibited promising performance characteristics, challenges related to performance optimization and practical feasibility necessitate careful consideration and further research. Overall the key features of each design (summarised in Table 11.1) show the counter-rotating vane array's superior performance under the tested conditions. These results look promising since they show agreement with several previous vane optimization studies such as Lin (2002) and Godard and Stanislas (2006), to name a few. However, the considerable side load and the yaw moments experienced by these devices, particularly as the skew angle increases, present a notable limitation for their deployment as vortex generators. This limitation becomes especially pronounced when considering materials like fiber-reinforced polymer and shape memory alloys, which may struggle to withstand additional stress over the hinge region necessary for optimal deployment.

Addressing this challenge requires a shift in perspective and approach. Rather than focusing solely on deploying and stowing the vortex, an alternative strategy proposes a fundamental redesign. As demonstrated in the study, the axial load of vane-type VGs is generally low due to their minimal frontal area. Consequently, it is reasonable to assume that at a neutral angle of attack ($\beta = 0°$), the effects of these actuators could be negligible. The innovative aspect lies in maintaining the vane deployed while dynamically adjusting the skew angle as needed.

Instead of relying on complex deployment and stowage mechanisms, this design maintains the vane in a deployed state while dynamically adjusting the skew angle to meet varying flow conditions. This method employs rigid materials for the vane structure, ensuring durability, and utilizes shape-memory alloys to facilitate precise rotation of the vanes to the desired inflow angle.

The dynamic adjustment of the skew angle provides significant operational flexibility. During periods requiring flow control, shape-memory actuation adjusts the vanes to the optimal position, enhancing effectiveness. Conversely, when the demand for flow control is minimal, the vanes can return to a neutral position ($\beta = 0°$), thereby mitigating side load issues and enhancing overall system robustness and operability.

This innovative approach offers several performance benefits. It enhances flow control effectiveness without the susceptibility to adverse pressure gradient effects observed in traditional VG designs. By simplifying the actuator mechanism, it reduces implementation challenges and increases the potential for practical application across a range of operating conditions. Thus, the proposed design provides a robust and adaptable solution for effective flow control, addressing the limitations identified in traditional VG actuators.

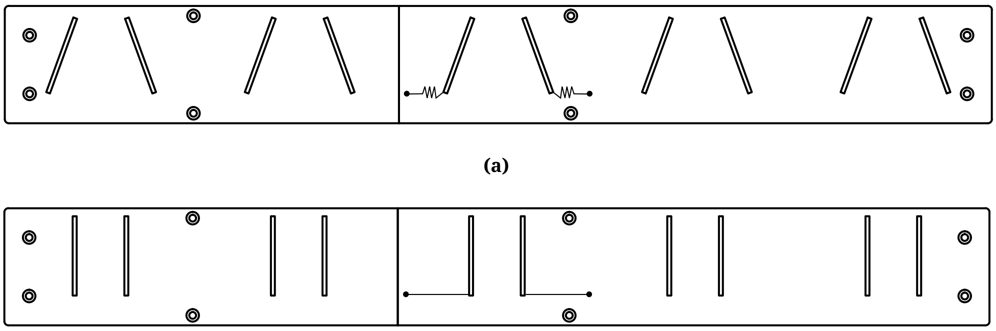

(a)

(b)

Figure 11.1: Schematic of proposed design of a counter-rotating actuator array: (*a*) Under actuation ($\beta = 20$ deg.); (*b*) Not actuated ($\beta = 0$ deg.).

Table 11.1: Summary of key features of each VG concept.

VG concept	Key Features
Forward Ramp	• Formation of closely spaced vortices at the ramp trailing edge. • Proneness to vortex merging and rapid decay due to close proximity. • Sensitivity of vortex strength to adverse pressure gradient (APG), reducing effective height. • Very limited flow control efficacy. • Generates negative wall-normal load, but not excessive. • Implementation challenges due to increased normal load. • Unsuitable for further consideration.
Backward Ramp	• Formation of horseshoe-shaped vortices shedding from the ramp's lateral edges. • Vortices spaced proportional to ramp width. • Effective flow control only in limited region, susceptible to decay. • Significant normal load generation. • Implementation challenges due to increased normal load. • Hollow ramp modification shows increased max. vorticity, potential interest in rigid version. • Rejected for further consideration.
Co-rotating Vanes	• Formation of main vortex shedding from wingtip edge. • Proneness to vortex lateral separation, leading to increased coverage. • Inconsistent flow control efficacy. • Potential enhancement with decreased vane spacing, but risks vortex merging. • Implementation challenges with curved ramp shape. • Rejected for further consideration.
Counter-rotating Vanes	• Formation of counter-rotating vortices from wingtip edges. • Proneness to vortex lateral separation (smaller than CoR vanes), leading to increased coverage. • Very consistent and effective flow control results. • Suggesting potential flow control efficacy even at larger distances upstream of the separation point. • Challenges in implementation with curved ramp shape due to increased side load. • Best option (in agreement with literature).

Part IV

Closure

12

Conclusions

This research project has successfully designed and tested experimentally four distinct VG actuator arrays tailored specifically for the control of turbulent separation bubbles along a curved backward-facing ramp. This research aimed to advance in the understanding of flow control mechanisms and their applicability in mitigating separation. In particular, it focused on investigating the aerodynamic features of adaptive vortex generators employing shape memory alloys, with the goal of identifying the optimal aerodynamic configuration. The conclusions drawn from the results discussed in the preceding chapters are summarized here.

On the research methodologies

The experimental methodology employed planar Particle Image Velocimetry (2D2C) to acquire the requisite data. Four distinct recording planes around the backward-facing ramp were utilized, facilitating a comprehensive analysis of three-dimensional flow field dynamics. This experimental methodology was vital in understanding the complexities of separation control around the ramp. PIV proved indispensable in providing a visual representation of flow patterns and in quantifying the effectiveness of VG actuator arrays in modulating flow behavior.

In parallel, numerical simulations using Computational Fluid Dynamics were also conducted as a complementary tool, offering insights into flow phenomena beyond the scope of experimental validation. Despite inherent limitations associated with the RANS approach, the numerical method yielded robust preliminary findings that aligned with predictions from prior investigations and increased confidence in the numerical study of VG actuator arrays. The outcomes demonstrated a notable correlation with the experimental results, and validated the hypothesis posed by Spalart et al. (2015), claiming that RANS simulations can accurately capture the evolution of streamwise vortices generated by VGs over a flat surface. Collectively, the experimental and numerical methodologies constituted a comprehensive framework for investigation, combining empirical validation with theoretical insights to advance the frontier of flow control research.

On the effect of vortex generators in preventing flow separation over a backward-facing ramp

The skew angle sensitivity analysis via a CFD study revealed critical insights into VG actuator array performance. Despite variations in aerodynamic loads, all VG designs demonstrated robustness against axial loads, with the vane design showing promise due to reduced sensitivity to inflow angles. However, challenges arise from normal and side loads, particularly concerning actuation mechanism durability, especially in configurations like the hollow ramp. This underscores the need for robust actuation mechanisms capable of withstanding operational cycles. In summary, the sweep angle study highlights both the potential and challenges of VG designs, requiring future optimization efforts.

The experimental analysis of the uncontrolled flow dynamics revealed several key observations about the complex nature of turbulent separation phenomena along the curved backward-facing ramp. The limited aspect ratio of the separation ramp resulted in a relatively three-dimensional flow regime, complicating the dynamics of separation bubbles. The separation bubble exhibited its largest area along the plane of symmetry of the test section, emphasizing the role of geometric constraints in shaping flow behavior. Moreover, the smooth curvature of the ramp contributed to the intermittent nature of the separation phenomenon, which manifested intermittently along a wide region, showcasing the dynamic nature of flow behavior.

The analysis of controlled flow dynamics and VG design revealed distinct characteristics and performance outcomes for various configurations. Counter-rotating vanes emerged as the most promising option, characterized by the formation of counter-rotating vortices from the wingtip edges. This configuration demonstrated very consistent and effective flow control results, suggesting potential efficacy even at larger distances upstream of the separation point. However, challenges in implementation were noted due to side loads, notwithstanding its status as the overall best option among the configurations examined.

Contrarily, co-rotating vanes exhibited a different behavior. Although promising outcomes were observed in very specific conditions, notable declines in flow control effectiveness appeared across the span in alternate scenarios, highlighting the need for further setup optimization. Potential enhancements with decreased vane spacing were identified, albeit with associated risks of vortex merging. Challenges in implementation also arose due to side loads.

The backward ramp configuration, characterized by the formation of horseshoe-shaped vortices shedding from the ramp's lateral edges, showcased effective flow control only within a limited streamwise region very close to the separation point. The generated vortices were susceptible to the APG and tended to decay over the stream. Implementation challenges primarily stemmed from normal load considerations. In contrast, the forward ramp design exhibited even less favorable outcomes, with closely spaced vortices forming at the ramp's trailing edge. Proneness to vortex merging and rapid decay due to close proximity rendered this configuration very ineffective, potentially even triggering separation. Implementation challenges, akin to the backward ramp, were primarily attributed to normal load considerations.

On the optimal aerodynamic configuration for a deployable vortex generator based on shape memory alloy actuation

The analysis of controlled flow dynamics and VG design underscores the diverse performance outcomes and implementation challenges associated with various configurations. While counter-rotating vane arrays emerge as the most promising option, each configuration presents unique opportunities and considerations for further optimization and practical implementation in flow control applications.

Given the limitations inherent in deployable VG configurations utilizing Shape Memory Alloy actuation, a novel design approach is proposed to address the challenges posed by traditional VG configurations. The proposed solution entails maintaining the vane deployed while dynamically adjusting the skew angle as necessitated by varying flow conditions. Unlike VG designs reliant on complex deployment and stowage mechanisms, the proposed design adopts a pragmatic approach by utilizing a rigid vane actuator constructed from durable materials. In this case, shape memory alloys are strategically employed to facilitate precise rotation of the vanes to the desired inflow angle, thereby offering enhanced adaptability and control over flow dynamics.

A key advantage of the proposed design lies in its ability to mitigate side load issues, a common challenge encountered in traditional VG configurations. During periods of minimal or no flow control demand, the vanes can be returned to a neutral position ($\beta = 0$ degrees), effectively reducing side load impacts and enhancing overall system robustness and operability.

By avoiding the material complexities associated with deployable VG configurations, the proposed design offers a streamlined yet effective solution for flow control applications. Its flexibility, precision, and operational efficiency position it as a promising avenue for future research and practical implementation in aerodynamic control systems.

13

Recommendations for future work

The study has yielded several conclusions, yet it also left some questions unanswered and raised new ones. This section presents recommendations for future work, aiming to enhance the understanding of separation control and improve the effectiveness of VG designs.

Validation of SMA-actuated devices
The experimental campaign presented in this research was conducted using a rigid version of the various proposed VG concepts due to project time limitations. A logical next step would be to validate the results of these tests using devices manufactured using the previously mentioned SMA actuation mechanisms. This could validate or refute the project's hypothesis regarding the viability and performance of this innovative approach, providing valuable insights into its practical feasibility and effectiveness in turbulent flow control applications.

Experimental testing of conceptual design
Another promising avenue consists in testing the proposed alternative design, which still remains conceptual. Validating the performance of this concept in an experimental test is crucial to assess its effectiveness in mitigating turbulent separation phenomena and its practical use in aerodynamic control systems.

High-fidelity CFD studies
Conducting a high-fidelity computational fluid dynamics study of the complete ramp geometry, designed to replicate the adverse pressure gradient encountered in the test section, could reveal further complexities of flow behavior and VG performance. However, as discussed in this report, Reynolds-Averaged Navier-Stokes simulations face significant limitations in accurately capturing highly separated turbulent flows. To overcome these constraints, a Large Eddy Simulation approach might prove advantageous despite the higher computational expense and time-consuming setup. Such simulations could provide a reliable approximation of outcomes associated with multiple VG configurations at a relatively low cost.

Fluid-structure interaction simulations
Integrating a numerical methodology that incorporates the mechanical attributes of SMA-actuated VGs, such as a fluid-structure interaction simulation, also holds promise in advanc-

ing this research. This approach could reveal additional constraints inherent in deployable VG concepts. Leveraging advanced numerical simulations can yield profound insights into flow dynamics while facilitating the optimization of VG configurations. Notably, these endeavors typically entail lower costs compared to experimental simulations.

Methodological refinements in experimental setups
For analogous experiments conducted within the same facility, methodological refinements such as augmenting the span or aspect ratio of the separation ramp hold potential benefits. This adjustment could mitigate the three-dimensionality of the flow, thereby diminishing uncertainties in the streamwise measurements. Additionally, the incorporation of an additional recording plane parallel to the slope of the ramp could provide insights into the streamwise evolution of the induced perturbation, thereby enriching comprehension of the separation phenomenon.

The recommendations outlined above underscore the multifaceted nature of ongoing research into VG designs for turbulent flow control. By validating innovative concepts through SMA-actuated devices, exploring high-fidelity CFD and fluid-structure interaction simulations, and refining experimental methodologies, future work can significantly advance our understanding and practical application of VG technology. Such efforts will not only address the limitations identified in this study but also pave the way for more effective and efficient aerodynamic control systems.

References

Aider, J.-L., J.-F. Beaudoin, and J. E. Wesfreid (2010). “Drag and lift reduction of a 3D bluff-body using active vortex generators”. In: *Experiments in Fluids* 48.5, pp. 771–789.

Ashill, P., J. Fulker, and K. Hackett (2001). “Research at DERA on sub boundary layer vortex generators (SBVGs)”. In: *39th Aerospace Sciences Meeting and Exhibit*. Aerospace Sciences Meetings. American Institute of Aeronautics and Astronautics.

– (2002). “Studies of flows induced by Sub Boundary Layer Vortex Generators (SBVGs)”. In: *40th AIAA Aerospace Sciences Meeting & Exhibit*. Aerospace Sciences Meetings. American Institute of Aeronautics and Astronautics.

Ashill, P. R., J. L. Fulker, and K. C. Hackett (2005). “A review of recent developments in flow control”. In: *The Aeronautical Journal* 109.1095, pp. 205–232.

Baldacchino, D. (2019). “Vortex Generators for Flow Separation Control: Wind Turbine Applications”. PhD thesis. Delft University of Technology.

Barrett, R. and S. Farokhi (1996). “Subsonic aerodynamics and performance of a smart vortex generator system”. In: *Journal of Aircraft* 33.2, pp. 393–398.

Barth, T., P. Scholz, and P. Weirach (2011). “Flow Control by Dynamic Vane Vortex Generators Based on Piezoceramic Actuators”. In: *AIAA Journal* 49.5, pp. 921–931.

Baskaran, V., A. J. Smits, and P. N. Joubert (1987). “A turbulent flow over a curved hill Part 1. Growth of an internal boundary layer”. In: *Journal of Fluid Mechanics* 182, pp. 47–83.

Bender, E., B. Anderson, and P. Yagle (1999). “Vortex generator modeling for Navier-Stokes codes”. In: *Proceedings of the 1999 3rd ASME/JSME Joint Fluids Engineering Conference*.

Budanko, T. (2023). “Pulsed jet arrays for turbulent separation control (MSc Thesis)”. In: *TU Delft*.

Buice, C. and J. Eaton (2000). “Experimental Investigation of Flow Through an Asymmetric Plane Diffuser”. In: *Journal of Fluids Engineering-transactions of The Asme - J FLUID ENG* 122.

Bush, R. H., T. S. Chyczewski, K. Duraisamy, B. Eisfeld, C. L. Rumsey, and B. R. Smith (2019). “Recommendations for Future Efforts in RANS Modeling and Simulation”. In: *AIAA Scitech 2019 Forum*. AIAA Scitech 2019 Forum. San Diego, California: American Institute of Aeronautics and Astronautics.

Cathalifaud, P., G. Godard, C. Braud, and M. Stanislas (2009). “The flow structure behind vortex generators embedded in a decelerating turbulent boundary layer”. In: *Journal of Turbulence* 10, N42.

Chou, F.-K. and V. A. Sandborn (1973). “Prediction of the turbulent boundary layer separation”. In.

Clauser, F. H. (1954). “Turbulent Boundary Layers in Adverse Pressure Gradients”. In: *Journal of the Aeronautical Sciences* 21.2, pp. 91–108.

– (1956). “The Turbulent Boundary Layer”. In: *Advances in Applied Mechanics*. Ed. by H. L. Dryden and T. von Kármán. Vol. 4. Elsevier, pp. 1–51.

Coles, D. (1956). “The law of the wake in the turbulent boundary layer”. In: *Journal of Fluid Mechanics* 1.2, pp. 191–226.

Dacome, G. and W. J. Baars (2023). *Private communication*. E-mail.

Debien, A., S. Aubrun, N. Mazellier, and A. Kourta (2015). “ACTIVE SEPARATION CONTROL PROCESS OVER A SHARP EDGE RAMP”. In: *Proceeding of Ninth International Symposium on Turbulence and Shear Flow Phenomena*. Ninth International Symposium on Turbulence and Shear Flow Phenomena. University of Melbourne, Australia: Begellhouse, pp. 341–346.

Deck, S. (2012). “Recent improvements in the Zonal Detached Eddy Simulation (ZDES) formulation”. In: *Theoretical and Computational Fluid Dynamics* 26.6, pp. 523–550.

Deutsch, S. and W. C. Zierke (1986). *The measurement of boundary layers on a compressor blade in cascade at high positive incidence angle. 2: Data report*. NASA-CR-179492.

Dovgal, A. V., V. V. Kozlov, and A. Michalke (1994). “Laminar boundary layer separation: Instability and associated phenomena”. In: *Progress in Aerospace Sciences* 30.1, pp. 61–94.

Drela, M. (2014). *Flight vehicle aerodynamics*. Cambridge, Mass.: MIT Press. 279 pp.

Driver, D. M., H. L. Seegmiller, and J. G. Marvin (1987). “Time-dependent behavior of a reattaching shear layer”. In: *AIAA Journal* 25.7, pp. 914–919.

Eroglu, A. and R. E. Breidenthal (2001). “Structure, Penetration, and Mixing of Pulsed Jets in Crossflow”. In: *AIAA Journal* 39.3, pp. 417–423.

Fernández-Gámiz, U., P.-E. Réthoré, N. N. Sørensen, C. M. Velte, F. Zahle, and E. Egusquiza (2012). “Comparison of four different models of vortex generators”. In: *Proceedings of EWEA 2012 - European Wind Energy Conference & Exhibition*.

Fernández-Gámiz, U., C. M. Velte, P.-E. Réthoré, N. N. Sørensen, and E. Egusquiza (2016). “Testing of self-similarity and helical symmetry in vortex generator flow simulations”. In: *Wind Energy* 19.6, pp. 1043–1052.

Florentie, L., S. J. Hulshoff, and A. H. Van Zuijlen (2018). “Adjoint-based optimization of a source-term representation of vortex generators”. In: *Computers & Fluids* 162, pp. 139–151.

Gad-el-Hak, M. and D. M. Bushnell (1991). “Separation Control: Review”. In: *Journal of Fluids Engineering* 113.1, pp. 5–30.

Gardarin, B. and L. Jacquin (2009). “ON THE PHYSICS OF VORTEX GENERATORS FOR FLOW SEPARATION CONTROL”. In.

Glezer, A. and M. Amitay (2002). “Synthetic Jets”. In: *Annual Review Fluid Mechanics* 34, pp. 503–529.

Godard, G. and M. Stanislas (2006). “Control of a decelerating boundary layer. Part 1: Optimization of passive vortex generators”. In: *Aerospace Science and Technology* 10.3, pp. 181–191.

Gould, D. G. (1956). *The use of vortex generators to delay boundary layer separation: theoretical discussion supported by tests on a CF-100 aircraft*. National Research Council of Canada. Division of Mechanical Engineering. National Aeronautical Establishment.

Gray, P. D., M. T. Lakebrink, F. O. Thomas, T. C. Corke, I. Gluzman, and J. Straccia (2023). “Experimental and Computational Evaluation of Smooth-Body Separated Flow over Boeing Bump”. In: *AIAA AVIATION 2023 Forum*. AIAA AVIATION Forum. American Institute of Aeronautics and Astronautics.

Herbst, A. H., P. Schlatter, and D. S. Henningson (2007). “Simulations of Turbulent Flow in a Plane Asymmetric Diffuser”. In: *Flow, Turbulence and Combustion* 79.3, pp. 275–306.

Ikeda, T., S. Masuda, T. Miyasaka, and T. Ueda (2006). “SMART VORTEX GENERATOR USING SHAPE MEMORY ALLOY”. In.

Jeong, J. and F. Hussain (1995). “On the identification of a vortex”. In: *Journal of Fluid Mechanics* 285, pp. 69–94.

Jirasek, A. (2005). “Vortex-Generator Model and Its Application to Flow Control”. In: *Journal of Aircraft* 42.6, pp. 1486–1491.

Jones, P. (1957). *The Calculation of the Paths of Vortices from a System of Vortex Generators, and a Comparison with Experiment*. Aeronautical Research Council.

Kaltenbach, H.-J., M. Fatica, R. Mittal, T. S. Lund, and P. Moin (1999). “Study of flow in a planar asymmetric diffuser using large-eddy simulation”. In: *Journal of Fluid Mechanics* 390, pp. 151–185.

Kleissl, K. (2013). “Cable Aerodynamic Control”. PhD thesis. Technical University of Denmark.

Koklu, M. (2018). “Effects of Sweeping Jet Actuator Parameters on Flow Separation Control”. In: *AIAA Journal* 56.1, pp. 100–110.

Kostas, J., J. M. Foucaut, and M. Stanislas (2007). “The Flow Structure Produced by Pulsed-jet Vortex Generators in a Turbulent Boundary Layer in an Adverse Pressure Gradient”. In: *Flow, Turbulence and Combustion* 78.3, pp. 331–363.

Lachmann, G. V., ed. (1961). *Boundary Layer and Flow Control: Its Principles and Application*.

Le, H., P. Moin, and J. Kim (1997). “Direct numerical simulation of turbulent flow over a backward-facing step”. In: *Journal of Fluid Mechanics* 330, pp. 349–374.

Le Pape, A., M. Costes, F. Richez, G. Joubert, F. David, and J.-M. Deluc (2012). “Dynamic Stall Control Using Deployable Leading-Edge Vortex Generators”. In: *AIAA Journal* 50.10, pp. 2135–2145.

Lee, J.-H., Y. S. Chung, and H. Rodrigue (2019). “Long Shape Memory Alloy Tendon-based Soft Robotic Actuators and Implementation as a Soft Gripper”. In: *Scientific Reports* 9.1, p. 11251.

Lelieveld, C., K. Jansen, and P. Teuffel (2016). “Mechanical characterization of a shape morphing smart composite with embedded shape memory alloys in a shape memory polymer matrix”. In: *Journal of Intelligent Material Systems and Structures* 27.15, pp. 2038–2048.

Lengani, D., D. Simoni, M. Ubaldi, P. Zunino, and F. Bertini (2011). “Turbulent boundary layer separation control and loss evaluation of low profile vortex generators”. In: *Experimental Thermal and Fluid Science* 35.8, pp. 1505–1513.

Lin, J. C. (2002). “Review of research on low-profile vortex generators to control boundary-layer separation”. In: *Progress in Aerospace Sciences* 38.4, pp. 389–420.

– (1992). “Control of Low-Speed Turbulent Separated Flow Over a Backward-Facing Ramp”. PhD thesis. Old Dominion University Libraries.

Lögdberg, O., K. Angele, and P. H. Alfredsson (2010). “On the robustness of separation control by streamwise vortices”. In: *European Journal of Mechanics - B/Fluids* 29.1, pp. 9–17.

Lögdberg, O., J. H. M. Fransson, and P. H. Alfredsson (2009). “Streamwise evolution of longitudinal vortices in a turbulent boundary layer”. In: *Journal of Fluid Mechanics* 623, pp. 27–58.

Manolesos, M., G. Papadakis, and S. Voutsinas (2020). “Revisiting the assumptions and implementation details of the BAY model for vortex generator flows”. In: *Renewable Energy* 146, pp. 1249–1261.

Manolesos, M., N. N. Sørensen, N. Troldborg, L. Florentie, G. Papadakis, and S. Voutsinas (2016). “Computing the flow past Vortex Generators: Comparison between RANS Simulations and Experiments”. In: *Journal of Physics: Conference Series* 753.2, p. 022014.

May, N. (2001). “A new vortex generator model for use in complex configuration CFD solvers”. In: *19th AIAA Applied Aerodynamics Conference*. 19th AIAA Applied Aerodynamics Conference. Anaheim,CA,U.S.A.: American Institute of Aeronautics and Astronautics.

Menter, F. R. (1994). “Two-equation eddy-viscosity turbulence models for engineering applications”. In: *AIAA Journal* 32.8, pp. 1598–1605.

Monty, J. P., E. Dogan, R. Hanson, A. J. Scardino, B. Ganapathisubramani, and N. Hutchins (2016). “An assessment of the ship drag penalty arising from light calcareous tubeworm fouling”. In: *Biofouling* 32.4, pp. 451–464.

Nikolaou, I. G., E. S. Politis, and P. K. Chaviaropoulos (2005). “Modelling the Flow Around Airfoils Equipped with Vortex Generators Using a Modified 2D Navier–Stokes Solver”. In: *Journal of Solar Energy Engineering* 127.2, pp. 223–233.

Nissle, S., M. Kaiser, M. Hübler, M. Gurka, and U. Breuer (2018). “Adaptive vortex generators based on active hybrid composites: from idea to flight test”. In: *CEAS Aeronautical Journal* 9.4, pp. 661–670.

Ohlsson, J., P. Schlatter, P. F. Fischer, and D. S. Henningson (2010). “Direct numerical simulation of separated flow in a three-dimensional diffuser”. In: *Journal of Fluid Mechanics* 650, pp. 307–318.

Ortmanns, J., M. Bitter, and C. J. Kähler (2008). “Dynamic vortex structures for flow-control applications”. In: *Experiments in Fluids* 44.3, pp. 397–408.

Pauley, W. R. and J. K. Eaton (1988). “Experimental study of the development of longitudinal vortex pairs embedded in a turbulent boundary layer”. In: *AIAA Journal* 26.7, pp. 816–823.

Pearcey, H. H. (1961). “Introduction to shock-induced separation and its prevention by design and boundary layer control”. In: *Boundary Layer and Flow Control*. Ed. by G. V. Lachmann. Pergamon, pp. 1166–1344.

Prandtl, L. (1933). “Recent Results of Turbulence Research”. In: *NACA TM 720*.

Quackenbush, T., R. Mckillip, and G. Whitehouse (2010). “Development and Testing of Deployable Vortex Generators Using SMA Actuation”. In.

Raffel, M., C. E. Willert, S. T. Wereley, and J. Kompenhans (2007). *Particle image velocimetry: a practical guide*. 2nd ed. Berlin: Springer.

Rumsey, C. L. (2024). *2D Zero Pressure Gradient Flat Plate Verification*. URL: `https://turbmodels.larc.nasa.gov/flatplate.html` (visited on 04/30/2024).

Sandborn, V. A. and S. J. Kline (1961). “Flow Models in Boundary-Layer Stall Inception”. In: *Journal of Basic Engineering* 83.3, pp. 317–327.

Sandborn, V. A. and C. Y. Liu (1968). “On turbulent boundary-layer separation”. In: *Journal of Fluid Mechanics* 32.2, pp. 293–304.

Santosh, S., G. Nithyanandh, J. Ashwath, and K. L. Kishore (2022). “Comparison of internal friction measurements on Ni-Ti reinforced smart composites prepared by additive manufacturing”. In: *Journal of Alloys and Compounds* 924, p. 166027.

Schatzman, D. M. and F. O. Thomas (2017). “An experimental investigation of an unsteady adverse pressure gradient turbulent boundary layer: embedded shear layer scaling”. In: *Journal of Fluid Mechanics* 815, pp. 592–642.

Schlichting, H. and K. Gersten (2017). *Boundary-Layer Theory*. Berlin, Heidelberg: Springer Berlin Heidelberg.

Schubauer, G. B. and P. S. Klebanoff (1951). “Investigation of separation of the turbulent boundary layer”. In.

Schubauer, G. B. and W. G. Spangenberg (1960). “Forced mixing in boundary layers”. In: *Journal of Fluid Mechanics* 8.1, pp. 10–32.

Simmons, D. J. (2020). “An experimental investigation of smooth-body flow separation”. PhD thesis. University of Notre Dame.

Simmons, D. J., F. O. Thomas, T. C. Corke, and F. Hussain (2022). “Experimental characterization of smooth body flow separation topography and topology on a two-dimensional geometry of finite span”. In: *Journal of Fluid Mechanics* 944, A42.

Simpson, R. L. (1981). “Review—A Review of Some Phenomena in Turbulent Flow Separation”. In: *Journal of Fluids Engineering* 103.4, pp. 520–533.

Simpson, R. L. (1989). “Turbulent Boundary-Layer Separation”. In: *Annual Review of Fluid Mechanics* 21, pp. 205–232.

– (1996). “Aspects of turbulent boundary-layer separation”. In: *Progress in Aerospace Sciences* 32.5, pp. 457–521.

Smith, F. (1994). “Theoretical prediction and design for vortex generators in turbulent boundary layers”. In: *Journal of Fluid Mechanics* 270.5, pp. 91–132.

Spalart, P. R., M. L. Shur, M. K. Strelets, and A. K. Travin (2015). “Direct Simulation and RANS Modelling of a Vortex Generator Flow”. In: *Flow, Turbulence and Combustion* 95.2, pp. 335–350.

Stillfried, F. von, S. Wallin, and A. V. Johansson (2012). “Vortex-Generator Models for Zero- and Adverse-Pressure-Gradient Flows”. In: *AIAA Journal* 50.4, pp. 855–866.

Tani, I. (1964). “Low-speed flows involving bubble separations”. In: *Progress in Aerospace Sciences* 5, pp. 70–103.

Taylor, H. D. (1947). “The elimination of diffuser separation by vortex generators.” In: *United Aircraft Corporation*.

Tropea, C., A. L. Yarin, and J. F. Foss, eds. (2007). *Springer Handbook of Experimental Fluid Mechanics*. Berlin, Heidelberg: Springer Berlin Heidelberg.

Velte, C. M., V. L. Okulov, and I. V. Naumov (2012). “Regimes of flow past a vortex generator”. In: *Technical Physics Letters* 38.4, pp. 379–382.

Velte, C. M., M. O. L. Hansen, and V. L. Okulov (2016). “Multiple vortex structures in the wake of a rectangular winglet in ground effect”. In: *Experimental Thermal and Fluid Science* 72, pp. 31–39.

Velte, C. M. (2013). “Vortex Generator Flow Model Based on Self-Similarity”. In: *AIAA Journal* 51.2, pp. 526–529.

Von Karman, T. H. (1931). *Mechanical similitude and turbulence*.

Wendt, B. J., I. Greber, and W. R. Hingst (1993). “Structure and development of streamwise vortex arrays embedded in a turbulent boundary layer”. In: *AIAA Journal* 31.2, pp. 319–325.

Westphal, R. V., J. P. Johnston, and J. K. Eaton (1984). “Experimental Study of Flow Reattachment in a Single- Sided Sudden Expansion”. In.

Westphal, R. V., J. K. Eaton, and W. R. Pauley (1987). “Interaction Between a Vortex and a Turbulent Boundary Layer in a Streamwise Pressure Gradient”. In: *Turbulent Shear Flows 5*. Ed. by F. Durst, B. E. Launder, J. L. Lumley, F. W. Schmidt, and J. H. Whitelaw. Berlin, Heidelberg: Springer, pp. 266–277.

White, F. M. (2006). *Viscous fluid flow*. 3rd ed. McGraw-Hill series in mechanical engineering. New York: McGraw-Hill. 652 pp.

Zhang, L., K. Yang, J. Xu, and M. Zhang (2011). “Modeling of delta-wing type vortex generators”. In: *Science China Technological Sciences* 54.2, pp. 277–285.

Zhu, C., Y. Feng, X. Shen, Z. Dang, J. Chen, Y. Qiu, Y. Feng, and T. Wang (2023). “Effects of the height and chordwise installation of the vane-type vortex generators on the unsteady aerodynamics of a wind turbine airfoil undergoing dynamic stall”. In: *Energy* 266.

A

Theoretical framework of separation control

To provide a theoretical understanding of the underlying mechanisms that govern controlled separation, it is beneficial to adopt the two-dimensional integral boundary layer (IBL) approach. Drela (2014) presented the mathematical foundations of IBL relations, offering a comprehensive explanation of this approach.

The dimensionless *von Karman momentum integral equation* governs the evolution of the momentum thickness θ and can be expressed as:

$$\frac{d\theta}{dx} = \frac{C_f}{2} - (H + 2 - M_e^2)\frac{\theta}{u_e}\frac{du_e}{dx} \tag{A.1}$$

On the other hand, the dimensionless *kinetic energy integral equation* governs the evolution of the related kinetic energy thickness θ^*, and can be expressed as:

$$\frac{d\theta^*}{dx} = 2C_{\mathcal{D}} - \left(\frac{2H^{**}}{H^*} + 3 - M_e^2\right)\frac{\theta^*}{u_e}\frac{du_e}{dx} \tag{A.2}$$

For an incompressible flow where $\delta^{**} = 0$ given that $\rho/\rho_e = 1$, and $M_e^2 << 1$, both Equation A.1 and Equation A.2 can be simplified to Equation A.3 and Equation A.4, respectively.

$$\frac{d\theta}{dx} = \frac{C_f}{2} - (H + 2)\frac{\theta}{u_e}\frac{du_e}{dx} \tag{A.3}$$

$$\frac{d\theta^*}{dx} = 2C_{\mathcal{D}} - 3\frac{\theta^*}{u_e}\frac{du_e}{dx} \tag{A.4}$$

Combining both equations and solving for the streamwise velocity gradient du_e/dx yields:

$$\frac{\theta}{u_e}\frac{du_e}{dx} = \frac{1}{H-1}\left(\frac{C_f}{2} - \frac{2C_{\mathcal{D}}}{H^*}\right) \tag{A.5}$$

According to this equation, in order to reduce the risk of boundary layer separation, the goal is to increase the maximum tolerated pressure gradient, or conversely, to minimize the most negative streamwise velocity gradient. Consequently, the left-hand side of the equation can be minimized by increasing the dissipation term while ensuring that C_f remains above zero for an attached flow (Baldacchino 2019).

Considering that the dissipation integral $\mathcal{D}$ is defined as:

$$\mathcal{D} = \int_0^{\delta} (\mu + \mu_t) \frac{\partial u}{\partial y} \, dy \tag{A.6}$$

A valid approach to increase the dissipation rate is to increase the turbulent kinetic energy, represented by μ_t. This can be done by increasing the energy transfer from the mean flow to the boundary layer, which is the same effect that vortex generators have, as Lengani et al. (2011) found.

B

Velocity gradient dependency on test section height

Apply 1D mass conservation equation

$$\rho A(x) U(x) = C_1 \tag{B.1}$$

where $A(x) = b\, h(x)$ and $b = 0.6$ m.

$$U(x) = \frac{C_1}{\rho A(x)} = \frac{C_1}{\rho b h(x)} = \frac{C_2}{h(x)} \tag{B.2}$$

where $C_2 = C_1/(\rho b)$

$$\frac{dU}{dx} = \frac{d}{dx}\left(\frac{C_2}{h(x)}\right) = -\frac{C_2}{h^2}\frac{dh}{dx} \tag{B.3}$$

Calculate the constants:

$$C_1 = \rho_0 A_0 U_0 \tag{B.4}$$

$$C_2 = C_1/(\rho b) \tag{B.5}$$

C

Model drawings

This section presents the technical drawings describing the geometries of all the vortex generator designs studied in this research.

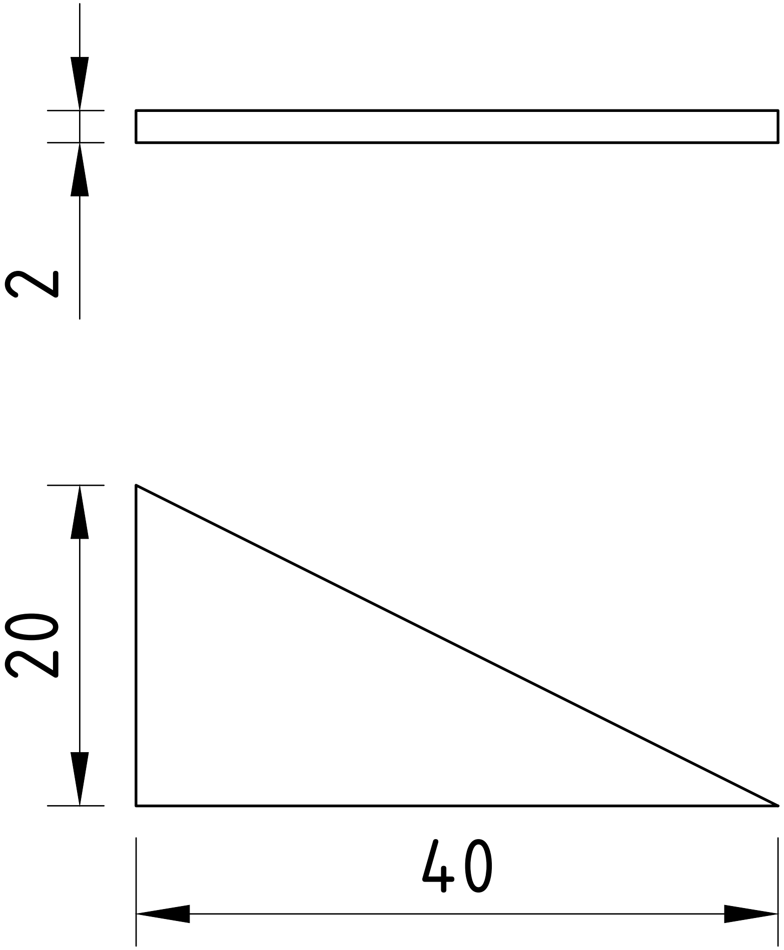

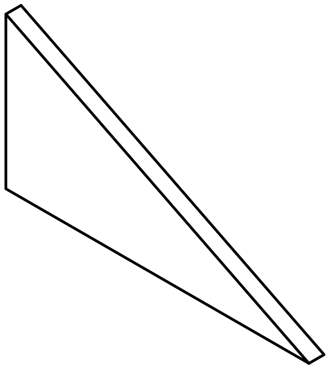

Dept.	Technical reference	Created by	Approved by
		Jorge Miret Marco 6/4/24	
		Document type	Document status
		Title	DWG No.
		Vane	VG-01
			Rev. / Date of issue / Sheet 1/1

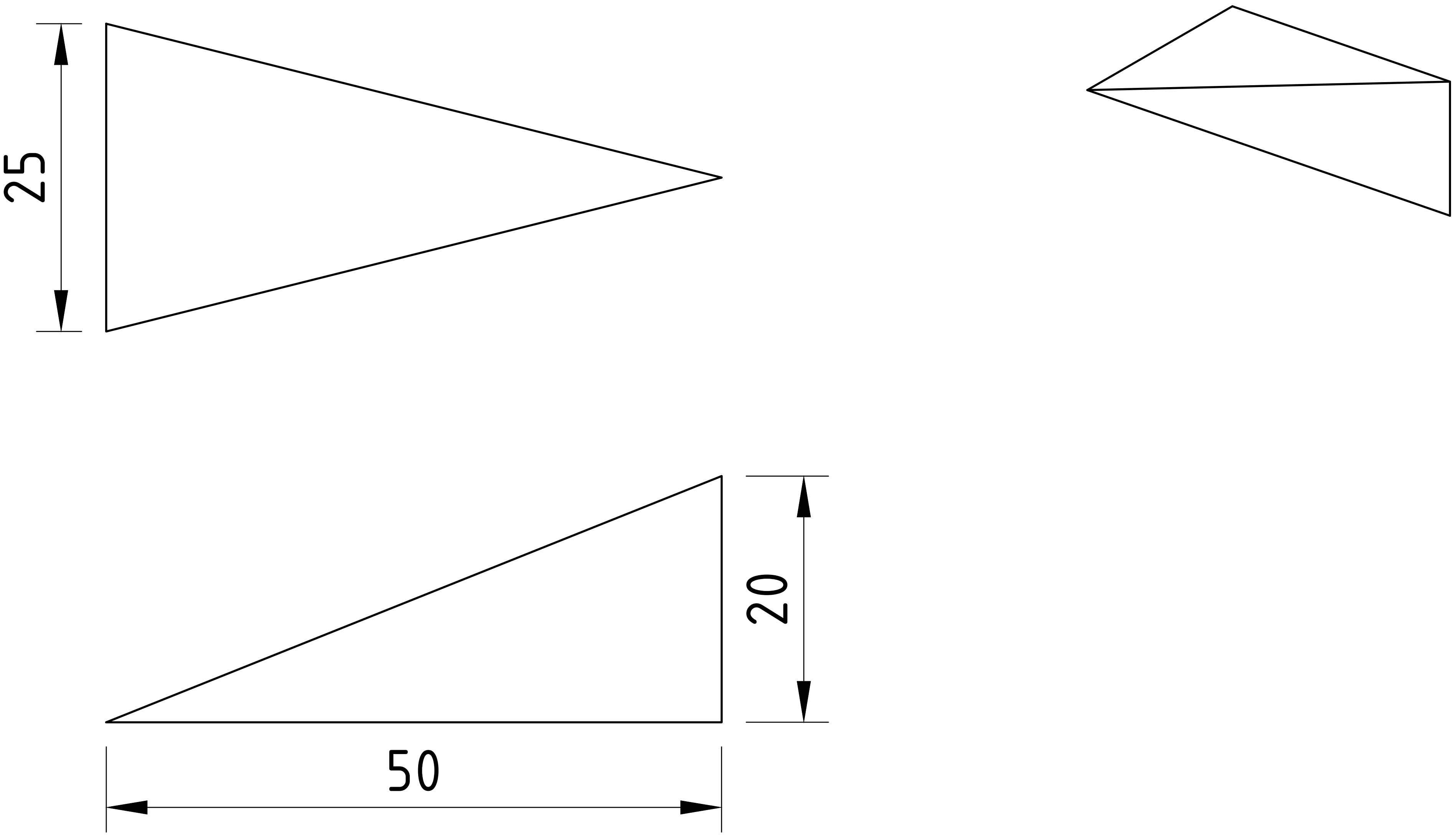

Dept.	Technical reference	Created by Jorge Miret Marco 6/4/24	Approved by
		Document type	Document status
		Title Ramp	DWG No. VG-02
			Rev. / Date of issue / Sheet 1/1

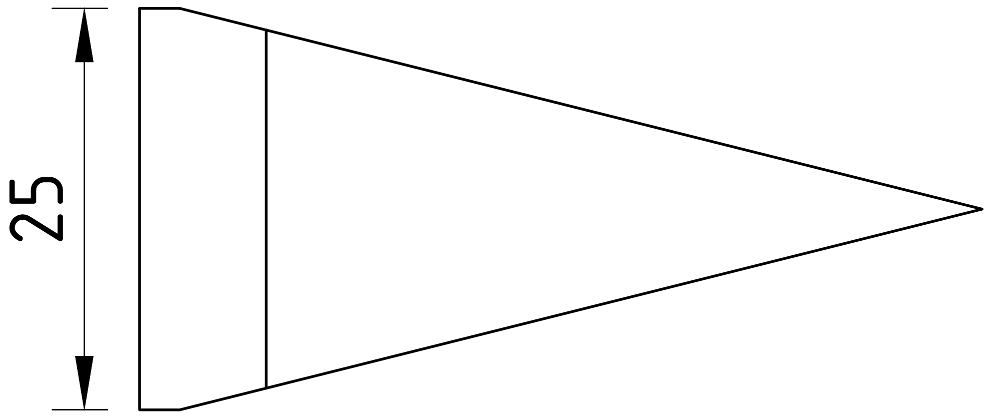

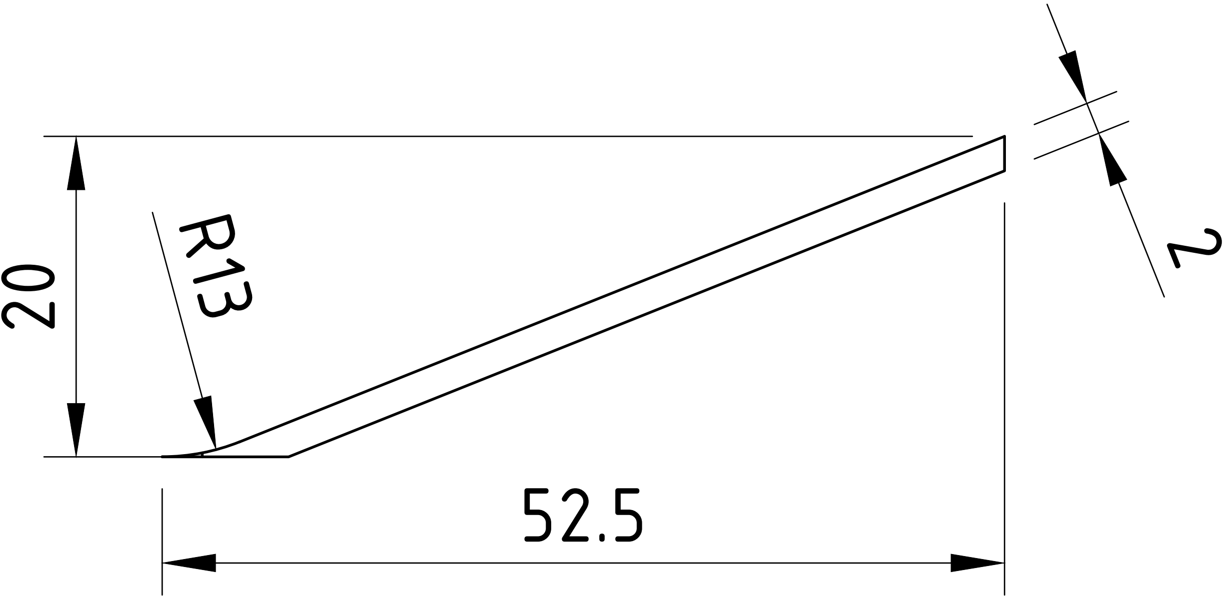

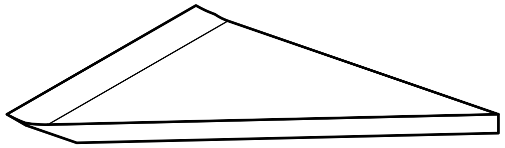

Dept.	Technical reference	Created by	Approved by
		Jorge Miret Marco 6/5/24	
		Document type	Document status
		Title Hollow Ramp	DWG No. VG-03

Rev.	Date of issue	Sheet
		1/1

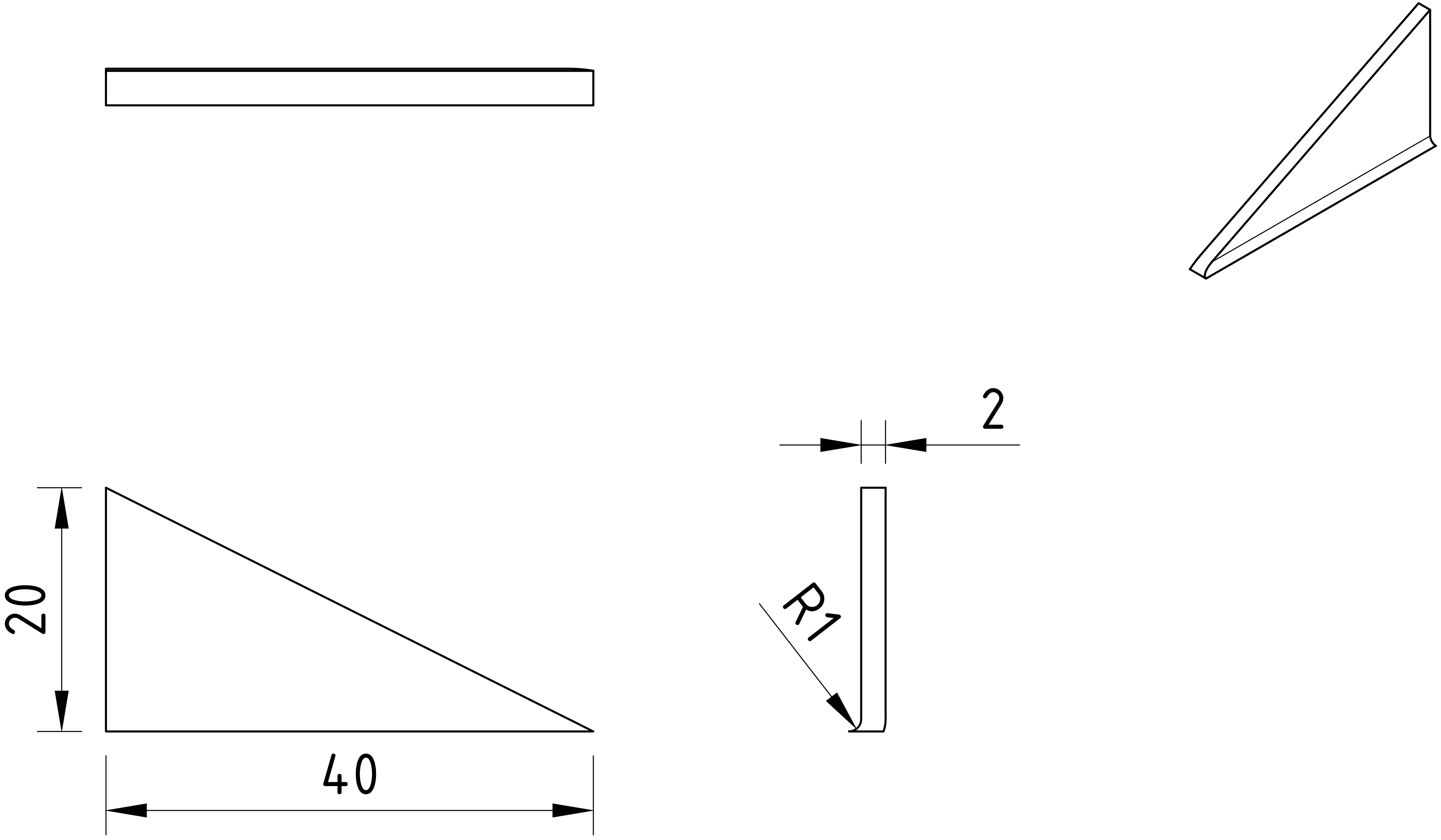

Dept.	Technical reference	Created by Jorge Miret Marco 6/5/24	Approved by
		Document type	Document status
		Title Curved Vane	DWG No. VG-04
			Rev. Date of issue Sheet 1/1